Precision Laser Spectroscopy in the Extreme Ultraviolet

Kjeld S.E. Eikema and Wim Ubachs

Department of Physics and Astronomy, Vrije Universiteit, Amsterdam, The Netherlands

1 INTRODUCTION

The wavelength range shorter than 200 nm is usually referred to as the vacuum ultraviolet (VUV), since the atmospheric constituent gases are not transparent for this radiation. Wavelengths shorter than 100 nm, where no transparent optical materials exist, define the regime of the extreme ultraviolet (XUV); the cutoff of LiF, the material with the shortest wavelength transparency, is at 105 nm. These issues of atmospheric absorption and the lack of optics hamper spectroscopies in these ranges where many atoms and molecules exhibit strong dipole-allowed transitions.

Techniques for using electromagnetic radiation in these difficult-to-access ranges were being explored since the turn of the nineteenth to the twentieth century. Schumann (1928) realized that quartz windows and prisms could be replaced by fluorite materials, and he invented the gelatin-containing Schumann plate by means of which photographic spectra at short wavelengths could be measured. Further, he was the first to realize the opaqueness of air and to demonstrate the solution to construct a vacuum spectrograph for spectroscopic investigations at short wavelengths ($\lambda < 200$ nm). Lyman extended this work and was able to cover wavelengths as short as 25 nm, where he discovered the principal series in the helium atom below the series limit at 50 nm (Lyman 1924); his name is also connected with the discovery of the Lyman series in the hydrogen atom (Lyman 1914) and the Lyman band systems in the hydrogen molecule (Lyman 1906), both falling in the XUV domain. Hopfield realized that continuum radiation in the XUV could be produced by discharging H_2 (Hopfield and Leifson 1923) and helium gases (Hopfield 1930), therewith opening the possibility of *absorption* spectroscopy in the XUV. Over the years, technical developments in the improved mounting of gratings in various configurations (Rowland circle, Eagle normal incidence, and Seya–Namioka geometry), the production of reflective coatings and progress in the ruling of gratings, as well as the study of emulsions for enhancing photographic films and the development of photoelectric detectors greatly facilitated the opportunities in XUV spectroscopy (Tousey 1962). As a highlight of classical absorption spectroscopy in the XUV, using a discharge continuum and photographic detection, we mention the precision study on the helium $(1s)^2\,{}^1S_0 - (1s)(2p)\,{}^1P_1$ resonance line at 58.4 nm, measured by Herzberg to an accuracy of 0.15 cm^{-1} (Herzberg 1958).

The invention of synchrotron light sources revolutionized the possibility and flexibility in performing excitation spectroscopy in the range of the XUV (Tomboulian and Hartman 1956). Continuum profiles of smooth intensity distributions without the superimposed emission and absorption lines of discharge sources facilitate spectroscopic applications, and the use of undulators in the third-generation synchrotrons has greatly enhanced the photon flux at short wavelengths. However, synchrotron-based XUV light sources have in common with discharge sources the limitations of spectroscopic resolution imposed by properties of grating spectrographs. A conceptually different concept than that of "classical" grating-based spectroscopy is that of Fourier-transform (FT) spectroscopy, usually operated at infrared wavelengths, but extended to the range of the VUV by Thorne and coworkers, applying it even in combination with synchrotron radiation

Handbook of High-resolution Spectroscopy. Edited by Martin Quack and Frédéric Merkt.
ISBN: 978-0-470-74959-3.

(Yoshino *et al*. 1995). Currently, an FT spectrometer is also being developed for the windowless XUV regime, without the beam-splitting element that forms the basis of a Mach–Zender interferometer commonly at the heart of an FT spectrometer. This brings the prospect of greatly enhancing the spectral resolution in the XUV domain over grating-based instruments, in particular, when the instrument can be combined with a synchrotron source delivering the short-wavelength photons (Joyeux *et al*. 2005).

Lasers can be used for the production of electromagnetic radiation at XUV wavelengths and for XUV spectroscopy in various ways. True lasing was demonstrated not only at giant installations but also in tabletop setups as by Rocca *et al*. (1994), exciting a discharge in highly charged Ne-like argon, therewith inducing laser operation at 46.9 nm. This application delivers only XUV radiation in certain lines. Laser-produced plasma sources can, in contrast, be employed to produce clean, line-free continua in broad ranges of the XUV and VUV from 4 to 200 nm by suitable choice of target materials. This was demonstrated by Costello and coworkers, including some online spectroscopic applications, which are again limited in resolution by the spectrometers employed (Costello *et al*. 1991).

The most important contribution of lasers to XUV spectroscopy is through the production of coherent radiation at short wavelengths via harmonic generation and other wave-mixing techniques. In these nonlinear optical processes, the coherence properties of the incident laser radiation are largely retained. In the case of upconversion of the output of narrow band radiation, i.e., of pulsed lasers in the nanosecond regime, tunable and narrowband radiation in the XUV domain is produced, which is used in many applications of scanning excitation spectroscopy, which are discussed in Section 3. Upconversion of ultrashort laser pulses in the femtosecond regime is rather straightforward, but the produced XUV output is broadband, well adapted to perform dynamical studies in atomic and molecular systems, but not so well suited in high-resolution spectroscopic applications. However, if the phases between consecutive pulses from a femtosecond laser are controlled, such as in frequency comb lasers (Hall 2006, Hänsch 2006), the coherence properties of the pulse sequences can be employed to perform ultrahigh-resolution spectroscopy in the XUV domain. These specific applications of ultrafast lasers in high-resolution spectroscopy are the subject of Section 5. Before discussing these spectroscopic applications of tunable XUV lasers, in Section 2, the theory of nonlinear conversion and harmonic generation is described. A distinction is made between two regimes: the perturbative regime, for intensities of $<10^{12}\ \mathrm{W\,cm^{-2}}$, in which only low-order harmonics are produced, and the so-called plateau regime, for intensities $>10^{13}\ \mathrm{W\,cm^{-2}}$, in which a long sequence of harmonic orders is generated. In Section 4, an intermediate approach is described (Brandi *et al*. 2003a): the use of high-intensity laser pulses of durations in the order of 300 ps. This allows for XUV generation in the high-harmonic plateau regime but, nevertheless, retaining narrow bandwidth that can be used in XUV spectroscopic scanning applications.

2 NONLINEAR HARMONIC CONVERSION TECHNIQUES

The concept and the prospects of harmonic conversion of optical frequencies via nonlinear optical methods were considered in the early years immediately after the invention of the laser. Bloembergen and coworkers described a wide variety of nonlinear optical phenomena in a seminal paper (Armstrong *et al*. 1962). In 1969, harmonic generation in gases was demonstrated, albeit with a nontunable ruby laser, but it opened the rich field of VUV and XUV spectroscopies, based on converted coherent laser radiation (New and Ward 1967). Initially, at the times when only nanosecond-pulsed lasers were available for high-power laser experiments, the nonlinear processes were described in the framework of perturbative theories. Most precision studies in the XUV have been performed with such nanosecond laser pulses; therefore, we explore this in more detail in the following sections.

2.1 The Nonlinear Polarization

When a medium is irradiated by laser beams, represented by electric field vectors $\boldsymbol{E}_i$ and propagation vectors $\boldsymbol{k}_i$, a polarization is induced in the medium:

$$\boldsymbol{P}_i = \epsilon_0 \left[\chi_{ij}^{(1)} \boldsymbol{E}_j + \frac{1}{2} \chi_{ijk}^{(2)} \boldsymbol{E}_j \boldsymbol{E}_k + \frac{1}{6} \chi_{ijkl}^{(3)} \boldsymbol{E}_j \boldsymbol{E}_k \boldsymbol{E}_l + O(E^4) \right] \tag{1}$$

where $\chi^{(1)}$ is the linear susceptibility and $\chi^{(n)}$ the nonlinear susceptibilities; these are material properties of the medium. In a medium with inversion symmetry (such as an ensemble of gaseous particles), the even orders in the nonlinear polarization cancel and hence $\chi^{(2n)} = 0$ for integer n. Furthermore, the nonlinear susceptibilities $\chi^{(n)}$ are frequency dependent, i.e., on the frequency of all input fields, as well as on the frequency at the induced polarization. For the production of VUV and XUV radiation with nanosecond-pulsed lasers, the third-order nonlinear susceptibility $\chi^{(3)}$ is the important term.

The physics of the harmonic conversion processes, the attainable conversion efficiencies, the resonance enhancement effects, dependence on focusing conditions, gas densities, and the polarization properties are related to two crucial aspects of wave mixing: (i) a macroscopic effect related to the so-called phase-matching properties, mainly affected by the indices of refraction and their dispersion properties, as well as on the geometry of the beams and their focusing conditions and (ii) the microscopic (material) properties of the medium, the physics of which is contained in $\chi^{(3)}$.

An analysis starts with the nonlinear polarization induced in the medium:

$$\boldsymbol{P}_i^{(3)} = \chi_{ijkl}^{(3)} \boldsymbol{E}_j \boldsymbol{E}_k \boldsymbol{E}_l \tag{2}$$

At this point, several wave-mixing processes can be considered; in the case of $\chi^{(3)}$, the processes are referred to as *four-wave mixing*, where the fourth wave is generated from three incident radiation fields, which are not necessarily different:

$$\begin{aligned} \text{Process I}: &\ \omega_1 + \omega_2 + \omega_3 \rightarrow \omega_4 \\ \text{Process II}: &\ \omega_1 + \omega_2 - \omega_3 \rightarrow \omega_4 \\ \text{Process III}: &\ \omega_1 - \omega_2 - \omega_3 \rightarrow \omega_4 \end{aligned} \tag{3}$$

The first process covers sum-frequency mixing, of which the third-harmonic generation (THG) is a special case; the second process is difference-frequency mixing; and the third process is not discussed further, since it generally does not lead to short-wavelength generation. Each of these processes yields a nonlinear polarization $\boldsymbol{P}_i^{(3)}(\omega_4)$ in the medium. This polarization at frequency ω_4 can be inserted as a source term in Maxwell's wave equation, producing a propagating electromagnetic field, also at frequency ω_4:

$$\nabla^2 \boldsymbol{E}(\omega_4) - \left(\frac{n}{c}\right)^2 \frac{\partial^2}{\partial t^2} \boldsymbol{E}(\omega_4) = \frac{4\pi}{c^2} \frac{\partial^2}{\partial t^2} \boldsymbol{P}(\omega_4) \tag{4}$$

After substitution of the source term as defined in equation (2), Maxwell's equation can be solved at frequency ω_4. As a general result, for the intensity of the radiation at frequency ω_4, one finds

$$I(\omega_4) \propto N^2 |\chi^{(3)}|^2 I(\omega_1) I(\omega_2) I(\omega_3) \Phi_{\text{pm}}(\boldsymbol{k}_1, \boldsymbol{k}_2, \boldsymbol{k}_3, \boldsymbol{k}_4) \tag{5}$$

where the proportionality involves some constants (depending on the choice of esu/cgs or SI) and degeneracy factors, with N being the density of the medium, $I(\omega_j)$ the intensities of the incident fields, and Φ_{pm} the phase-matching integral depending on the phase relationships between the various interacting waves, expressed by their $\boldsymbol{k}$ vectors. Physically, this can be understood from the fact that effective wave-mixing is only established if the various fields remain in phase. Dispersion, i.e., the dependence of the index of refraction on the wavelength $n(\lambda)$ destroys the coherent build-up of radiation; after each relative phase slip of π between the fields, destructive interference reconverts the generated field into input fields.

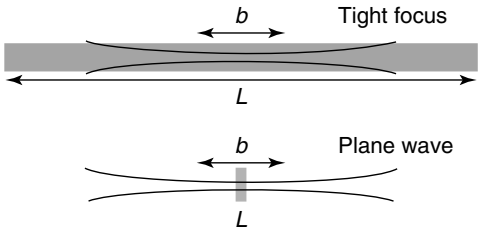

Figure 1 The focal geometries in two limits as described in the text: in the case of tight focusing, the nonlinear gaseous medium (indicated in gray shade) extends over the entire focal region ($b \ll L$) and the plane-wave limit where the interaction zone is much smaller than the focus ($b \gg L$). Note that the first geometry corresponds to that of a cell filled with a gas, whereas the second one is typical for a laser beam focused into a gas jet of limited interaction length.

These phenomena of phase matching and their effect on the conversion efficiency in third-order nonlinear processes have been quantitatively described by Bjorklund (1975) and this is not repeated here. However, we discuss some issues of these techniques that are of practical relevance for the user of VUV and XUV radiation in spectroscopic applications. First of all, a distinction between two regimes of harmonic generation can be made—that of *tight focusing* and that of *plane waves*—as shown in Figure 1. In the following two subsections, phase matching in these two limiting regimes is described.

2.2 Phase Matching in the Tight-focus Limit

In the case of the tight focus, the phase evolution of the electromagnetic fields (laser beams) must be evaluated over the length of the medium covering the entire beam waist of the focal geometry. In the plane-wave limit, there is no curvature of the beams over the short range that the medium covers; the medium does not see a focus. Bjorklund (1975) has derived solutions for the phase-matching integrals for a number of limiting cases of interest. First, for the sum-frequency mixing process (also including third-harmonic radiation), i.e., for process I

$$\begin{aligned} \Phi_{\text{TF}}^{\text{I}} &= \pi^2 (b\Delta k)^2 \exp\left[\frac{b\Delta k}{2}\right] \text{ for } \Delta k < 0 \\ &= 0 \text{ for } \Delta k \geq 0 \end{aligned} \tag{6}$$

and for process II

$$\Phi_{\text{TF}}^{\text{II}} = \pi^2 \exp\left[-b|\Delta k|\right] \tag{7}$$

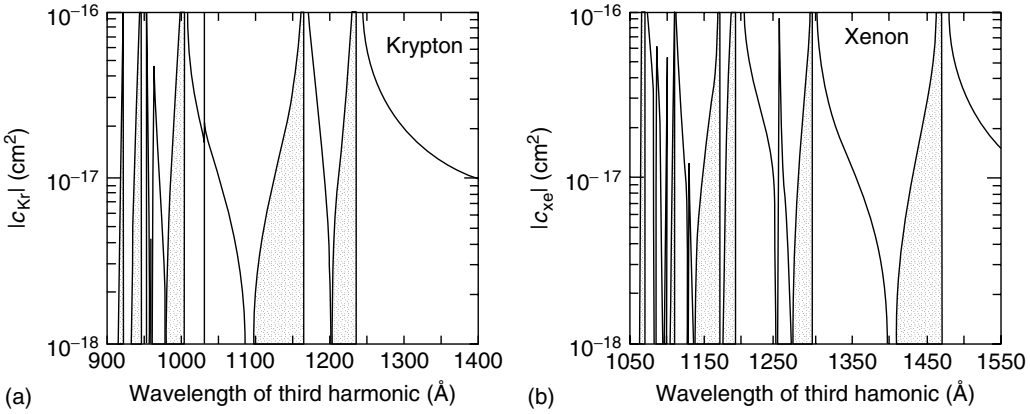

Figure 2 Calculation of the wave mismatch per atom C, as defined in equation (9) for Kr (a) and Xe (b). The gray-shaded areas exhibit negative dispersion and, hence, the wavelength regions where THG can be effectively produced in the tight-focusing limit. [Reproduced from Mahon *et al*. (1979).]

The phase mismatch is defined as

$$\Delta k = |\Delta \boldsymbol{k}| = |\boldsymbol{k}_4 - \boldsymbol{k}_1 - \boldsymbol{k}_2 \pm \boldsymbol{k}_3| \tag{8}$$

with the $(-)$ sign for the sum-frequency mixing process (I) and the $(+)$ sign for the difference-frequency mixing process (II); b is the so-called confocal parameter, which is equal to $2\pi w_0^2/\lambda$, with w_0 being the focal beam waist. These results can be interpreted as follows. In the case of process II, difference-frequency mixing, phase matching can be established for both positive and negative ranges of Δk and, hence, for gases with positive and negative dispersion. Process I can only be phase matched if $\Delta k < 0$, i.e., in gases of negative dispersion and is, therefore, more constrained.

The physics of the phase-matching phenomena can be understood as a combination of two effects. On the one hand, there is dispersion in the gas that causes a gradual phase slip and, on the other hand, there is the Gouy phase, causing a π phase slip when traversing a focus region over the entire length for a number of confocal lengths b. This makes the tight-focus geometry different from the plane-wave geometry, where the Gouy phase plays no role.

The phase-matching condition can be further quantitatively evaluated in the case of the noble gases, where the energy level structure and the dispersion are well known. For the example of third-harmonic generation, the wave mismatch can be written as

$$\Delta k = \frac{2\pi}{\lambda}(n_1 - n_3) = CN \tag{9}$$

where λ is the wavelength at the fundamental, N the density of the medium, and C the wave mismatch per atom. Calculations of C have been performed for Kr and Xe (Mahon *et al*. 1979), yielding the results displayed in Figure 2. Negative dispersion in atoms (shown in gray-shaded areas in Figure 2) is known to occur in the energy range just above the allowed transitions, and this is reflected in the figure. Below the first resonance line (i.e., at the long wavelength edge of 123.5 nm in Kr and 147 nm in Xe), the gas is positively dispersive and no THG can occur. At shorter wavelengths, there is an oscillating pattern governed by the location of energy levels to which dipole-allowed transitions can occur from the ground state. Hence, in the gray-shaded regions, THG can be effectively produced in these media. Note that here it is shown that the macroscopic property of phase matching also depends on the microscopic properties of the medium.

From the above analysis, it follows that the phase mismatch in a wave-mixing process is dependent on the density of the gas, via $\Delta k = CN$, where C is a material property and N the number density of the gas. From equation (6), it not only follows that THG can occur in a negatively dispersive gas but also that there exists an optimum value of Δk for which THG is optimal. For process I, it can be shown that $\Phi_{\mathrm{TF}}^{\mathrm{I}} \approx 5.3$ for $\Delta k = -2/b$. For a certain focal geometry (fixed b), this condition can be met by varying the gas density N as shown for the THG of $\lambda_1 = 354$ nm in xenon gas in Figure 3. In the work by Kung *et al*., it was demonstrated that by pressure phase matching, the conversion efficiency could be increased to 0.9% (Bjorklund 1975).

Kung and coworkers have further demonstrated that mixing of gases can enhance the THG-conversion efficiency even more (Kung 1983). Mixing allows for the optimization of the nonlinear susceptibility with one gas (xenon), and the loss in the phase matching is compensated by adding argon gas, which has different dispersion properties at the wavelengths chosen. The optimized mixing ratio depends on the choice of the b parameter and the cell length L. By this means, a conversion efficiency of 2.8% was experimentally demonstrated (Kung 1983).

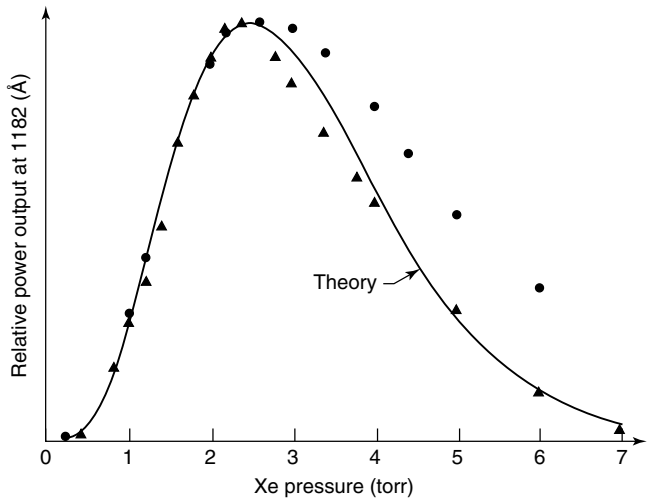

Figure 3 Optimization of phase matching in xenon gas by varying the gas pressure. Conditions $b/L = 0.025$ and $f/L = 0.5$, the focus positioned at the center of the cell. The points correspond to two data sets taken at different settings of the aperture; the curve represents a calculation. [Reproduced from Bjorklund (1975).]

2.3 Phase Matching in the Plane-wave Limit: Gas Jets

In the approximation of the plane-wave limit, for both processes I and II, it is found that

$$\Phi_{\mathrm{PW}}^{\mathrm{I,II}} = \frac{4L^2}{b^2}\sin^2\left(\frac{\Delta kL}{2}\right) \tag{10}$$

Since under the condition of the plane-wave limit (see lower part of Figure 1) the propagating light beam does not undergo a change of wavefront inside the nonlinear medium (in fact, there is no focus inside the medium), the effect of the Gouy phase shift does not occur if $b \ll L$. Since the high intensities required for THG and other harmonic conversion processes are only obtained in a focus, the plane-wave conditions are only realistically met in gas jet experiments. The conversion efficiency is much lower than in the case of the tight-focus limit and the optimum is reached for $\Delta k = 0$.

The use of pulsed valves for the production of harmonics was a breakthrough in particular to reach the windowless regime of the XUV (Kung 1983). The requirement of handling radiation in the XUV by definition prohibits the use of window materials, and hence of cells that should be sealed off by some optical material. The pulsed jet, as displayed in Figure 4, is the solution: in combination with differential pumping techniques, a situation can be achieved in which harmonic conversion can take place inside a gaseous nonlinear medium, while at the same time vacuum conditions are maintained in the entire measurement setup, outside the limited region of a laser focus. In particular the generated coherent XUV beam does not undergo absorption in the region outside the focus, and can be propagated and transported into a differentially pumped vacuum chamber, where it can be used for spectroscopic experiments. The first application of this scheme was the excitation of H_2 molecules in the wavelength range 97–102 nm (Marinero *et al*. 1983).

2.4 Coherently Propagating Beams and Noncollinear Phase Matching

An important aspect of four-wave mixing processes and their phase-matching properties is that coherent beams of light are generated, which propagate in a direction determined by the incident beams. In general, a fourth beam is generated with wave vector $\boldsymbol{k}_4$, for which the following equation holds:

$$\boldsymbol{k}_4 = \boldsymbol{k}_1 + \boldsymbol{k}_2 \pm \boldsymbol{k}_3 \tag{11}$$

Hence, in the case of collinearly incident beams, $\boldsymbol{k}_1$, $\boldsymbol{k}_2$, and $\boldsymbol{k}_3$ are parallel, and the wavevector of the generated beam $\boldsymbol{k}_4$ points exactly in the forward direction along the incident beams.

If some of the beams have transverse components relative to the propagation direction, the true vectorial properties of the wave vectors $\boldsymbol{k}_i$ have to be taken into account. These properties can be beneficially applied in a noncollinear phase-matching geometry configuration of input beams, as displayed in Figure 5 (Hannemann *et al*. 2005). Experimentally, a small angle between incident beams wave vectors at $\boldsymbol{k}_1$ ($\lambda_1 = 212$ nm) and $\boldsymbol{k}_2$ (at a tunable wavelength in the visible range) was chosen in a sum-frequency process, yielding $\omega_4 = 2\omega_1 + \omega_2$. The resulting direction of the produced field at frequency ω_4 is in the direction $\boldsymbol{k}_4 = 2\boldsymbol{k}_1 + \boldsymbol{k}_2$. The advantage of this method is that the direction of $\boldsymbol{k}_4$ is not along any of the incident wave vectors, or of the third harmonic (which is along $\boldsymbol{k}_1$), or along the difference-frequency beam. As was demonstrated by placing a slit, selecting the angle along the sum-frequency direction, a pure monochromatic XUV beam was produced, which could be applied online for spectroscopic studies (Hannemann *et al*. 2005). The phase-matching geometry then intrinsically operates as a monochromator.

Focused laser beams exhibit a spread in $\boldsymbol{k}$-vectors, depending on the specific focal conditions (numerical aperture and confocal parameter), leading to a spread in angles $\Delta\theta$ emanating from a focus. In the simplest case of a TM_{00} beam profile, this distribution is Gaussian. Owing to the nonlinear conversion in harmonic generation, the spread in angles $\Delta\theta$ for the harmonically generated beams is

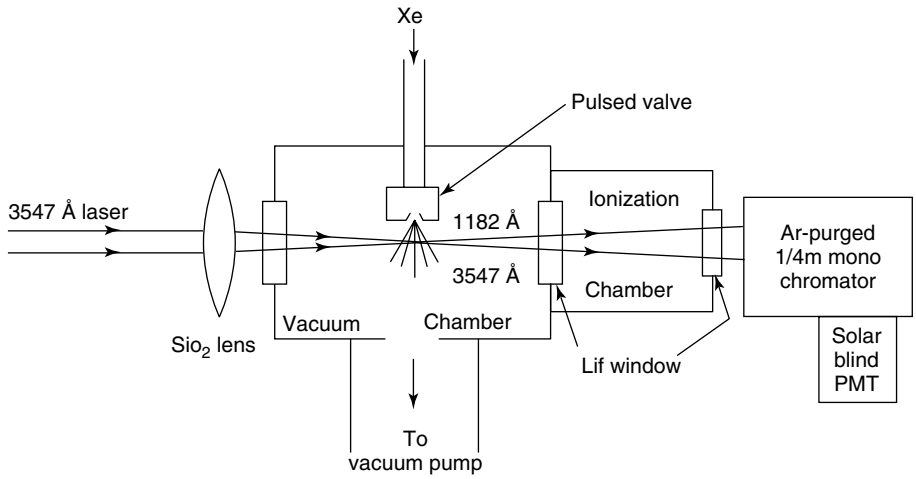

Figure 4 Principle of using a pulsed valve for the production of XUV light in a gaseous medium while keeping vacuum conditions outside the focal region in which the harmonic conversion takes place. Differential pumping of the chambers along the direction of propagation of the generated XUV beam further maintains vacuum conditions in a typical setup for XUV spectroscopy. The concept of harmonic generation in a gas jet was first demonstrated by Kung, and the figure is reproduced from Kung (1983); in this case, an LiF window is used at the exit of the chamber, but later a windowless connection to a differentially pumped chamber became regularly used in the XUV domain.

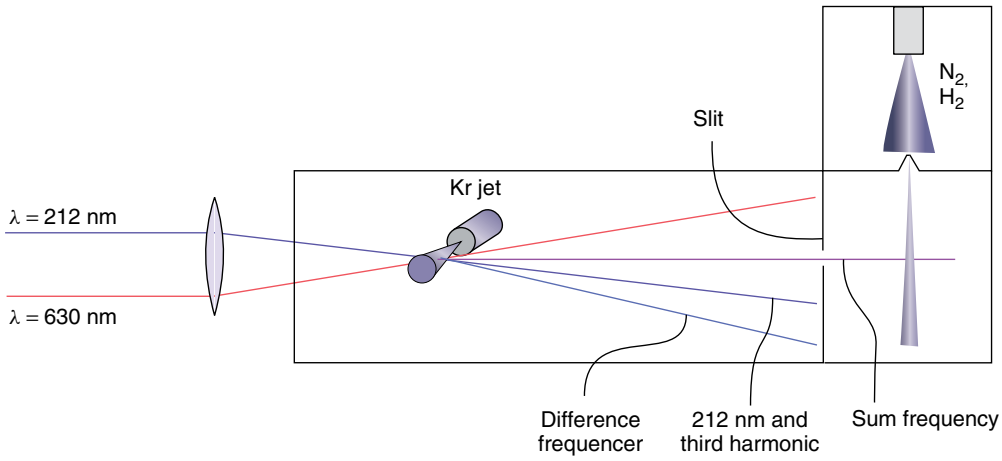

Figure 5 Noncollinearly phase-matched scheme for a sum-frequency mixing process $\omega_{\mathrm{XUV}} = 2\omega_{\mathrm{UV}} + \omega_{\mathrm{VIS}}$, where the sum-frequency-generated frequency is filtered out in the direction of the propagating wave vector. The setup also displays how a crossed-beam spectroscopic experiment is performed in a differentially pumped vacuum hamber into which the XUV beam is directed. [Adapted from Hannemann *et al*. (2005).]

more confined to the propagating axis than the fundamental beams. In the case of THG for a Gaussian beam, one has

$$\Delta\theta_{\mathrm{THG}} = \frac{1}{\sqrt{3}}\Delta\theta_{\mathrm{fund}} \tag{12}$$

The property of spread in $\boldsymbol{k}$-vectors can be turned into an XUV filtering instrument by putting a post or a beam stop in the incident laser beam before focusing. In such case, the $\boldsymbol{k}_{\mathrm{UV}}$ vectors lying on a cone generate a THG beam with intensity in the dark region in the far field as shown in Figure 6. Selection in the far field, either by a slit or by a diaphragm, then results in a beam of pure THG, without the overlap of an intense fundamental laser beam. This constitutes, in fact, a monochromatizing device, which is particularly useful in XUV absorption experiments or in multistep excitation experiments involving XUV photons (Reinhold *et al*. 1998).

2.5 Resonance Enhancement Effects

The third-order nonlinear susceptibility $\chi^{(3)}_{ijkl}$ is, in fact, a material response function at the single-particle level. According to equation (5), its absolute square $|\chi^{(3)}_{ijkl}|^2$

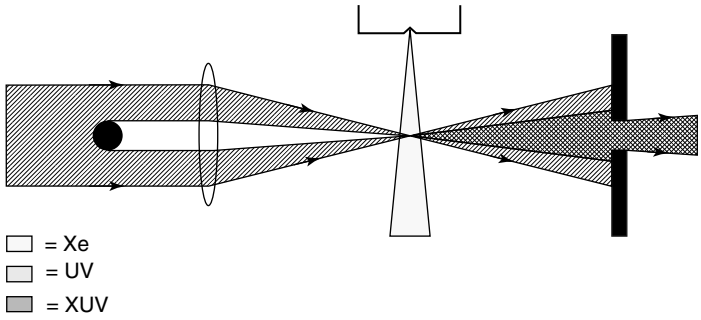

Figure 6 Geometrical layout of the XUV filtering instrument based on the selection of incident wave vectors $\boldsymbol{k}_{\text{fund}}$ and generated wave vectors $\boldsymbol{k}_{\text{XUV}}$. [Adapted from Reinhold *et al*. (1998).]

represents the strength of the nonlinear process. It is a complicated function for which full descriptions are given elsewhere (Shen 1984, Boyd 2003). In short, it can be written as

$$\chi^{(3)}_{ijkl}(\omega_4, \omega_1, \omega_2, \omega_3,) = \sum_{gmnp} \sum_{\text{terms}} \frac{< g|\boldsymbol{r}_j|m >< m|\boldsymbol{r}_k|n >< n|\boldsymbol{r}_l|p >< p|\boldsymbol{r}_i|g >}{(\omega_{gm} \pm \omega_1)(\omega_{gn} \pm \omega_1 \pm \omega_2)(\omega_{gp} \pm \omega_1 \pm \omega_2 \pm \omega_3)} \tag{13}$$

where the first summation is over all possible quantum states in the atomic medium, $|g >$ being the ground state and $|m >$, $|n >$, and $|p >$ all possible excited states, including continuum states, in the atom. The second summation is taken over a large number of terms corresponding to all permutations of $(+)$ and $(-)$ signs in the denominator. The brackets in the numerator represent electric dipole transitions for each of the four photons involved in the wave-mixing process. Note that these four photons describe a *parametric* process, defined as a wave-mixing process in which no energy exchange with the medium takes place; the four-photon cycle starts in a ground state $|g >$, and it ends in the same state.

This representation of the nonlinear susceptibility elucidates how resonances in the atomic medium give rise to enhancement of $\chi^{(3)}$. Each of the three terms in the denominator may yield a resonance, e.g., if the first photon at frequency ω_1 matches the energy separation ω_{gm} in the atoms. Two-photon resonances are particularly useful for resonance-enhanced sum-frequency mixing: this occurs if (assuming $\omega_1 = \omega_2$) the level spacing in the atom ω_{gn} is equal to $2\omega_1$. The noble gases contain many of these two-photon resonances, the strongest being the $(4p)^6 - (4p)^5(5p)$ $J = 0$ two-photon resonance in krypton at $\lambda = 212.5$ nm (Miyazaki *et al*. 1989). Schemes using these two-photon resonances for two-photon resonant sum-frequency (Hilber *et al*. 1987, Marangos *et al*. 1990) as well as difference-frequency mixing (Hilbig and Wallenstein 1982) were amply explored. Merkt and coworkers developed a multipurpose XUV spectrometer based on these schemes of narrow bandwidth and wide tunability up to 20 eV (Hollenstein *et al*. 2000, Rupper and Merkt 2004), which was used in a wide variety of high-resolution spectroscopic applications (*see* Merkt *et al*. 2011: **High-resolution Photoelectron Spectroscopy**, this handbook).

Through equation (13) and the summation over all possible ground and excited quantum states (including continua) of the atoms in the medium, the effective nonlinear susceptibility for all combinations of wavelengths is governed by the quantum-mechanical properties of the species.

2.6 Exact Harmonics and Frequency Shifts

Nonlinear optical harmonic conversion processes can be considered as parametric processes, in which no energy exchange occurs with the medium. This implies that exact harmonics ω_n are produced at frequencies

$$\omega_n = n \times \omega_f \tag{14}$$

where ω_f is the fundamental frequency of the laser beam. Harmonic conversion can take place only at high intensities, i.e., with laser pulses of limited durations, at which these intensities can be maintained; this may have consequences for the simple relationship of equation (14). Laser pulses of short duration have a certain nonzero bandwidth $\Delta\omega_f$, with a lower bound set by the Fourier limit. Here, the frequency *profiles* in the time and the frequency domain are connected. In the ideal case of an exactly Fourier-limited pulse of Gaussian profile in the frequency domain, the bandwidth of the nth harmonic is given by $\sqrt{n} \times \Delta\omega_f$,

where in the case of an FT-limited pulse of Lorentzian profile this would be $n \times \Delta\omega_f$. For pulses with chirp, exhibiting a frequency that is not constant over time, i.e., $\omega_f(t)$, a convolution must be made over the nonlinear conversion process to determine the frequency profile of the generated pulses.

When a laser beam experiences a time-dependent refractive index, the phase $\phi(z, t)$ of the radiation field is modulated by

$$\phi(z, t) = -\frac{\partial n}{\partial t} \tag{15}$$

These temporal phase excursions cause a chirp, i.e., a time-dependent frequency of the field propagation along the z-direction:

$$f(t) = \frac{1}{2\pi} \frac{\partial \phi(z, t)}{\partial t} \tag{16}$$

Here, one might distinguish between different physical phenomena that have similar effects. First, the incident laser pulses may have a chirp that originates in the production process of the laser pulses. This is often a result of time-dependent gain in a medium in which laser oscillation or amplification takes place; during build-up of a population inversion, the increase (or the decrease) in index of refraction is a natural effect. A phase modulation may also be picked up when a high-power laser beam traverses a medium with a nonlinear refractive index (Kerr effect); a part of the laser pulse at higher intensities experiences a different index. If such a chirped laser pulse is harmonically converted, it may result in an harmonic that deviates n times from the fundamental ω_f. The frequency chirp induced in the different stages of optical amplification and upconversion can easily lead to calibration errors on the order of 100 MHz. These phenomena have been discussed by a number of investigators aiming at precision experiments with UV and XUV pulses (Wieman and Hänsch 1980, Fee *et al*. 1992, Melikechi *et al*. 1994, Eikema *et al*. 1997, Reinhard *et al*. 1996).

In addition, the harmonic conversion processes itself can be associated with chirp-induced deviations from exact multiples of the fundamental frequency in the harmonic content. The high intensity in the focal region may give rise to ionization; the free electrons produced lower the local refractive index substantially, thus phase-modulating the laser beam. Since in the plasma $n \to 0$, hence $\partial n/\partial t < 0$, this gives rise to a temporal blue shift in the harmonics, when strong ionization occurs. This phenomenon, often observed in harmonic conversion with femtosecond lasers (Macklin *et al*. 1993, Wahlstrom *et al*. 1993), also played a significant role in a precision experiment using fifth harmonic generation, as displayed in Figure 7. The absolute frequency of the fifth harmonic, as produced in different gaseous media, is measured against an atomic ruler, the He resonance line at 58.4 nm. In the case of harmonic generation in acetylene no or little ionization of the interacting medium takes place, while ionization is very strong in xenon. In the latter case, a blue shift is induced, which is observed when measuring an atomic resonance.

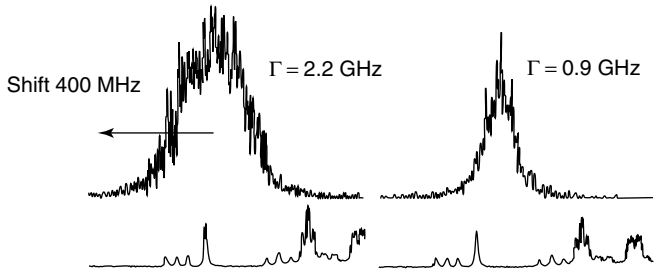

Figure 7 Effect of ionization in the focal region: here, it is demonstrated for a fifth-order harmonic conversion process, where powerful laser pulses (50 mJ of UV at 292 nm in a 30 μm focus, in 4 ns) are converted into pulses at 58.4 nm. The produced wavelength at 58.4 nm is scanned over the He resonance line, whereas the frequency of the fundamental (at 584 nm, before frequency-doubling) is referenced against I_2 saturated lines (lower spectrum). A comparison is made by producing the fifth harmonic in C_2H_2 (right: low level of ionization) and in Xe (left: high level of ionization). The red shift in the spectrum on the left is interpreted as a blue shift of the fifth harmonic radiation. Note also that the additional broadening in the case of nonlinear conversion in Xe. [Reproduced from Eikema *et al*. (1997).]

2.7 Third-harmonic Generation in Pulsed Jets

From a practical perspective, coherent beams of XUV radiation are elegantly produced by focusing intense laser beams in pulsed jets, following the method invented by Kung (1983). In most applications, nanosecond-pulsed lasers (with pulse durations of ≈ 5 ns) are used, due to the abundant availability of Q-switched Nd:YAG lasers and because time durations of 5 ns provide a good compromise (Fourier argument) between achieving high intensities and narrow bandwidths. Initially, commercial pulsed-dye lasers (PDLs) were applied to provide the wanted tunability, but the bandwidth of such systems is limited by the gratings applied in the dye oscillators. Later pulsed-dye amplification (PDA) systems, injection seeded by continuous wave (CW) ring dye lasers, were applied to obtain nearly Fourier-transform-limited pulses in the regime of the XUV. This was first explored by Kung *et al*. (Cromwell *et al*. 1989) and later applied in many high-resolution spectroscopic studies by Ubachs and coworkers (Ubachs *et al*. 1997) and by Merkt and coworkers (Hollenstein *et al*. 2000).

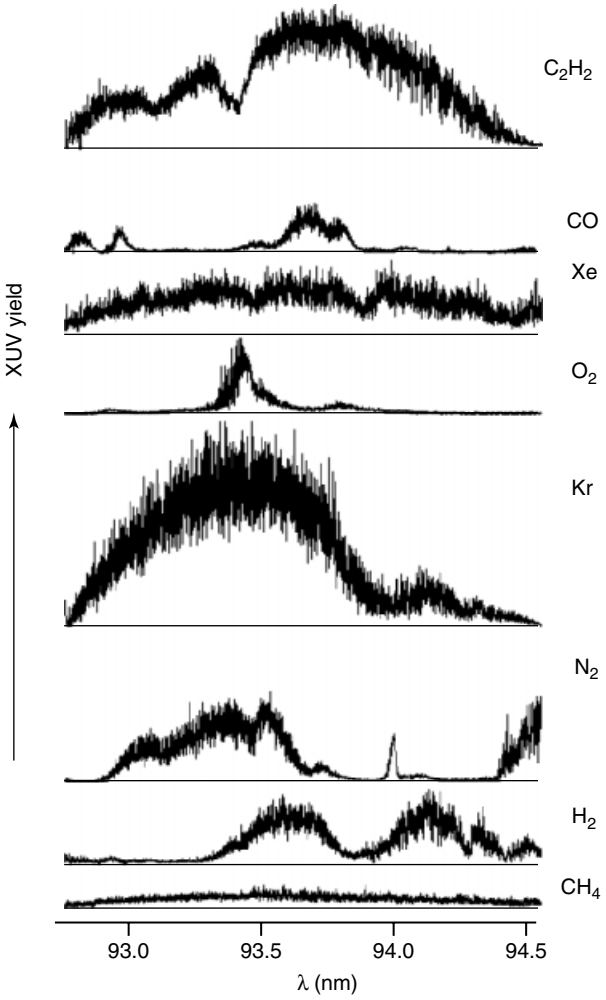

Figure 8 The efficiency of XUV production in various gases (as indicated) via direct third-harmonic generation of the frequency-doubled output of a pulsed-dye laser covering the range of Rhodamine-6G dye. The XUV was produced underneath a pulsed valve with 0.8 mm orifice. [Adapted from Hinnen (1997).]

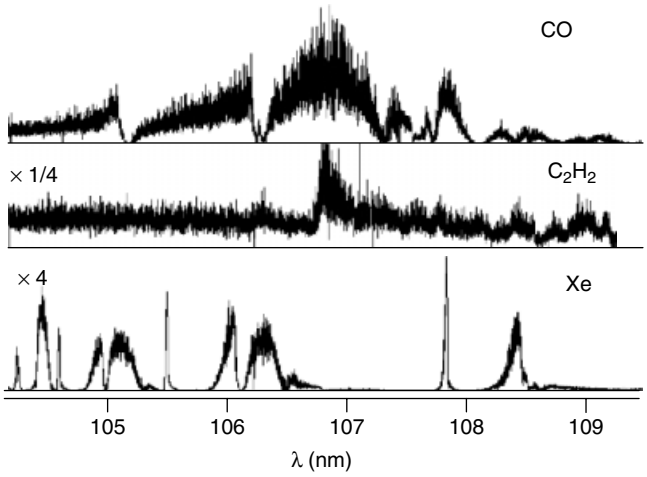

Figure 9 The efficiency of XUV production in carbon monoxide, acetylene, and xenon gases via direct third-harmonic generation of the frequency-doubled output of a pulsed-dye laser covering the range of DCM dye covering the wavelength range 104–109 nm. [Adapted from Hinnen (1997).]

Two routes are being explored in the production and the application of tunable and coherent narrowband XUV radiation. On the one hand, the sum-frequency schemes employing the strong resonance enhancement effects on two-photon transitions in the noble gases (Miyazaki *et al*. 1989). This method has the advantages of achieving higher XUV yield and greater flexibility; however, it requires two independently tuneable laser systems, which make the setup more costly. On the other hand, nonresonant THG from intense frequency-doubled output pulses of a PDA system is capable of covering an important part of the XUV domain (90–115) where many atoms and molecules exhibit important absorption systems. In studies where calibration of the XUV light at the highest accuracy is required, direct THG may be advantageous, since only a single tunable laser requires calibration (Eikema *et al*. 1997). Here, we focus on direct THG.

The efficiency of nonresonant third-harmonic production, starting with intense frequency-doubled pulses in the UV domain, depends on many parameters. Phase matching, in the plane-wave regime, depends on the focal conditions and on the dispersion properties of the gaseous media used. Furthermore, the nonlinear susceptibility and, hence, the quantum-mechanical level structure of the atoms in the medium play a role with many possible near resonances at the one-, two-, and three-photon level. In addition, (linear) reabsorption in the focal region by the medium may affect the practical XUV yield. In Figures 8 and 9, experimentally determined harmonic conversion yields are displayed as measured under conditions of pulsed jets with 0.8 mm orifice, UV energies of ≈ 25 mJ in 5 ns pulses, focal length $f = 25$ cm, and estimated gas density of 20 torr approximately 0.5 mm below the orifice in the jet expansion (Hinnen 1997).

Harmonic yield curves, as displayed in Figures 8 and 9, are useful when choosing the optimal medium for efficient THG. Xenon is often a medium of choice for THG, since it exhibits a fair third-order nonlinear susceptibility over the entire XUV wavelength region; in the range 105–110 nm, however, there exist gaps in the yield curves with virtually no third-harmonic production; then, CO and acetylene are good alternatives. It should be noted that the efficiency curves are not universal; the efficiency depends on the choice of geometry (b parameter and numerical aperture) and on the intensity, since saturation effects play a role at high input energies of the incident laser beams. In addition, in some media, optical breakdown occurs at

some choices of b, laser intensity, and gas density. Under conditions of severe breakdown, X-rays are produced in the plasma, which will propagate into the spectroscopy zone, where the species will be nonresonantly ionized, hampering the spectroscopic studies. Ionization of the medium will also give rise to frequency chirp effects in the harmonic conversion (see Figure 7).

2.8 Polarization Properties

The third-order nonlinear susceptibility of a medium, expressed by equation (13), is an intricate function. The factors in the denominator give rise to resonance enhancement effects matching the quantum-mechanical level structure of the atoms contained in a medium. However, the resonances that are connected in the dipole matrix elements in the nominator play a role. These dipole matrix elements can be reduced, using the Wigner–Eckart theorem, to

$$\begin{aligned} < i|\boldsymbol{r}_k|j > &= < J_i, M_i|\boldsymbol{r}_q^{(1)}|J_j, M_j > \\ &= (-)^{J_i - M_i} \begin{pmatrix} J_i & 1 & J_j \\ -M_i & q & M_j \end{pmatrix} \\ &\quad \times < J_i, M_i \| \boldsymbol{r}^{(1)} \| J_j, M_j > \end{aligned} \tag{17}$$

where q represents polarizations in spherical tensor components ($q = 0$ for linearly polarized light and $q = \pm 1$ for circularly polarized light). The numbers J and M relate to the angular momentum properties of the quantum states of the atoms involved.

These dipole matrix elements can be substituted in the equation for the nonlinear susceptibility, equation (13), which then yields a coherent sum over four dipole matrix elements to represent a coherent *four-wave mixing* process. In this way, the susceptibility $\chi^{(3)}$ acquires a tensor nature, and the polarizations of the (three) input beams define the polarization of the (fourth) generated beam. Each dipole matrix element contains a projection of an electromagnetic field vector onto the transition dipole vector of the atom (or the molecule). This projection can be evaluated in terms of the $3j$ symbol, as in equation (17), leading, for the four-photon process, to

$$\begin{aligned} \chi^{(3)} \propto & \begin{pmatrix} J_i & 1 & J_g \\ -M_i & q_1 & M_g \end{pmatrix} \begin{pmatrix} J_j & 1 & J_i \\ -M_j & q_2 & M_i \end{pmatrix} \\ & \times \begin{pmatrix} J_k & 1 & J_j \\ -M_k & q_3 & M_j \end{pmatrix} \begin{pmatrix} J_g & 1 & J_k \\ -M_g & q_4 & M_k \end{pmatrix} \end{aligned} \tag{18}$$

In a *parametric* four-wave mixing process, in which there is no exchange of energy between the radiation fields and the atoms in the medium (hence no excitation), in each possible process, a four-photon cycle occurs, starting in an initial state (here limited to ground states $|g >$) and ending in the same state, with the same quantum numbers.

This procedure then defines the polarization properties of the generated field at frequency ω_4. The coherent cycle should always exhibit $\Delta M = 0$, and from this it follows that a process with $q_1 = q_2 = q_3 = 1$ cannot lead to a generated field at ω_4. Hence, THG with circularly polarized light is not possible. Combinations of incident fields with arbitrary polarizations can, however, lead to a newly generated field exhibiting circular polarization. In the special case of two-photon resonance enhancement (either the two-photon resonant sum or the difference-frequency mixing process), the quantum level after two-photon exchanges sets some additional constraints on the polarizations. In the case of processes with $J = 0$ or $J = 2$ intermediate states (as often employed in two-photon resonant sum- and difference-frequency mixing in noble gases), the summation over the two-photon excited state $|J_k, M_k >$ is replaced by fixing to the quantum numbers of the intermediate state in the resonance enhancement processes.

2.9 Continuous-wave VUV Production

In view of the smallness of third-order nonlinear susceptibilities, the high intensities of pulsed lasers (at peak powers of multiple kilowatts) are required to generate any radiation in the VUV domain. Some initial studies of the production of coherent VUV radiation with CW laser radiation were performed by Wallenstein and coworkers. In these attempts resonance enhancement of $\chi^{(3)}$ plays an important role to compensate for the low intensities. Powers of picowatts at 143 nm were produced in four-wave mixing in Mg vapor (Timmermann and Wallenstein 1983) and powers up to 20 nW at 192 nm in Sr vapor (Nolting and Wallenstein 1990).

Threefold resonance enhancement applying a wave-mixing scheme in atomic mercury vapor with a near-resonant wavelength at 257 nm (absorption should be avoided), an exact resonance at the two-photon level (7*s* level in Hg) with radiation at 399 nm, and a resonance near the 11p and 12p Rydberg states at the three-photon level was used to generate narrowband CW radiation at the Lyman-α wavelength of 121.56 nm (Eikema *et al.* 1999). Optimizing laser powers and the Hg vapor pressure in the interaction region contained in a heat pipe yielded a VUV-generation yield curve, as displayed in Figure 10. The shortest wavelength achieved was 119 nm. At optimum conditions, some 20 nW of radiation at Lyman-α was produced (Eikema *et al.* 2001). CW radiation in the XUV windowless regime has not yet been reported.

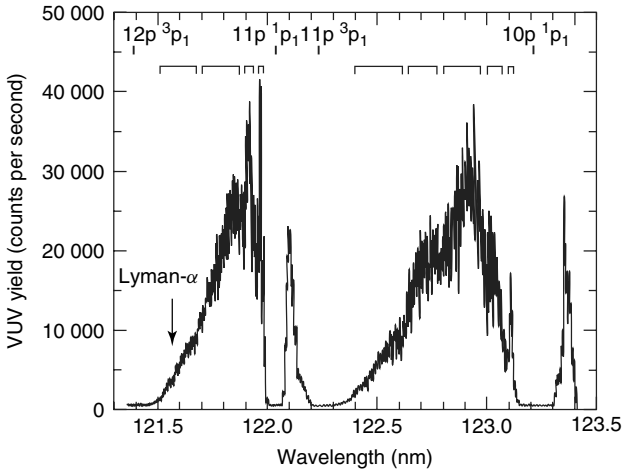

Figure 10 Continuous four-wave mixing yield in Hg vapor using threefold resonance enhancement, with the resonances at the three-photon level indicated. [Adapted from Eikema *et al*. (1999).]

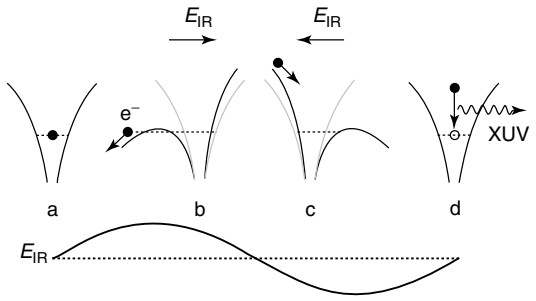

Figure 11 Pictorial representation of the three-step model: (a) field-free Coulomb potential for a bound electron; (b) tunneling ionization and classical motion of the electron in the IR laser field; (c) IR-field reversal and return of the electron wavepacket; and (d) recombination of the electron wavepacket and subsequent emission of harmonic radiation.

2.10 The Nonperturbative Plateau Regime

Breakdown of the perturbative model intuitively follows by considering the contribution of higher order terms in the expansion equation (1). If the electric field intensities $|\boldsymbol{E}|$ become so high as to match the condition

$$\chi^{(2n+3)}|\boldsymbol{E}|^2 \approx \chi^{(2n+1)} \tag{19}$$

then the perturbative expansion fails and all terms should be taken into account.

At the high intensities for which the condition of equation (19) holds, harmonics are easily generated as was experimentally investigated since the 1980s (Ferray *et al*. 1988, Wildenauer 1987). A crucial finding is the observation of a characteristic *plateau* of sequential harmonics —again only odd harmonics will be produced for symmetry reasons—that terminate at a certain cutoff energy. A theory has been put forward in classical terms that explains the phenomenon of *high* harmonic generation (HHG), which is known as the *collisional* or *three-step* model (Corkum 1993, Krause *et al*. 1992, Lewenstein *et al*. 1994). The model is represented in Figure 11. The first step is a lowering of the Coulomb potential on one side due to the electric field of the laser field, leading to tunneling ionization of the electron. In the second step, this electron wavepacket is accelerated away from the remaining ion by the light field, but it reverses direction when the field reverses polarity. In the third step, when the wavepacket again comes close to the ionic core, kinetic energy of the electron can be converted into emission of short-wavelength radiation. In this model, the maximum energy acquired by the electron, and therefore the emitted harmonic, depends on the ionization energy of the medium (I_p), the pondoromotive potential U_p of the electron, and the frequency of the incident radiation ω:

$$E_{\max} = I_p + 3.17U_p \tag{20}$$

The pondoromotive potential U_p (the mean kinetic energy of an electron in a oscillating field) is equal to

$$U_p = e^2E_0^2/4\omega^2m_e \tag{21}$$

where e is the electron charge, E_0 the electric field amplitude, and m_e the mass of the electron. The quadratic dependence on electric field means that the cutoff energy is linearly proportional to the laser intensity. From equation (21), it is also clear that longer laser wavelengths can, in principle, lead to shorter wavelengths in the HHG process.

The intensities required for reaching the plateau of harmonics can only be achieved when using ultrashort lasers pulses that have intrinsically broad bandwidths (Fourier principle) and are by themselves not useful in high-resolution spectroscopic studies. An intermediate regime was investigated with pulses of rather long duration (of some 300 ps) and intensities sufficient to reach the harmonics plateau. This is described in Section 4. If the coherence between consecutive pulses from an ultrafast mode-locked laser can be used, in particular with frequency comb lasers, the time-domain properties of the laser pulses can be used to unravel atomic properties at high accuracies. This is discussed in Section 5.

3 XUV SPECTROSCOPY WITH NANOSECOND PULSES

High-resolution spectroscopy in the XUV domain has a certain limitation of scope in the sense that there exist

only a limited number of atomic and molecular species that exhibit narrow features at high energies. Moreover, the requirement of high resolution pertains only to studies in the gas phase. Most atoms and molecules have an ionization potential below 10 eV and above that range broadly structured ionization continua exist. Similarly, dissociation limits of molecules are in almost all cases lower than 10 eV, and above their first dissociation limit, molecules often display broad continuum dissociative resonances. A notable exception forms the investigation of Rydberg states of high principal quantum number. Even in strongly dissociating molecules in the region below the ionization limit, extremely narrow resonances are found. This is exploited in methods of Rydberg-resolved zero-kinetic energy photoelectron spectroscopy (Seiler *et al.* 2001), providing information on the structure of ground states of molecular ions.

Here, we focus on a few topics where high-resolution spectroscopy in the XUV domain has yielded significant results. First, the noble gases have a level structure that is densely packed close to the ionization limit, but a single ground electronic state is isolated and distant in energy, e.g., in the He atom all excited levels are within 4 eV, whereas the ground state is 20 eV below the dense manifold of excited states. The other noble gas atoms exhibit a similar level structure. In this realm, a narrowband XUV laser was used to perform accurate calibration of the resonance lines in the noble gases. Accurate frequency calibration of a single line then determines the excitation energies of all electronic states and the value of the ionization potential.

In molecules, there are three examples where a narrowband XUV laser has a significant impact in the determination of the physical properties. Both the isoelectronic systems CO and N_2, exhibiting by far the strongest chemical bonds (the largest dissociation energies), display a complicated excited state level structure, severely perturbed and characterized by Rydberg-valence interactions. In addition, the mutually perturbing singlet states interact with triplet states, causing predissociation as a general phenomenon. However, each of the singlet states couples in a different manner to the triplet manifold, giving rise to a richness of spectral features, some of which are highlighted below. The spectra of these molecules have important consequences. Carbon monoxide is the second most abundant species in the universe, and its (pre)dissociation properties are known to govern the chemical dynamics of interstellar clouds. Nitrogen is the most abundant species in the Earth's atmosphere, and the dipole-allowed XUV absorption spectrum shields the Earth's surface from the hazardous XUV components of the solar flux.

The hydrogen molecule is a case by itself. It exhibits the Lyman and Werner absorption bands, representing the most ubiquitous molecular absorption features occurring in interstellar clouds and in early objects in the universe. Precision spectroscopies of these systems performed by high-resolution XUV laser spectroscopy are presented below.

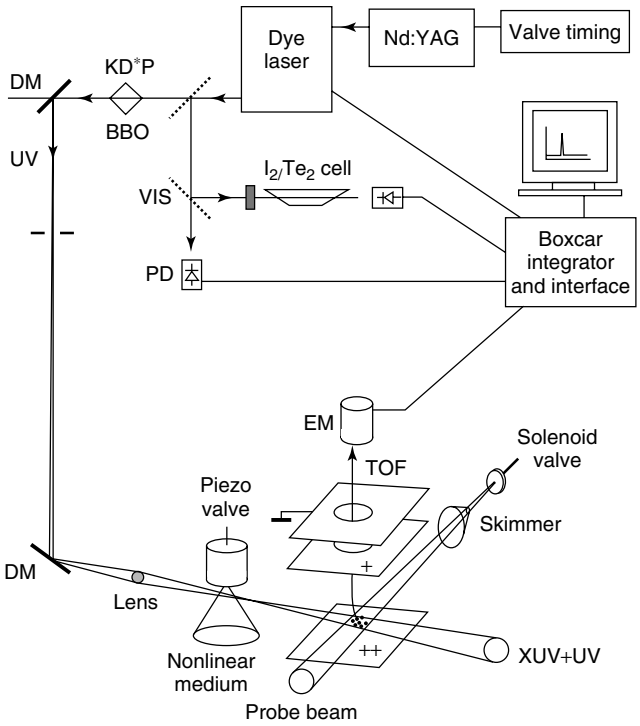

Figure 12 Schematic of a generic setup used for XUV laser spectroscopy. An Nd : YAG-pumped dye laser system delivers tunable radiation at wavelengths 410–680 nm in pulses of 5 ns duration. Frequency doubling takes place either in a KD*P crystal (for the yellow-red range) or in a BBO crystal (for the blue-green range). The UV light is separated from the fundamental on dichroic mirrors (DM) and focused underneath the orifice of the pulsed jet. Overlapping XUV beams and UV beams propagate into a differentially pumped interaction chamber, where they are perpendicularly crossed with an atomic or a molecular beam. The overlapping beams are used in 1XUV + 1UV photoionization to record spectra of the resonant states. Ions are detected after time-of-flight mass-separation. In this configuration using the pulsed-dye lasers, the bandwidth of the tunable XUV radiation is 0.25–0.30 cm^{-1}. Wavelength calibration results from simultaneous recording of absorption spectra of I_2 in the red-yellow-green range and in Te_2 in the blue range.

3.1 Experimental Consideration

In the spectroscopic investigations, XUV radiation is produced via frequency-doubling of tunable laser radiation from a PDL and subsequent frequency-tripling in a gas jet. A generic setup is displayed in Figure 12, with a description of some details given in the caption. The choice is crucial between commercial PDLs, yielding a bandwidth of 0.25–0.30 cm^{-1} for the tunable XUV radiation, and the use of a PDA system, where the output of a CW ring dye

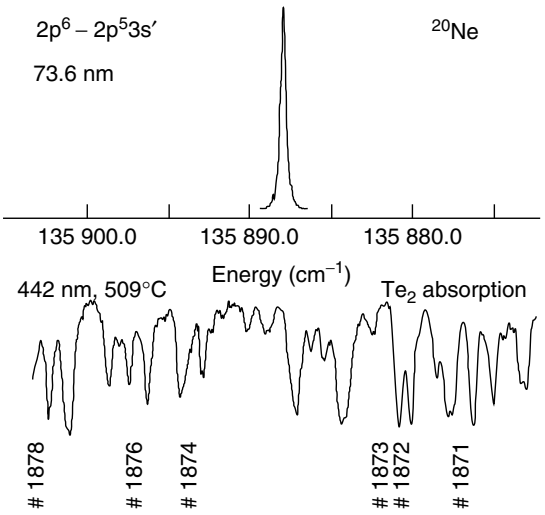

Figure 13 Upper trace : Spectrum of the (3s′) resonance line in the Ne atom at 73 nm, recorded using the third harmonic of a frequency-doubled pulsed-dye laser. Lower trace: absorption spectrum of $^{130}Te_2$ using the lines indicated by numbers from the Te_2 reference atlas (Cariou and Luc 1980). [Adapted from Eikema *et al*. (1994b).]

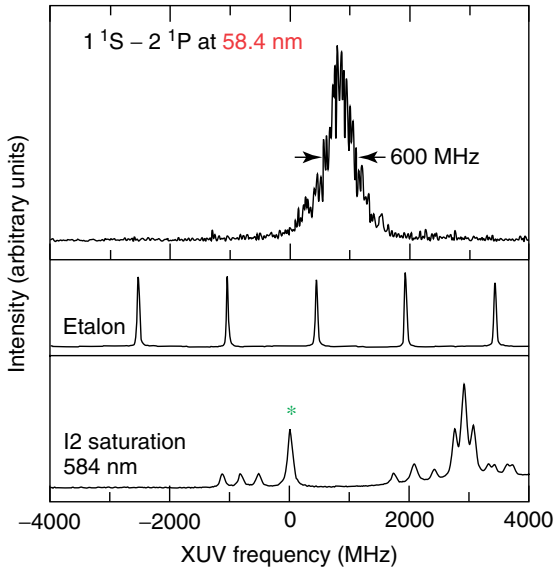

Figure 14 Upper: Recorded spectrum in the precision experiment on the $(1s)^2\,{}^1S_0-(1s)(2p)\,{}^1P_1$ transition in the He atom at 58.4 nm, using the 10th harmonic of a pulsed-dye laser; Middle: Transmission fringes of a stabilized etalon with FSR = 148.9567 MHz; Lower: Saturated absorption spectrum in I_2 with the line marked by (*) calibrated at 513 049 427.1 (1.7) MHz. [Adapted from Eikema *et al*. (1997).]

laser is amplified and upconverted, leading to an improved bandwidth of 0.01 cm^{-1}. The PDLs have slightly better flexibility and a wider operation range.

3.2 Accurate Calibration of Noble Gas Resonance Lines

All the noble gases exhibit strong resonance lines in the range of the XUV. For all noble gas elements except radon, resonance lines were calibrated, and selected results are given in Table 1. For Ne, the (3s) and (3s′) resonance lines are at $\lambda = 73-74$ nm. These wavelengths can be produced by pumping a blue dye laser with the third harmonic of a Nd:YAG laser, and frequency-doubling the output in BBO crystals. Frequency-tripling in a xenon jet then delivers the XUV at 73–74 nm, though at low-intensity levels (Eikema *et al*. 1994b). A recorded spectrum of the (3s′) line is shown in Figure 13, and calibration is performed by recording an on-line absorption spectrum of Te_2 molecules formed in a heated (509 °C) and isotopically enriched sample of $^{130}Te_2$ (Cariou and Luc 1980).

Resonance lines of Ar, Kr, and Xe have been measured using the narrowband PDA-based XUV lasers at instrumental widths of some 300 MHz (or 0.01 cm^{-1}). The first study was performed with the first such narrowband source developed at Berkeley (Trickl *et al*. 1989) on several lines of Kr, while later the Amsterdam system was employed to investigate lines in several heavy noble gases (Velchev *et al*. 1999, Brandi *et al*. 2001, 2002). In all of these studies, accurate measurements were performed on transition frequencies, as well on isotope shifts and hyperfine structures in the odd isotopes.

The He atom is a special and exemplary case. The transition wavelength of the $(1s)^2\,{}^1S_0-(1s)(2p)\,{}^1P_1$ line is at 58.4 nm or 21 eV. Tunable XUV radiation in this range could be produced by running a PDA laser system at 584 nm in the visible domain, and then pursue frequency-doubling and subsequent fifth harmonic conversion in a gas jet (Eikema *et al*. 1997). A characteristic spectrum, displayed in Figure 14, shows some essential aspects of the absolute frequency calibration for the ^{4}He line. The linewidth of the resonance is 600 MHz, determined in part by natural lifetime broadening ($\tau = 0.3$ ns), residual Doppler broadening, and the bandwidth of the XUV source (300 MHz). An I_2 hyperfine component, measured online via saturation spectroscopy using the CW output of the seed laser, served as the absolute frequency marker at the fundamental wavelength. Crucial in the absolute frequency calibration was the assessment of chirp effects originating in the PDA system, and propagating into the frequency profile of the XUV radiation, even to the extent that chirp-compensation was applied with an electro-optic modulator, placed in the CW beam before amplification. Chirp induced by phase modulation in the focal region of the gas jet, where the harmonic conversion takes place, was assessed by investigating the line shift under conditions of ionization (Xe as nonlinear medium) or acetylene; see also Figure 7.

Table 1 Accurately calibrated resonance lines for the various noble gas atoms.

Atom	Spectral line	Frequency	Unc.	Reference
^{4}He	$(1s)^2 \rightarrow (1s)(2p)\,^1P_1$	171 134.8950	(15)	(Eikema *et al*. 1997)
^{20}Ne	$(2p)^6 \rightarrow (2p)^5(3s)[\frac{3}{2}]_1$	134 459.33	(5)	(Eikema *et al*. 1994b)
^{20}Ne	$(2p)^6 \rightarrow (2p)^5(3s')[\frac{1}{2}]_1$	135 888.73	(5)	(Eikema *et al*. 1994b)
^{40}Ar	$(3p)^6 \rightarrow (3p)^5(4s')[\frac{1}{2}]_1$	95 399.833	(3)	(Velchev *et al*. 1999)
^{86}Kr	$(4p)^6 \rightarrow (4p)^5(5s')[\frac{1}{2}]_1$	85 846.700	(8)	(Trickl *et al*. 1989)
^{86}Kr	$(4p)^6 \rightarrow (4p)^5(5d)[\frac{1}{2}]_1$	103 801.8002	(12)	(Brandi *et al*. 2002)
^{86}Kr	$(4p)^6 \rightarrow (4p)^5(6s')[\frac{1}{2}]_1$	105 146.309	(14)	(Trickl *et al*. 1989)
^{86}Kr	$(4p)^6 \rightarrow (4p)^5(6s)[\frac{3}{2}]_1$	99 894.0337	(73)	(Trickl *et al*. 1989)
^{86}Kr	$(4p)^6 \rightarrow (4p)^5(6s)[\frac{3}{2}]_1$	99 894.0528	(14)	(Brandi *et al*. 2002)
^{86}Kr	$(4p)^6 \rightarrow (4p)^5(7s)[\frac{3}{2}]_1$	105 770.696	(7)	(Trickl *et al*. 1989)
^{136}Xe	$(5p)^6 \rightarrow (5p)^5(7s')[\frac{1}{2}]_1$	95 800.5867	(30)	(Brandi *et al*. 2001)
^{136}Xe	$(5p)^6 \rightarrow (5p)^5(8d)[\frac{1}{2}]_1$	94 228.0187	(32)	(Brandi *et al*. 2001)
^{136}Xe	$(5p)^6 \rightarrow (5p)^5(8d)[\frac{3}{2}]_1$	94 685.4822	(30)	(Brandi *et al*. 2001)

The spectral positions and their uncertainties are expressed in cm^{-1}. The uncertainty refers to the last digits in the stated frequency.

The importance of the absolute calibration of the He resonance line lies in the possibility to deduce a value for the Lamb shift in the ground state of this two-electron system. In fact, determination of the XUV laser by Eikema *et al*., first with a PDL system delivering a bandwidth of 0.5 cm^{-1} (Eikema *et al*. 1993) and later with a PDA system at further improved resolution (Eikema *et al*. 1997), was the first measurement after the original study of Herzberg (1958) based on classical spectroscopy. Although Herzberg compared the 1958 experimental value with the then existing calculations of the ground-state Lamb shift in He (Kabir and Salpeter 1957, Sucher 1958), the laser-based result yielding an absolute transition frequency of 5 130 495 083 (35) MHz could be compared with more sophisticated ab initio calculations of He, which had reached a level of accuracy, at which the non-QED part could be considered exact (Drake *et al*. 1993). From a comparison between experiment and non-QED theory, a value for the Lamb shift of 41 224 (45) MHz could be deduced, which was at the time in very good agreement with theoretical prediction of the Lamb shift from QED calculations: 41 233 (35) MHz. Bergeson and coworkers performed an alternative experiment on the ground state of the helium atom: Doppler-free excitation of the $(1s)^2\,^1S_0-(1s)(2s)\,^1S_0$ two-photon resonance by employing pulsed Fourier-transform-limited VUV radiation at 120 nm (Bergeson *et al*. 1998). This experiment resulted in a value of 41 104 (48) MHz for the Lamb shift. Since the time of these experiments (publications in 1997 and 1998), improved calculations have been performed (Drake and Yan 2008), yielding slightly larger discrepancies.

3.3 Predissociation Phenomena in Carbon Monoxide

The spectrum of carbon monoxide is one of utmost complexity. The dissociation of CO is at 89 460 cm^{-1} and the entire energy region up to the ionization threshold at $113\,027.367 \pm 0.016\,cm^{-1}$ (Seiler 2004) is full of discrete and slightly more diffuse absorption features that have been difficult to assign. In the span between the dissociation and ionization thresholds, predissociation is the dominant phenomenon. A seemingly erratic behavior of spectral features, which strongly vary in width over adjoining vibrational levels, is observed. In addition, the predissociation widths were found to differ by orders of magnitude for the various $^{x}C^{y}O$ isotopomers.

The sequences of Rydberg states are known to interact with the valence states, which exhibit potential wells at larger internuclear separation than that in the Rydberg states. In Figure 15 some relevant potential energy curves are plotted. The low-lying $D'\,^1\Sigma^+$ state, identified in emission (Wolk and Rich 1983), has an inner curve that crosses all of the Rydberg states, thus causing those states to predissociate. This phenomenon starts with the lowest lying $(3s\sigma)$ member of the singlet Rydberg series, denoted as the $B^1\Sigma^+$ state, of which the two lowest lying vibrational levels are not yet subject to predissociation. This interaction was extensively studied (Tchang-Brillet *et al*. 1992, Baker *et al*. 1995) in quantitative terms. At slightly higher excitation energy, there is, in an adiabatic picture, the $C'\,^1\Sigma^+$ state, calculated as $4^1\Sigma^+$ in ab initio potential calculations (Cooper and Langhoff 1981).

The XUV absorption spectrum of CO was investigated using all available spectroscopic instruments.

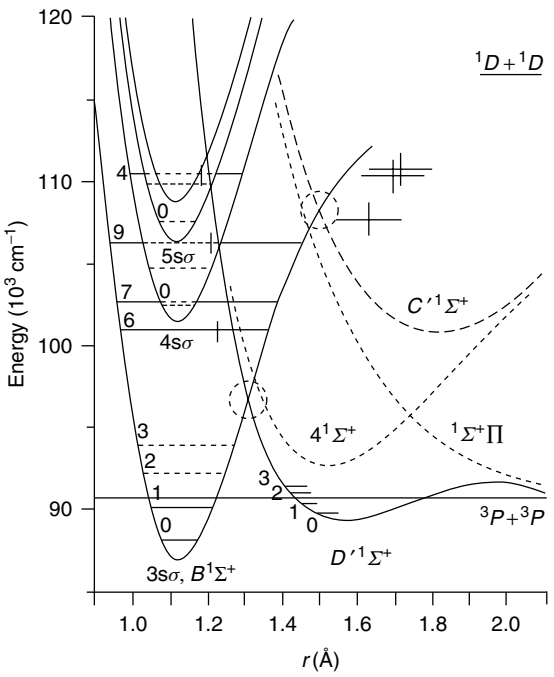

Figure 15 Potential energy diagram for the carbon monoxide molecule. [Reproduced from Eidelsberg *et al.* (2004).]

The low-resolution synchrotron absorption spectrum (Letzelter *et al.* 1987) gives an overview of all the features to be detected. Initially, Casey investigated CO at the 10-m grating spectrograph at the National Research Council in Ottawa, reaching a resolution of 0.7 cm^{-1}. This spectrum remained unpublished except for a PhD Thesis work (Casey 1978). Further, high-resolution studies were performed at the 10.6 m VUV spectrograph of the Observatoire de Paris in Meudon, using a vacuum spark VUV source synchronized with a pulsed jet expansion of CO; thus, low-temperature absorption spectra of four different isotopomers of carbon monoxide ($^{12}C^{16}O$, $^{13}C^{16}O$, $^{12}C^{18}O$, and $^{13}C^{18}O$) were recorded over a wide wavelength range (Eidelsberg *et al.* 1991). The resolution in this study was slightly better than 1 cm^{-1} and the obtained low-temperature Boltzmann populations (10–20 K) allowed for unraveling the bandhead structures. Similarly, a 6.65-m VUV spectrograph, mounted on a synchrotron beam line at the Photon Factory Facility in Tsukuba, Japan, allowed for high-resolution jet absorption experiments at 0.5 cm^{-1} resolution.

XUV laser excitation studies, using 1XUV + 1UV photoionization for detection, were performed with the Amsterdam XUV laser system, first with the PDL-based system, yielding 0.3 cm^{-1} resolution (Eikema *et al.* 1994a) and later with the PDA system and a much improved resolution of 0.01 cm^{-1} (Ubachs *et al.* 1997). Additional information on the highly excited states of CO, in particular on the higher principal quantum number Rydberg states, was obtained from multistep laser excitation studies performed by Ebata and coworkers (Ebata *et al.* 1992, Komatsu *et al.* 1993).

We present a typical example of how the laser-based XUV spectroscopy has aided in the understanding of the spectroscopy and the dynamics of electronically excited states of CO. In Figure 16, the recorded 1XUV + 1UV photoionization spectrum of the (4pπ) $L^1\Pi - X^1\Sigma^+$ (0,0) band of $^{12}C^{16}O$ is displayed, showing effects of rotational-state-dependent predissociation in a number of ways. The linewidths in the R and P branches broaden with increase in rotational state, which is indicative of enhanced predissociation. The natural line broadening Γ, which can

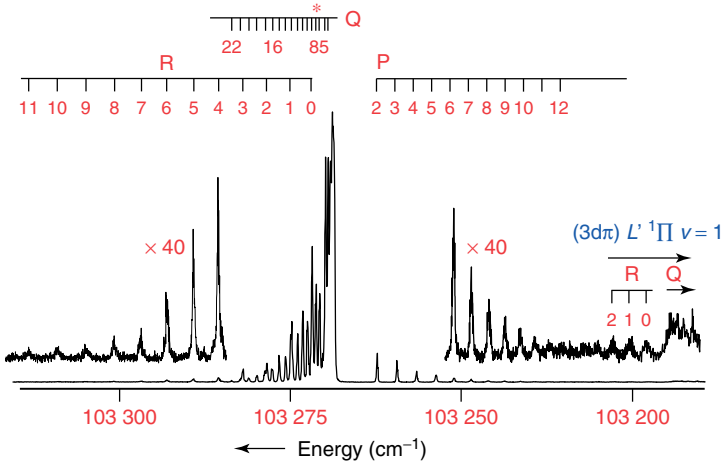

Figure 16 Spectrum of the (4pπ) $L^1\Pi - X^1\Sigma^+$ (0,0) band of $^{12}C^{16}O$. The increasing linewidth in both the P and R branches toward higher rotational states is crucial. On the right-hand side, another band appears, unrelated to the 4pπ state. [Reproduced from Eikema, K.S.E., Hogervorst, W., and Ubachs, W. (1994a) Predissociation rates in carbon-monoxide—dependence on rotational state, parity and isotope. *Chemical Physics*, **181**(1–2), 217–245. © 1994, with permission from Elsevier.]

be deconvoluted from the observed linewidth $\Delta\nu$, is a measure of the lifetime τ, and it can be related to the predisssociation rate of the excited state:

$$k_{\text{pred}} = 2\pi\Gamma = \frac{1}{\tau} \tag{22}$$

Additional information on the excited state lifetimes is contained in the line intensities. In $1+1$ photoionization, the line intensity depends on the lifetime of the intermediate state when τ becomes smaller than the duration of the exciting laser pulses, where the competition between predissociative decay and the photoionization process weakens the predissociated lines. It can be shown that the line intensity under those conditions is (Eikema *et al*. 1994a)

$$I \propto \tau \tag{23}$$

As a result, this proportionality relation of the line intensities within a band can be used to determine relative predissociation rates $k_{\text{pred}}(J)$ for rotational levels within a vibrational manifold. For the case of the $(4p\pi)\,L^1\Pi, v=0$ state, the information on line broadening and intensity can be converted into predissociation rate, as displayed in Figure 17.

This particular case of predissociation is a typical example where the mechanism of rotational coupling with the $D'\,^1\Sigma^+$ state plays a role via the matrix element:

$$< D'\,^1\Sigma^+|\boldsymbol{L}_-\boldsymbol{R}_+|L^1\Pi > \propto \sqrt{J(J+1)} \tag{24}$$

Such an off-diagonal matrix element explains the typical behavior of a predissociating $^1\Pi$ state, interacting with the inner potential well of the $D'\,^1\Sigma^+$ state. The vibrational part of the matrix element can be separated and equation (24) yields a rotationally dependent predissociation scaling with $J(J+1)$, as is indeed found in Figure 17. Note that there is only coupling between the (e)-parity levels in the double degenerate Π state, while the (f)-parity states are unaffected by predissociation. This is indeed the case in the $(4p\pi)\,^1\Pi, v=0$ state in CO (Eikema *et al*. 1994a); in a later study at much improved resolution, an additional predissociation effect at much smaller k_{pred} was detected, holding only for (f)-parity components and exhibiting rotational-state independence (Cacciani *et al*. 2002).

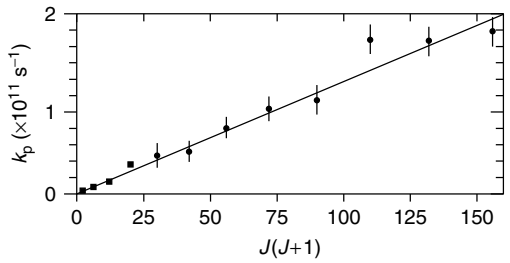

Figure 17 Predissociation rates of rotational quantum states for the (e) parity Λ-doubling components in the $(4p\pi)\,L^1\Pi, v=0$ state in $^{12}C^{16}O$, as obtained from line-broadening measurements in the spectrum of Figure 16. [Reproduced from Eikema, K.S.E., Hogervorst, W., and Ubachs, W. (1994a) Predissociation rates in carbon-monoxide—dependence on rotational state, parity and isotope. *Chemical Physics*, **181**(1–2), 217–245. © 1994, with permission from Elsevier.]

The combined efforts in XUV spectroscopy, classical and laser, have led to a deepened, but still partial, understanding of the level structure of the excited states of CO and its predissociation dynamics. The paper by Huber *et al*. (Eidelsberg *et al*. 2004) gives the most recent status on the perturbative interactions between the Rydberg states and the two major valence states $C'\,^1\Sigma^+$ and $D'\,^1\Sigma^+$ states causing the perturbations.

While the dominant predissociation mechanism giving rise to most of the line broadening and the rapid decay dynamics in the singlet excited states in CO is caused by the C′ and D′ states of $^1\Sigma^+$ symmetry, additional effects are caused by interactions with triplet states, which in many cases give rise to *accidental* predissociations. A long-known and celebrated example is that of the $E^1\Pi$ state (Simmons and Tilford 1974), which was independently studied for a number of isotopes by Baker *et al*. (1993) and Cacciani *et al*. (1995). For the $E\,^1\Pi, v=0$ level, the accidental predissociation occurs at a high rotational level ($J=31$), where a crossing with rotational levels belonging to the $k^3\Pi, v=3$ manifold occurs. In addition, $k^3\Pi, v=4$ was found to cross (the $E\,^1\Pi, v=0$ rotational manifold) both at $J=41$ and $J=44$; this is made possible by the mixing of two different spin–orbit levels in $k^3\Pi$.

The $E^1\Pi, v=1$ level is perturbed at low J-levels, even to the extent that a transition to the $k^3\Pi_0, v=6, J=7$ (e)-parity level could directly be observed in VUV-laser excitation (Ubachs *et al*. 2000a). This phenomenon of accidental predissociation in the $E^1\Pi, v=1$ level was later investigated with a narrowband (PDA-based) VUV-laser, therewith unraveling the Q-branches in the E-X (1,0) band. In the Q-branches, the $k^3\Pi, v=6$ perturber states give rise to shifts and broadening at the same time. The line shifts are such that the ordering of lines becomes fully erratic and of each in the six isotopomers of CO investigated ($^{12}C^{16}O$, $^{12}C^{17}O$, $^{12}C^{18}O$, $^{13}C^{16}O$, $^{13}C^{17}O$, and $^{13}C^{18}O$) the ordering is different. As an example, the Q-branch of the $^{13}C^{16}O$ isotopomer is presented in Figure 18, displaying the phenomenon in extremum.

Another illustrative example is that of the predissociation effect in the $(4d\sigma)\,^1\Sigma^+$—$X^1\Sigma^+$ (0,0) band in CO, displayed in Figure 19. Although the spectrum should reflect a simply structured $^1\Sigma^+ - ^1\Sigma^+$ system with a P and an R branch exhibiting a band gap, a seemingly erratic spectrum appears with an anomalous intensity distribution and strongly varying linewidths over the band profile. Perturbations clearly occur at $J=9, 13$, and 22, where

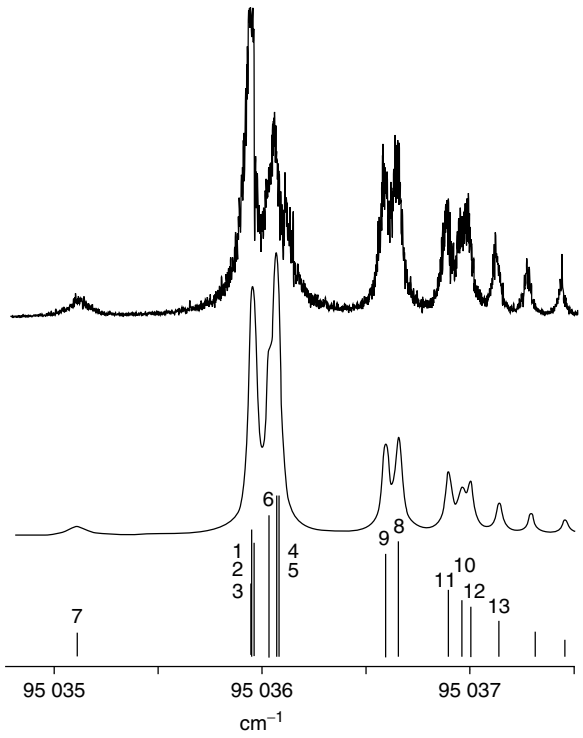

Figure 18 Example of the perturbing effect of the $k^3\Pi$, $v = 6$ state in CO, shifting and broadening all the Q-branch lines in the E-X (1,0) band. For the $^{13}C^{16}O$ isotopomer, the effect is found to be most drastic. The Q(7) is broadened and shifted to lower energy, while the Q(8) line is shifted to higher energy. In the upper graph, the experimentally recorded spectrum is shown, with the calculated spectrum below it. The sticks represent the line positions and calculated intensities in a perturbation model. [Reproduced from Ubachs *et al*. (2000a).]

lines are missing. The rotational structure of the $(4d\sigma)$ $^1\Sigma^+$, $v = 0$ state can be deduced by comparing combination differences in the P and R branches, resulting in an unambiguous assignment. The line positions can be fitted to a simple rotational progression, while leaving out the most heavily perturbed lines in a fitting routine. On the basis of the resulting rotational constants, the deviations of the perturbed lines can be plotted, as shown in Figure 20. This demonstrates how an interacting triplet state of yet unknown origin causes predissociation as well as perturbing shifts in the rotational structure of a vibrational band. Note how the rates of predissociation and the perturbing shifts are associated. The line intensities provide additional information, in that they exhibit a strongly non-Boltzmann behavior. It is a remarkable effect that the P(22) and R(20) lines, exciting the $J = 21$ level, are exceptionally strong, while they are located next to a strongly predissociated $J = 22$ level, to be probed in P(23) and R(21) lines, which have lost all intensity in the spectrum.

As is exemplified in the above, the level structure of carbon monoxide and its isotopomers provides a test ground for the study of perturbations and predissociation mechanisms. The use of narrowband XUV lasers has aided in unraveling the phenomena.

3.4 Rydberg-valence Interaction in Molecular Nitrogen

The N_2 molecule is isoelectronic with the CO molecule and the two molecules have some features in common. The triple-(2p) bond also causes a large dissociation energy ($78\,714\,cm^{-1}$) and the electronically excited states exhibit strong perturbations and predissociation phenomena. The inversion symmetry in N_2, however, separates the electronic states into two distinct classes: those of *ungerade* symmetry, accessible via dipole-allowed transitions from the ground state and those of *gerade* symmetry. Apart from the remark that some *gerade* excited states have been investigated by 1XUV + 1VIS two-photon double resonance spectroscopy (de Lange *et al*. 2002), we focus on the states of *ungerade* symmetry, which are directly accessible via XUV excitation.

Although the excited states of N_2 are separated in u and g symmetries, the dipole-allowed XUV absorption spectrum remains one of the severe complexity (Vieitez *et al*. 2008). Strong interactions between singlet states of valence character (the $b^1\Pi_u$ and the $b'\ ^1\Sigma_u^+$ states) and Rydberg states (the $c_n\ ^1\Pi_u$ and the $c'_{n+1}\ ^1\Sigma_u^+$ series converging to the $X^2\Sigma_g^+$ state of the ion) dominate the absorption spectrum. The potential energy curves (in a diabatic picture) are shown in Figure 21, including the $o_n\ ^1\Pi_u$ Rydberg series converging to the $A\ ^2\Pi_u$ state of the ion. The Rydberg-valence interactions are so strong that the vibrational bands in the valence and Rydberg manifolds were assigned as differing electronic states, but through the work of Dressler and coworkers (Stahel *et al*. 1983) the perturbations were fully unraveled and the anomalous non-Franck–Condon intensity distributions explained. In N_2, the dominant predissociation mechanism is that of spin–orbit coupling to states of triplet symmetry, in particular, the combined $C\ ^3\Pi_u$ and $C'\ ^3\Pi_u$ states, the potential energy curves of which are presented in Figure 21.

As an example of the strong variations in predissociation behavior of the excited states, we present measurements of the $b^1\Pi_u$—$X^1\Sigma_g^+$ (1,0) band. In the main isotopomer $^{14}N_2$, the $b^1\Pi_u$, $v = 1$ state is, along with the lowest vibrational level of the $c'_4\ ^1\Sigma_u^+$ Rydberg state, the only state that is unpredissociated. However, the slight change in energy when going to the $^{15}N_2$ isotopomer causes the $b^1\Pi_u$, $v = 1$ state to become strongly predissociated. The spectra for both isotopes are compared in Figure 22.

In the past decade, much progress has been made using not only high-resolution XUV spectroscopic methods,

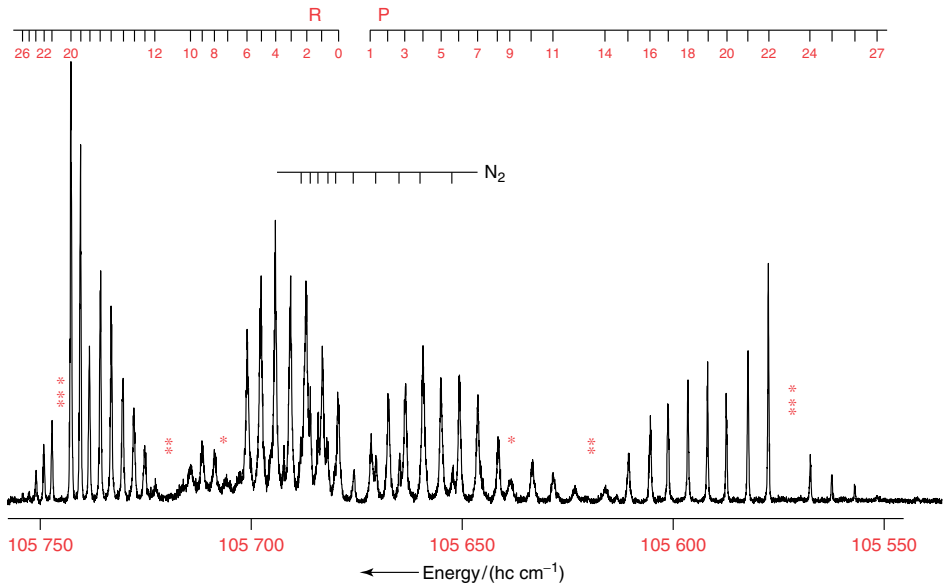

Figure 19 Spectrum of the $(4d\sigma)\ ^1\Sigma^+$—$X^1\Sigma^+$ (0,0) band in CO. The three locations of the interaction with a triplet perturber state are indicated by (*). Some lines pertaining to the N_2 molecule, one just falling in the band gap, are indicated as well. [Reproduced from Eikema, K.S.E., Hogervorst, W., and Ubachs, W. (1994a) Predissociation rates in carbon-monoxide—dependence on rotational state, parity and isotope. *Chemical Physics*, **181**(1–2), 217–245. © 1994, with permission from Elsevier.]

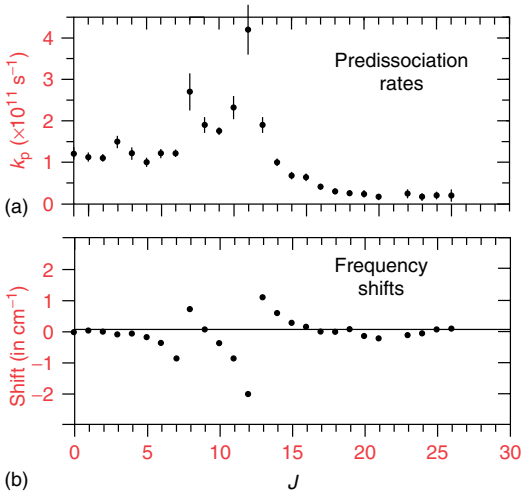

Figure 20 (a) Predissociation rates for rotational levels in the $(4d\sigma)\ ^1\Sigma^+$, $v = 0$ state as obtained from line broadening in the spectrum displayed in Figure 19. (b) Frequency shifts from a simple rotational progression induced by a perturbing triplet state in CO. Note that resonances in the predissociation rates are accompanied by large frequency shifts, as characteristic of an accidental predissociation by a triplet state. [Reproduced from Eikema, K.S.E., Hogervorst, W., and Ubachs, W. (1994a) Predissociation rates in carbon-monoxide—dependence on rotational state, parity and isotope. *Chemical Physics*, **181**(1–2), 217–245. © 1994, with permission from Elsevier.]

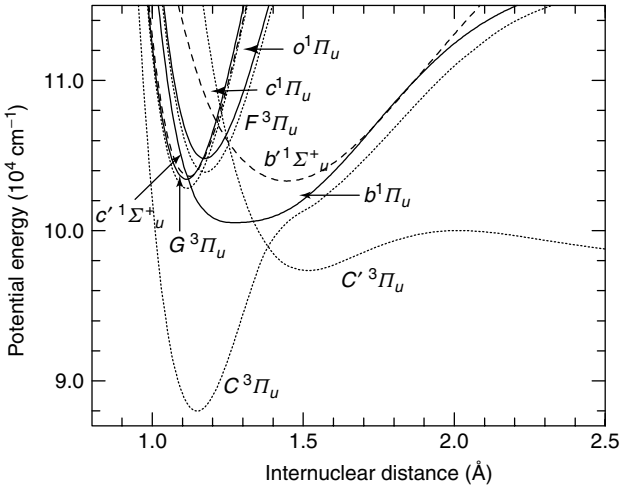

Figure 21 Potential energy diagram for the relevant excited states of the *ungerade* symmetry of nitrogen molecule. [Reproduced from Lewis *et al.* (2005).]

mainly narrowband lasers (Sprengers *et al.* 2005b, Ubachs *et al.* 1989, Ubachs 1997, Ubachs *et al.* 2000b), but also synchrotron radiation studies (Stark *et al.* 2005) to chart many details of the rotational structure in the heavily perturbed vibrational bands. At the same time, a model based on coupled Schrödinger equations has been developed that can explain the anomalous intensity distributions, the varying predissocation rates, and the strong isotopic effects (Lewis *et al.* 2005). This sophisticated model is able to explain all observed details up to an excitation energy of some 105 000 cm^{-1}. Now, work is in progress to include the predissociation phenomena at slightly higher energies; there is a crucial issue—it is not just the $C\ ^3\Pi_u$ and $C'\ ^3\Pi_u$ states

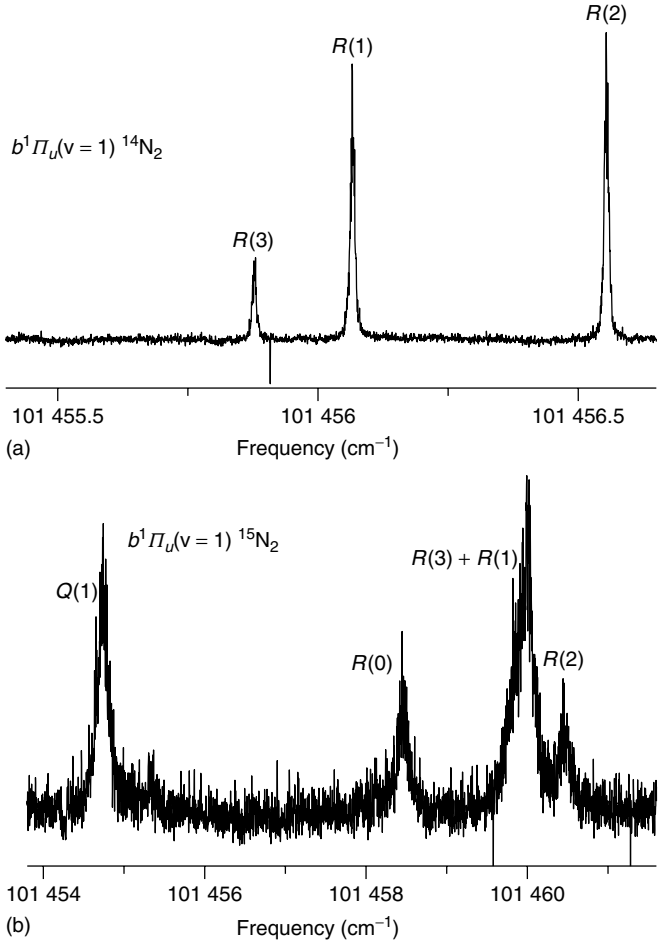

Figure 22 Excitation spectrum of the $b^1\Pi_u, v = 1$ state for (a) the $^{14}N_2$ and (b) the $^{15}N_2$ isotopomer. [Reproduced from Sprengers *et al*. (2005b).]

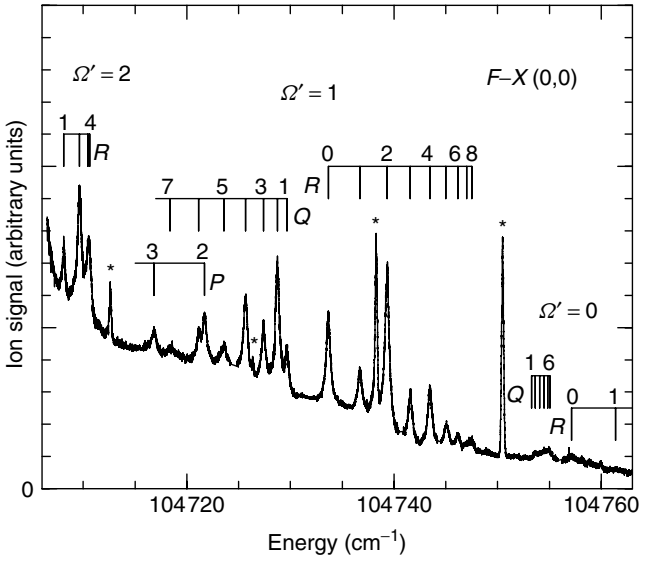

Figure 23 Observed excitation spectrum of the $F^3\Pi_u, v = 0$ state in $^{14}N_2$. [Reproduced from Sprengers *et al*. (2005a).]

but also higher lying states of triplet character, such as the $F\ ^3\Pi_u$ and $G^3\Pi_u$ states, that must be included. A helpful ingredient is that $F\ ^3\Pi_u, v = 0$ has been observed directly by 1XUV + 1UV laser excitation under high resolution. A spectrum, displayed in Figure 23, shows the narrow spectral signatures of all three spin–orbit components. Although the excited states in this $F\ ^3\Pi_u, v = 0$ triplet manifold are narrow, the location of the F-state has its consequences for a comprehensive perturbation model for N_2.

3.5 Precision Studies of the H_2 Lyman and Werner Bands

The hydrogen molecule and its isotopomers are the system with a prominent VUV-XUV spectrum, which had been investigated over decades using classical techniques. Lyman was the first to detect the VUV emission in the $B^1\Sigma_u^+ - X^1\Sigma_g^+$ system, which is known as the *Lyman system* (Lyman 1906). Later Werner observed the $C^1\Pi_u - X^1\Sigma_g^+$ system, which was then named after him (Werner 1926). The absorption spectrum of the H_2 molecule does not exhibit the characteristic feature of a molecular spectrum with lines ordered in bands. Because H_2 is so light, the vibrational and the rotational spacings become very large that the lines appear randomly distributed. Moreover, the nonadiabatic interactions become so strong that spectral lines undergo large shifts, whereas the intensities undergo interference effects such that Höhnl–London factors do not apply. Over the years, classical absorption and emission spectra were obtained at improved accuracies, ultimately ending with the Atlases of Lyman (Abgrall *et al*. 1993a) and Werner (Abgrall *et al*. 1993b) band lines by the Meudon group.

Laser-based XUV spectroscopy of the Lyman and Werner band lines was performed by Hinnen *et al*. (1994) for the H_2 and D_2 molecules and later for the HD isotopomer as well (Hinnen *et al*. 1995). In these studies, a crossed beam configuration was employed to reduce Doppler broadening, but the laser XUV bandwidth of $0.25\,cm^{-1}$ (PDL-based XUV source) was a limiting factor in the determination of line positions; the accuracy of $0.05\,cm^{-1}$ implies only a slight improvement over classical studies.

A step forward in high-accuracy spectroscopic studies resulted from the use of a PDA-based XUV source of $0.01\,cm^{-1}$ bandwidth. High-precision wavelength calibration studies were performed on the Lyman and Werner band systems of H_2 (Philip *et al*. 2004), HD (Ivanov *et al*. 2008), and D_2 (Roudjane *et al*. 2008). A typical spectrum, also displaying the on-line measured I_2 saturation spectrum, for calibration purposes is shown in Figure 24.

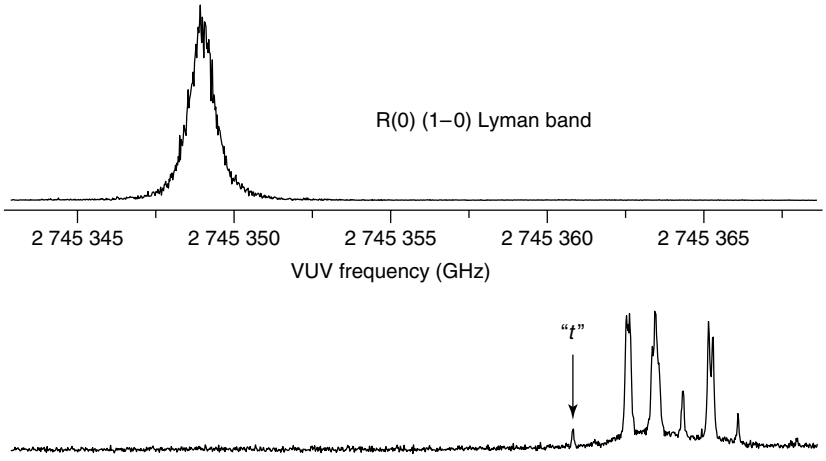

Figure 24 Spectrum of the R(0) rotational line in the B-X(1,0) Lyman band recorded with the narrowband PDA-based XUV laser system. [Reproduced from Hollenstein *et al*. (2006).]

The accuracy obtained in these XUV laser calibration studies has been pushed to the $\Delta\lambda/\lambda = 5 \times 10^{-8}$ level for the purpose of comparison with high-redshift spectroscopic data of the same lines, which have recently become available from large telescopes equipped with high-resolution spectrometers. A comparative analysis of laboratory (zero-redshift) data and high-red shift data allows for an investigation of a possible variation of the proton–electron mass ratio μ over cosmological time. In this respect, an indication for a relative change was detected at the level $\Delta\mu/\mu = (2.4 \pm 0.6) \times 10^{-5}$ (Reinhold *et al*. 2006).

3.6 Lyman-α Excitation of H

The previous sections discussed about pulsed VUV/XUV laser excitation. However, CW coherent spectroscopy has also been demonstrated at 121.56 nm, close to the boundary of the VUV and XUV spectral region. The laser source, on the basis of CW four-wave mixing in mercury, has been discussed in Section 2.9. It was developed with the aim of laser cooling and spectroscopy of anti-hydrogen. Anti-hydrogen could offer possibilities to test CPT symmetry and the Einstein equivalence principle, but is rather difficult to make and store (Gabrielse 2005). Spectroscopy on antihydrogen has, therefore, not been demonstrated yet. Instead, the Lyman-α source has been used to demonstrate excitation of the equivalent 1s–2p transition in normal atomic hydrogen (Eikema *et al*. 2001). The 1s–2p transition (Figure 25) was recorded with near-natural linewidth for the first time with this experiment, and it still presents the shortest wavelength for which CW laser excitation has been achieved.

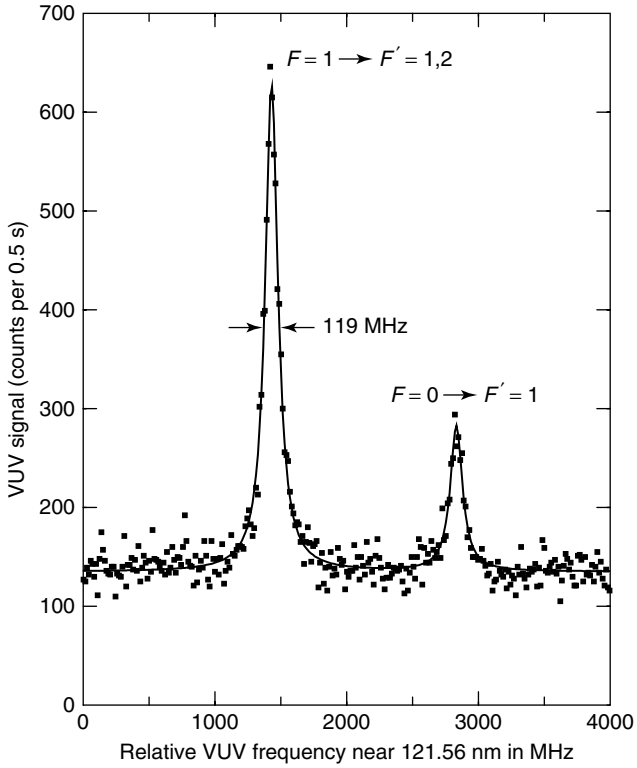

Figure 25 Recorded spectrum in the precision experiment on the 1s–2p Lyman-α resonance line in H at 121.56 nm, using continuous wave radiation produced by four-wave mixing in Hg vapor. [Adapted from Eikema *et al*. (2001).]

4 THE INTERMEDIATE REGIME: PICOSECOND LASER PULSES

So far in this article, applications of harmonic generation are discussed using lasers with pulse durations of typically 5 ns, as obtained from powerful Q-switched lasers. The

strategy followed is to produce wavelength-tunable-pulsed radiation by pumping dye lasers or titanium–sapphire lasers. Those pulses are then converted, via frequency-doubling in nonlinear crystals (KDP or BBO), to the ultraviolet regime. In a subsequent step, XUV radiation is produced by frequency-tripling in gas (most often a gas jet). This is done with laser pulses of up to 20 mJ per pulse in the UV; for durations of 5 ns and focusing tightly to a 20 μm spot size yields power densities below $10^{12}\,\mathrm{W\,cm^{-2}}$. This is in the perturbative regime, i.e., power densities below those implied in equation (19), and only the term represented by $\chi^{(3)}$ in equation (1) is effective. In an exceptional case, over 50 mJ per pulse was produced in the UV permitting fifth harmonic generation to produce XUV radiation with a wavelength as short as 58 nm, although at low intensities of some 10^4 photons per pulse (Eikema *et al*. 1997).

For laser pulses of femtosecond duration, it is rather easy to reach the plateau region for which power densities on the order of $10^{13}\,\mathrm{W\,cm^{-2}}$ are required (Section 5). Even for laser pulses in the picosecond regime, the plateau is easily reached, as was proven in the earliest studies of high-harmonic generation (Ferray *et al*. 1988). However, the latter studies were performed with the nontunable output of mode-locked lasers and they lacked the possibility of performing XUV excitation spectroscopy, which relies on the option of tunability. At Lund a laser source was constructed based on a distributed feed-back dye laser (DFDL), pumped by a mode-locked laser, exhibiting tunability over the gain curve of infrared dyes at pulse durations of 50 ps. The output of this DFDL was used to produce wavelength tunable XUV radiation down to 35 nm (Lynga *et al*. 2001), which was used for XUV excitation studies of atoms and molecules (Cacciani *et al*. 1998), however, at bandwidths of some $30\,\mathrm{cm^{-1}}$, which is not competitive with most classical sources from the perspective of spectroscopic resolution.

An alternative picosecond tunable XUV source was built, based on the combination of a number of optical techniques. The output of a single-mode tunable Ti : sapphire laser was pulse amplified in a traveling-wave amplifier configuration using infrared dyes. The pump laser was a frequency-doubled Q-switched Nd : YAG laser (532 nm) that was pulse compressed via *stimulated Brillouin scattering* (*SBS*) to 300 ps pulse durations at conversion efficiencies exceeding 90% (Schiemann *et al*. 1997, Neshev *et al*. 1999). Hence, wavelength tunable pulses of 300 ps duration and pulse energies of typically 1 mJ per pulse were produced, which were further amplified in a preamplifier and a bow-tie multipass amplifier to 225 mJ (Brandi *et al*. 2003b). By focusing these pulses, power densities of $5 \times 10^{13}\,\mathrm{W\,cm^{-2}}$ were achieved, allowing for HHG in gas jets of noble gases and molecular gases (Brandi *et al*. 2003a).

In the setup, displayed in Figure 26, harmonics up to 21st were obtained in Ar at wavelengths below 40 nm. Efficiency curves are presented in Figure 27. A resolving power of $\lambda/\Delta\lambda = 2.5 \times 10^5$ or a bandwidth below $1\,\mathrm{cm^{-1}}$ was obtained at these short wavelengths. This compares to the best wavelength resolution that can be obtained in classical spectrograph-based XUV studies. Application in a spectroscopy experiment was demonstrated by measuring the $(1s^2) \rightarrow (1s)(4p)$ transition in He at 52.2 nm (Brandi *et al*. 2003a).

The high energies in combination with the duration of the laser pulses cause the nonlinear medium to become fully ionized. Experimentally, it was verified that the optimum harmonic yields were achieved at intensities of $3 \times 10^{13}\,\mathrm{W\,cm^{-2}}$ and that further increase in intensity did not result in increased XUV production (Brandi *et al*. 2006). The ionization of the medium causes rapid phase changes via equation (15) by the production of electrons that affect the index of refraction as

$$n_e(t) = 1 - \frac{e^2 N_e(t)}{8\pi^2 m_e \epsilon_0 \nu^2} \tag{25}$$

Hence, the release of electrons first causes a blue shift, via equation (16), but the electrons leave the interaction region rapidly. The resulting plasma dynamics in the interaction zone gives rise not only to blue shifts but also, under certain conditions, to red shifts. These phenomena can be investigated for harmonic conversion processes, whereby reasonably narrowband XUV is produced that can be scanned over an atomic resonance for accurate wavelength calibration; this facilitates the investigation of the plasma dynamics and the related frequency chirp phenomena (Brandi *et al*. 2006).

5 FREQUENCY COMB LASER TECHNIQUES FOR XUV SPECTROSCOPY

Experiments in the VUV and XUV frequently rely on harmonic generation of lasers and base the calibration on the measurement of the fundamental laser frequency. Traditional methods for this include the use of absorption spectroscopy of previously calibrated transitions in, e.g., molecular iodine. Reference lines of this kind are not available everywhere, and often an etalon is used to bridge the frequency distance to such reference lines. The accuracy that can be achieved for the fundamental frequency is typically on the order of 1 MHz in the visible and infrared part of the spectrum. However, as discussed in Section 2.6, amplification and harmonic upconversion can disturb the direct relationship (via the harmonic order)

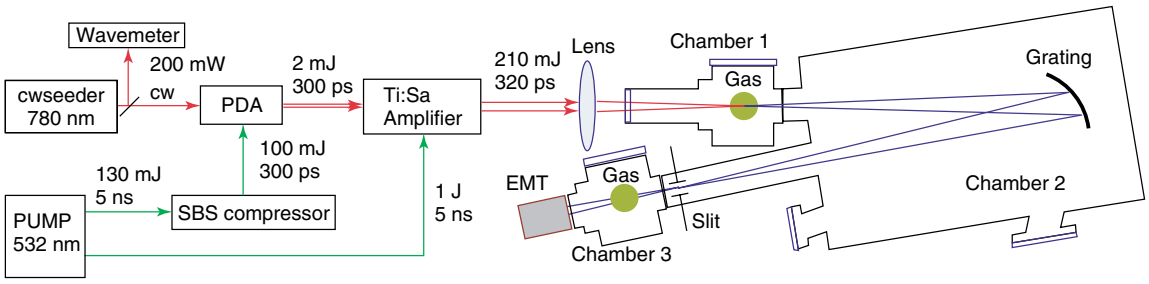

Figure 26 Experimental layout for the production of powerful laser pulses of 300 ps duration at intensities of >200 mJ per pulse, at tunable wavelengths in the range 760–800 nm. CW radiation from a Ti : Sa laser is pulse amplified in infrared dyes in a multistage traveling-wave amplifier, pumped by pulses at 532 nm and 300 ps duration obtained from an SBS compressor. These pulses are thereupon amplified in Ti : Sa, first in a preamplifier, then in a bow-tie multipass postamplifier to reach power levels of >200 mJ. These pulses are focused at the orifice of a pulsed valve with $f = 20$ cm, reaching power densities of $>10^{13}$ W cm^2, sufficient to generate harmonics on the plateau. An XUV grating spectrometer is used to disperse the high-order harmonics and detect them on an electron multiplier. [Reproduced from Brandi *et al.* (2003a).]

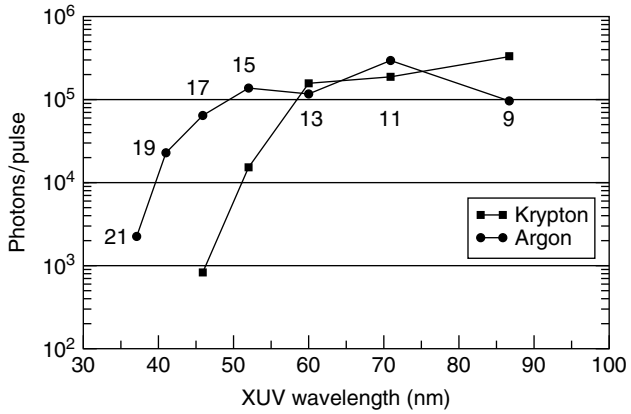

Figure 27 Harmonic conversion efficiency in the XUV domain for input pulses at 225 mJ per pulse at $\lambda = 780$ nm and 300 ps duration, focused with a $f = 20$ cm lens. The plateau structure with the characteristic cutoff is clearly visible, which occurs first for Kr at the 13th harmonic, because of its lower ionization potential. [Adapted from Brandi *et al.* (2003a).]

between the calibration of the fundamental light and the harmonics. Time-dependent phase distortions can result in instantaneous frequency excursions from the calibrated original frequency (Wieman and Hänsch 1980, Fee *et al.* 1992, Melikechi *et al.* 1994, Eikema *et al.* 1997, Reinhard *et al.* 1996). It becomes even more complicated if the signal is produced only by a part of the laser pulse.

Such chirp-induced errors can be particularly problematic for experiments, requiring the highest level of accuracy in the XUV. An example was given in Section 3.2, with the excitation of helium from the ground state using 58.4 nm light to test QED. The accuracy in the theoretical ground-state energy position is currently 36 MHz according to Drake and Yan (2008). The experimental accuracy is on the order of 1 part in 10^8 (50 MHz) (Eikema *et al.* 1997, Bergeson *et al.* 1998), for a large part due to chirp effects. It is rather difficult to improve on this with nanosecond laser pulses.

5.1 QED Tests in the XUV with Atoms

The reason to probe transitions at XUV wavelengths in atoms is given by the way QED effects scale with the number of protons (Z) in the nucleus. For one- and two-electron systems, this scaling is $\approx Z^4$ for the lowest order QED effects (Drake and Yan 2008, Adkins *et al.* 2007) and even larger for higher order terms. Therefore, quite a number of spectroscopic experiments have been performed on heavy (high Z) ions such as U^{92+} (Stoehlker *et al.* 2008, Gumberidze *et al.* 2005) or Fe^{25+} (Chantler *et al.* 2007). The QED effects are largest in the ground state, but for heavy ions this means that transitions involving the ground state are in the X-ray region. Unfortunately, no narrow bandwidth laser exists for such short wavelengths. In the low-Z limit, one of the best known tests of QED involves measuring the 1S–2S transition at 2×243 nm in atomic hydrogen, where an accuracy on the order of $1 : 10^{14}$ (Fischer *et al.* 2004) has been achieved. At 243 nm, precision laser sources are available, but progress in hydrogen is now hampered by the uncertainty of the charge radius of the proton. A measurement of transitions in helium- and hydrogen-like helium$^+$ ions would by-pass this obstacle, because the QED effects are at least 16 times larger in these atoms according to the $\approx Z^4$ scaling law. Helium also has the advantage that the ^{4}He isotope has no nuclear spin, in contrast to hydrogen. However, excitation of helium requires ≈ 50 nm for a single-photon transition and 120 nm for a two-photon transition from the ground state (where the QED effects are the largest). Likewise, He^+ requires ≈ 25 nm for a single-photon transition and 61 nm for the 1S–2S transition. Measurements on He^+

have the advantage that not only the theory is very well developed but also for neutral helium considerable progress has been made over the past 10 years (Drake and Yan 2008, Adkins *et al.* 2007, Pachucki 2006, 2007, Karshenboim 2005). To become competitive with hydrogen in the experiment–theory comparison, the accuracy in XUV spectroscopy still has to be improved by orders of magnitude. A possible route to this goal is the use of the so-called frequency comb lasers.

5.2 Frequency Comb Lasers

The invention of the self-referenced frequency comb laser (Holzwarth *et al.* 2000, Jones *et al.* 2000, Udem *et al.* 2002) has caused a revolution in precision frequency metrology and attosecond laser science (Corkum and Krausz 2007, Baltuska *et al.* 2003, Gallmann and Keller 2011). Indeed, the high precision obtained in, e.g., the aforementioned 1S–2S hydrogen experiment is partly due to the use of a frequency comb. These devices are based on a mode-locked (ultrafast) laser, emitting pulses that have a precisely controlled timing and phase. This control results in a mode spectrum that is completely determined by just two numbers: the repetition rate of the pulses f_{rep} and an offset frequency f_0 (also frequently represented as f_{ceo}, where ceo stands for carrier–envelope offset). Both are in the radio-frequency domain and can be counted with high precision. A frequency comb, therefore, forms a bridge between optical frequencies in the hundreds of terahertzes range (which cannot be counted directly) and radio frequencies that can be easily counted. This concept of the frequency comb laser is illustrated in Figure 28.

A comparison is shown of the output of a comb laser in the time and frequency domain. In the time domain, an infinite train of pulses is observed with a repetition time T. On close inspection, one can see that the phase of the pulses is normally not constant from pulse to pulse, but that it contains a carrier–envelope phase slip $\Delta\phi_{\mathrm{ce}}$. This originates from the difference in phase and group velocity in the comb laser resonator. The output viewed in the frequency domain (e.g. with a spectrometer with very high resolution) consists of many modes, which are the cavity modes of the laser. However, because of the Fourier relation between time and frequency domain, the mode spacing is equal to the repetition rate in the time domain ($f_{\mathrm{rep}} = 1/T$). Likewise, the carrier–envelope phase shift $\Delta\phi_{\mathrm{CE}}$ of the pulses corresponds to an offset frequency of the "comblike" spectrum according to $\Delta\phi_{\mathrm{ce}} = 2\pi f_0/f_{\mathrm{rep}}$, which can be measured using an "f : 2f" interferometer (Holzwarth *et al.* 2000, Jones *et al.* 2000). For each mode frequency, one can write

$$f_n = f_0 + n f_{\mathrm{rep}} \tag{26}$$

If both f_{rep} and f_0 are locked to an atomic clock reference, then all comb modes are known in principle to the same high precision. Such an optical frequency "ruler" can be used for calibration purposes by counting an interference beat note between a CW narrow bandwidth laser (used for excitation of the transition under scrutiny) and the comb laser modes. One has to know beforehand with which mode n the (electronically selected) beat note is generated. This can normally be determined from a previous (less accurate) calibration or by changing the repetition rate of the comb laser. The spectral coverage of comb lasers is typically in the (near) infrared, as the most common comb lasers are based on Ti : sapphire or Er-fiber mode-locked lasers. Spectral coverage can be extended via nonlinear interaction in crystals and photonic fibers (Dudley *et al.* 2006).

Precision spectroscopy of Lamb shifts in helium and hydrogen-like helium$^+$ could ideally be pursued by narrowband pulsed laser sources or even by CW sources at the desired wavelengths (Eikema *et al.* 1999, 2001), but these possibilities are limited or non-existent. Frequency comb lasers can possibly solve these issues in two ways.

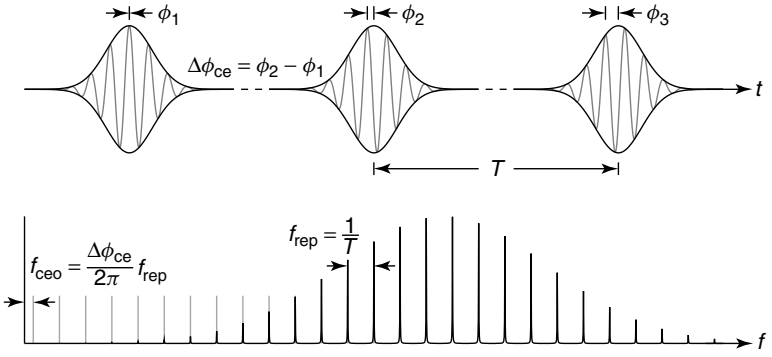

Figure 28 The frequency comb laser principle based on a mode-locked laser. Upper half: time-domain representation as phase-coherent laser pulses. Lower half: frequency domain representation in the form of resonator modes, parameterized with f_{rep} (repetition frequency) and f_{o} (the carrier–envelope offset frequency, represented here as f_{ceo}). [Reproduced from Zinkstok (2008).]

First, the high peak power of comb laser pulses can be exploited to generate high harmonics of the original comb light. With enough peak power in the comb laser pulses (either by amplification (Witte *et al.* 2005, Zinkstok *et al.* 2006) or by enhancement in an optical resonator (Jones *et al.* 2005, Gohle *et al.* 2005), it is possible to generate light with wavelengths well into the XUV. Second, instead of using a CW laser for inducing an atomic transition and then using a frequency comb for its calibration, the upconverted pulses from the comb laser itself can be used directly for this purpose (direct frequency comb spectroscopy, DFCS). The principle of excitation with phase-coherent pulses (Baklanov and Chebotaev 1977) is very similar to Ramsey spectroscopy with spatially separated fields (Ramsey 1949). Experimentally, it was already explored in the late 1970s (Teets *et al.* 1977, Eckstein *et al.* 1978) by exciting atomic sodium using dye laser pulses in a resonator. Similar experiments were performed with two delayed pulses in sodium, demonstrating Ramsey-type interference (Salour and Cohen-Tannoudji 1977). There were no developments until 1996 when a mode-locked laser was used to determine hyperfine splittings in rubidium (Snadden *et al.* 1996) and in 1997 a similar experiment in cesium was carried out (Bellini *et al.* 1997). Because f_0 control was still not possible at that time, only relative measurements could be performed. With the invention of the frequency comb laser, the situation has changed, making DFCS a very interesting new tool for spectroscopy (Marian *et al.* 2004, Witte *et al.* 2005, Zinkstok *et al.* 2006).

5.3 Upconversion of Frequency Comb Lasers

Converting frequency combs to VUV and XUV wavelengths is not trivial because HHG is needed to produce VUV and XUV from comb pulses at (near) infrared wavelengths. This process requires a peak intensity on the order of 10^{13}–10^{14} W cm^{-2}, except if plasmon field enhancement is used, as demonstrated recently by Kim *et al.* (2008). Typical comb lasers emit pulses in the range of 10–100 fs, with peak powers in the range of 0.1–1 MW. Without any enhancement, even strong focusing is insufficient to reach the required power density for HHG. As already mentioned, one possibility is to enhance the intensity by storing the pulses in an enhancement cavity, similar to resonators used for enhancing CW laser light. One complication with ultrashort pulses is their bandwidth. To enhance the full spectrum, one needs to fulfill the resonance conditions for all the frequencies in the pulses. This can be achieved with special "chirped" mirrors, to compensate for wavelength-dependent phase velocities. If the cavity contains strongly focusing mirrors, then sufficient peak power density can be generated in a noble gas jet (inside the cavity) for efficient HHG. In this manner, light has been generated initially by two groups, down to a wavelength of 60 nm (Jones *et al.* 2005, Gohle *et al.* 2005). An example of the setup to generate intracavity HHG is shown in Figure 29.

In Figure 30, the corresponding harmonic yield for this setup is shown. Harmonics up to the 15th order are clearly visible.

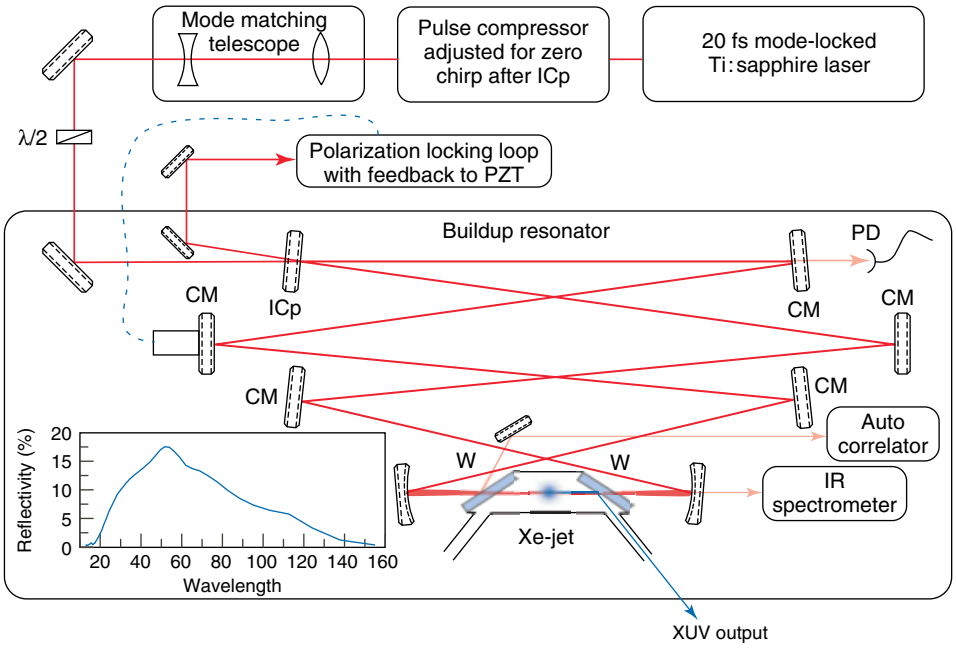

Figure 29 Experimental setup for generating XUV via HHG from frequency comb laser pulses that are enhanced in a resonator. [Reproduced from Gohle *et al.* (2005).]

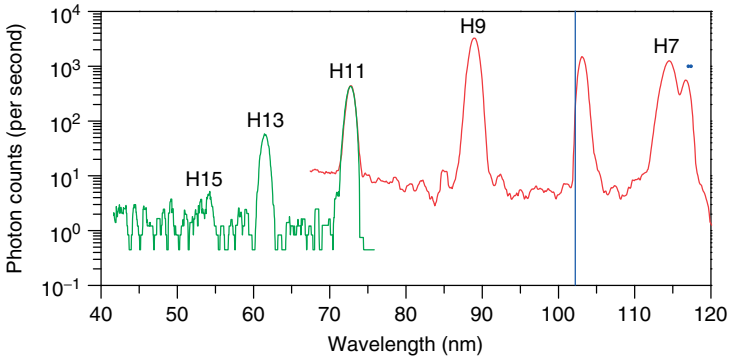

Figure 30 The high-harmonic yield in an enhancement resonator for frequency comb pulses, showing light up to the 15th harmonic. [Reproduced from Gohle *et al.* (2005).]

Harmonics into the XUV can, therefore, be generated with frequency comb lasers, but the generated light is not necessarily a frequency comb too. For this, a high phase stability between the upconverted pulses is required. The phase of the harmonics generated in a HHG process depends via the vector potential on the intensity of the driving radiation. This can be calculated via the so-called quasi-classical action S acquired by the electron in the three-step harmonic generation process, as explained in Section 2.10. According to Lewenstein *et al.* (1995), Kan *et al.* (1995), and Lindner *et al.* (2003), the action is equal to

$$S(p, t_0, t_1) = \int_{t_0}^{t_1} (I_\mathrm{p} + p^2(t)/2m_\mathrm{e})\mathrm{d}t \qquad (27)$$

where I_p is the ionization potential of the medium (atom), t_0 is the time (moment) of tunneling, t_1 is the recombination time, p is the momentum of the electron, and m_e is the electron mass. The phase of the emitted harmonics then depends on two components:

$$\phi = -S(p, t_0, t_1)/\hbar + q\omega t_1 \qquad (28)$$

where q is the harmonic order and ω is the central angular frequency of the laser. The first part (containing S) is directly intensity dependent, as the momentum p depends on the electric field of the laser and the moment of tunneling and recombination. The action S also depends on the kind of trajectory the electron wavepacket takes. Two of those paths, generally referred to as the *short and long trajectory*, contribute the most to the HHG signal. For large fields, the atomic phase (and therefore the generated harmonics) depends nearly linearly on intensity and, therefore, also on the pondoromotive energy via

$$\theta = -\eta U_\mathrm{p} \qquad (29)$$

Lindner *et al.* (2003) have given an example for 25th harmonic generation in argon, where the calculated values are $\theta = -0.11U_\mathrm{p}$ rad eV^{-1} for the short quantum path and $\theta = -3.9U_\mathrm{p}$ rad eV^{-1} for the long path. For typical HHG conditions, this can lead to a phase variation, ranging from a few radians for the short path to tens of radians for the long path. Both contributions are also separated in space, as the short quantum path is emitted mostly on the axis and the long path contribution is more concentrated at larger beam divergences. In combination with the geometrical Gouy phase over a focus, one can favor the short quantum path contribution by focusing the laser slightly in front of the interaction medium (Gaarde *et al.* 1999, Lindner *et al.* 2003). This is clearly desirable for upconversion of frequency comb lasers, because the short quantum path contribution is far less susceptible to intensity variations. Therefore, a higher degree of phase coherence is expected in this case. Experimentally, this has been verified for individual harmonics (Zerne *et al.* 1997) by inducing spatial interference between two HHG beams, as shown in Figure 31. For this demonstration, 35 ps pulses from a normal mode-locked 1064 nm laser (not a frequency comb) were split in two and individually focused side by side to $\approx 10^{13}$ W cm^{-2} in a gas jet. After separation of the fundamental and harmonic light, stable spatial interference fringes were observed in the far field at the 13th harmonic. Care was taken in this case to have equal fundamental intensities in the two foci. Fluctuations in the original 1064 nm beam then lead to equal phase shifts in the two HHG processes, so that a maximum visibility of the fringes is retained. With uneven pulse intensities between the two HHG sources, a rapid degradation of contrast was observed.

Experiments have also been performed with time-delayed ($\approx$100 fs) XUV pulses made by HHG (Cavalieri *et al.* 2002, Pirri *et al.* 2008), leading to interference effects in the excitation probability of krypton. Therefore, phase coherence is probably also maintained to a large degree for high harmonics generated in an enhancement cavity. If so, then every harmonic forms a new frequency comb on its own, as depicted in Figure 32. However, this has been

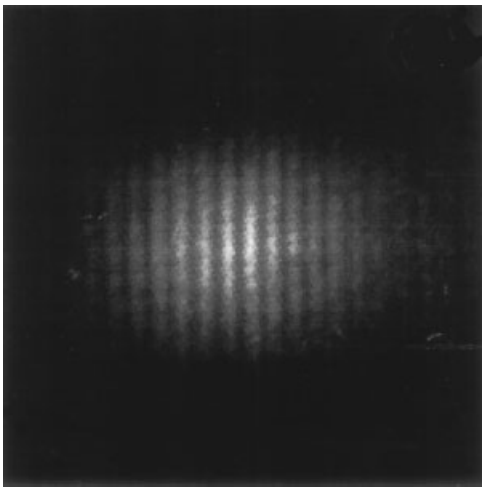

Figure 31 Spatial interference pattern between two XUV beams at 82 nm, produced by 13th harmonic generation of 1064 nm light. [Reproduced from Zerne *et al*. (1997).]

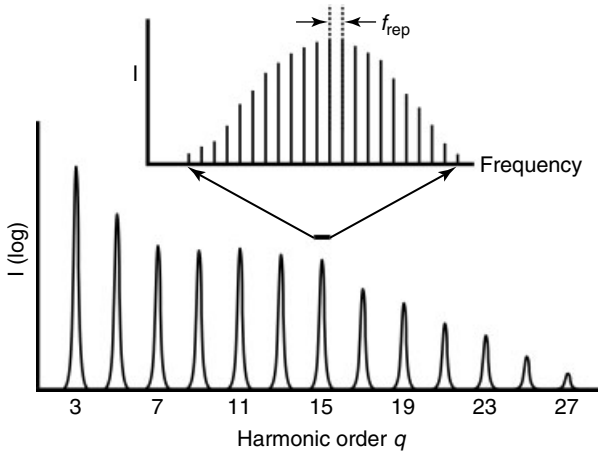

Figure 32 Schematic representation of frequency spectrum generated by high-harmonic generation at the full repetition rate of the comb laser. Each harmonic will consist of a frequency comb with a spacing equal to the repetition rate f_{rep}.

verified experimentally so far only at the third harmonic near 266 nm (Jones *et al*. 2005, Gohle *et al*. 2005) and not at shorter wavelengths.

Given the properties, discussed above, of comb lasers and HHG, upconversion of frequency comb light at full repetition rate has clearly two major advantages. First, the comb mode spacing remains equal to the original comb (because the repetition rate remains equal). Second, the harmonic generation process is performed in quasi-steady state. Each pulse experiences the same conditions in the HHG process. Phase shifts in the upconverted pulses due to HHG and competing ionization processes are basically identical for each pulse. This means that the comb modes are expected to be narrow and not shifted from their original positions (apart from the multiplication factor of the harmonic).

Compared to the first experiments with enhancement cavities, considerable progress has been made by using higher power comb lasers based on Yb-fiber technology (Hartl *et al*. 2007). Alternatively, a low-repetition rate (10.8 MHz), but high power per pulse Ti : sapphire oscillator, has been employed, leading to harmonics at the microwatts power level with a wavelength down to 43 nm (Ozawa *et al*. 2008). Up to now, no spectroscopic experiment has been demonstrated with these sources in the VUV or XUV. Despite the relatively high average power used now, it most likely requires interaction with many pulses to obtain a sizeable excitation probability. In practice, this means that confinement in traps would be beneficial, e.g., by storing He^+ ions in a Paul trap to probe the 1S–2S transition. One issue of the cavity enhancement approach is the difficulty of coupling out the generated XUV power with high efficiency from the cavity. Another is the relatively small flexibility in the choice of wavelengths (given by the peak wavelength of current comb laser implementations).

5.4 Two-pulse Frequency Comb Amplification and Excitation

Because of some of the drawbacks of cavity enhancement, a different approach has been pursued to perform DFCS in the XUV based on *amplification of comb pulses*. Ideally, one would like to amplify all the comb pulses at high (full) repetition rate to keep the mode spacing of the amplified comb large enough. In practice, a rate of 100 MHz is desirable, but this has not been demonstrated yet. Rapid progress in the field of high-power Yb-fiber amplifiers has made 100 μJ possible at intermediate repetition rates (few MHz Limpert *et al*. 2009). This still leads to rather narrowly spaced modes.

A solution was demonstrated, making use of the amplification of only a few subsequent pulses from a comb laser to microjoules (Witte *et al*. 2005, Zinkstok *et al*. 2006) and even milli-joules level (Kandula *et al*. 2008). With pulse lengths in the 100 fs–1 ps range, this is sufficient to generate HHG. By amplifying and upconversion of subsequent pulses, one retains the mode spacing of the original comb, but the shape of the modes changes. In Figure 33, the comb mode shape is shown for 1, 2, and 10 pulses. It can be seen that two pulses already contain the essential information of the comb line positions, but that the mode structure resembles a cosine-modulated spectrum. The maxima of the cosine correspond to the positions of the original comb modes, and for many more pulses one obtains a narrow comb mode spectrum again. Excitation with more pulses,

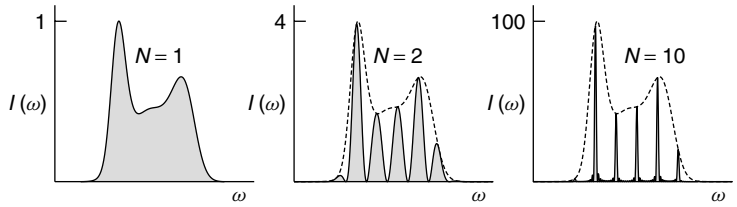

Figure 33 Relationship between the number of phase-coherent pulses N (with a fixed phase difference) and the resulting spectrum in the frequency domain. [Reproduced from Witte (2008).]

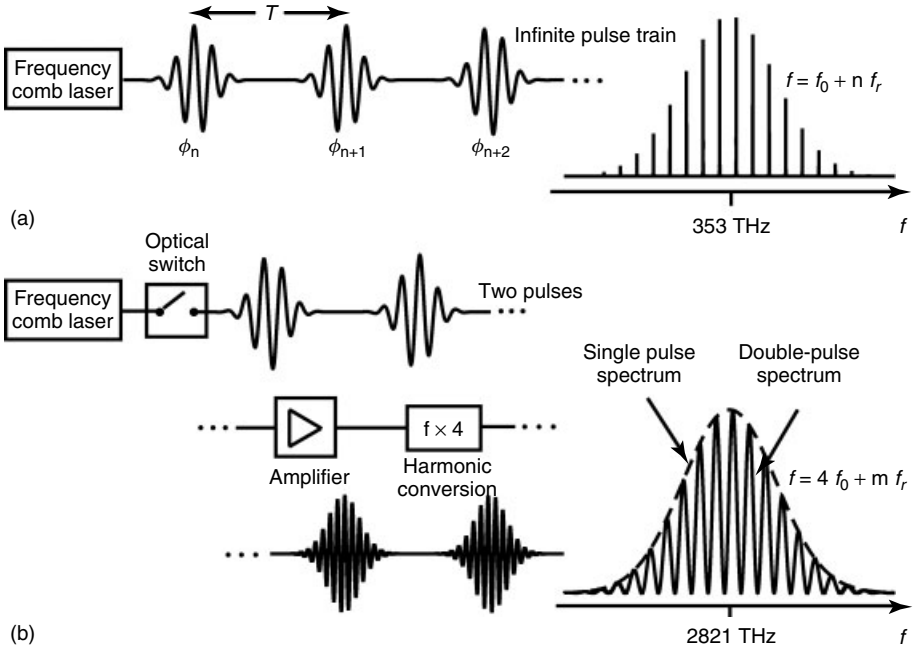

Figure 34 Excitation with frequency comb lasers. (a) At a full repetition rate, the excitation spectrum consists of narrow modes. (b) The spectrum after selection of two pulses, amplification and fourth harmonic generation, resulting in a cosine-like frequency comb in the UV.

therefore, leads to narrower modes and resonances. Unfortunately, it is difficult to control and measure phase distortions of the pulses if there are more than two of them involved in the excitation process. In the following description of the excitation process, we, therefore, concentrate only on the case of two pulses. It is shown that reducing the comb to two pulses hardly compromises the resolution one can obtain. Experimentally the situation can look as depicted in Figure 34. Instead of using the full repetition rate (Figure 34a), only two pulses are selected, which are then amplified and upconverted (Figure 34b).

To calculate the consequences of using only two pulses, we assume a two-level atom that is excited in a one-photon transition. The ground state is denoted by $|g\rangle$ with amplitude c_g, and the excited state by $|e\rangle$ with amplitude c_e. The laser pulses are taken with a square intensity envelope (duration τ), and a central frequency ω_L. In this way, the equations of motion can be readily solved. Only the main results are given here; for a full account, see (Witte 2008). We start with writing the wave function of a two-level atom as

$$|\psi\rangle = \begin{pmatrix} c_\mathrm{e} \\ c_g \end{pmatrix} \tag{30}$$

The atom is excited by an approximately resonant laser field $\boldsymbol{E}(t) = \boldsymbol{E}_0(\mathrm{e}^{\mathrm{i}\omega_L t} + \mathrm{e}^{-\mathrm{i}\omega_L t})$. In the dipole approximation and after transformation to a frame rotating with the laser frequency, the Schrödinger equation of the system can be written as (Cohen-Tannoudji *et al.* 1977)

$$\begin{aligned} \mathrm{i}\hbar\frac{\partial|\psi\rangle}{\partial t} &= \hbar\begin{pmatrix} -\frac{1}{2}(\omega_L-\omega_0) & -\mathrm{i}\Omega(1+\mathrm{e}^{2\mathrm{i}\omega_L t}) \\ \mathrm{i}\Omega^*(1+e^{-2i\omega_L t}) & \frac{1}{2}(\omega_L-\omega_0) \end{pmatrix}|\psi\rangle \\ &\approx \hbar\begin{pmatrix} -\frac{\Delta}{2} & -\Omega \\ -\Omega^* & \frac{\Delta}{2} \end{pmatrix}|\psi\rangle \end{aligned} \tag{31}$$

where $\Omega = \boldsymbol{d}\cdot\boldsymbol{E}_0/\hbar$ is the Rabi frequency, $\omega_0 = (E_\mathrm{e} - E_g)/\hbar$ is the angular transition frequency between $|g\rangle$ and

$|e\rangle$, and $\boldsymbol{d}$ is the dipole operator. In the last step, a detuning $\Delta = \omega_L - \omega_0$ is introduced, and the rotating-wave approximation has been applied. As a result, equation (31) is now time independent, allowing direct integration. We assume that the atoms are initially in the ground state. The excitation amplitude after just one square pulse with a length τ is then equal to

$$\begin{pmatrix} c_e(\tau) \\ c_g(\tau) \end{pmatrix} = \begin{pmatrix} \mathrm{i}\frac{\Omega}{a}\sin a\tau \\ \cos a\tau - \mathrm{i}\frac{\Delta}{2a}\sin a\tau \end{pmatrix} \tag{32}$$

where $a = \sqrt{\left(\frac{\Delta}{2}\right)^2 + |\Omega|^2}$ is known as the *Rabi flopping frequency* for a certain detuning Δ. The amplitudes of both levels undergo Rabi oscillations as a function of time, determined by the Rabi flopping frequency a. For small times τ, the excited state amplitude τ is mostly determined by the electric field strength through the Rabi frequency Ω.

For DFCS, the atom needs to interact with at least one additional pulse. The pulse shape is again approximated as a square to neglect any possible time dependence of Ω (this approximation holds only when the pulses are relatively weak, $\Omega\tau \ll 1$). In between the pulses, the atoms evolve field free with a phase evolution equal to $\omega_0 t$. When the second pulse interacts with the atom after a delay T, the phase of the additional excited state amplitude depends on the phase of the light field. The electric field of the second pulse is taken identical to that of the first pulse, aside from a time delay T and a phase shift φ:

$$\boldsymbol{E}(t) = \boldsymbol{E}_0(\mathrm{e}^{\mathrm{i}\omega_L(t-T)-\mathrm{i}\varphi} + \mathrm{e}^{-\mathrm{i}\omega_L(t-T)-\mathrm{i}\varphi}) \tag{33}$$

After the pulse sequence, the resulting excited state amplitude is found to be:

$$\begin{aligned} c_{e2} &= \frac{2\Omega\sin a\tau}{a^2}\left(a\cos a\tau\cos\frac{1}{2}(\tau\Delta - \omega_0 T - \varphi)\right. \\ &\quad \left. + \frac{\Delta}{2}\sin a\tau\sin\frac{1}{2}(\tau\Delta - \omega_0 T - \varphi)\right) \\ &= -\frac{2c_{e1}}{a}\left(\cos\frac{\omega_0 T + \varphi}{2}\left(a\cos a\tau\cos\frac{\tau\Delta}{2}\right.\right. \\ &\quad \left. + \frac{\Delta}{2}\sin a\tau\sin\frac{\tau\Delta}{2}\right) + \sin\frac{\omega_0 T + \varphi}{2} \\ &\quad \left.\times\left(a\cos a\tau\sin\frac{\tau\Delta}{2} - \frac{\Delta}{2}\sin a\tau\cos\frac{\tau\Delta}{2}\right)\right) \end{aligned} \tag{34}$$

This fairly complicated expression can be simplified if we assume that $\Omega \ll \Delta$, so that $a \approx \Delta/2$. The resulting final excited state population is then (Salour 1978)

$$|c_{e2}|^2 = 4|c_{e1}|^2\cos^2\left(\frac{\omega_0 T + \varphi}{2}\right) \tag{35}$$

In this approximation, the excited state population does not depend on the detuning and Rabi frequency, but only on the transition frequency ω_0, and the time delay T and phase shift φ between the pulses. These are exactly the parameters that are controlled to a high degree in a frequency comb. The time delay T is equal to $1/f_{\mathrm{rep}}$, while $\varphi = \Delta\phi_{\mathrm{ce}} = 2\pi f_0/f_{\mathrm{rep}}$. Excitation with only a pair of pulses emitted by a frequency comb laser is, therefore, enough to perform DFCS. It is also clearly similar to Ramsey spectroscopy with spatially separated fields (Ramsey 1949).

For pulse trains consisting of N pulses, a formula analogous to equation (35) can be derived, which has the following form:

$$|c_{eN}|^2 = N^2|c_{e1}|^2\left|\sum_{n=0}^{N}\mathrm{e}^{\mathrm{i}n(\omega_0 T+\varphi)}\right|^2 \tag{36}$$

This expression is basically the same as the formulas that describe the formation of a frequency comb from a finite number of phase-locked pulses. As a result, the measurement of the excited state population as a function of either T or ϕ_{ce} will result in a spectrum that consists of a regularly spaced comb of peaks separated by $1/T$ that become narrower when more pulses are used. Interaction of a two-level system with a pair of consecutive frequency comb pulses, therefore, leads to an excitation probability that mimics the frequency comb structure.

Figure 35 shows the excited state population as predicted by equation (36) for trains of up to four laser pulses. The parameters are $T = 13$ ns, $\varphi = 0$, and $\omega_0 = 2821$ THz. This figure shows the expected narrowing of the signal for an increasing number of pulses and the maximum intensities of the fringes scale with N^2.

In contrast to traditional spectroscopy, the accuracy is not limited by the spectral characteristics of the individual pulses, but only by the reproducibility of the pulses, which can be extremely good when a frequency comb is employed. Therefore, direct excitation with phase-coherent pulse trains provides a good alternative to high-precision metrology with narrowband CW lasers. Since the high peak power of typical ultrashort-pulsed lasers can exceed a terawatt, frequency conversion of such pulses using nonlinear optics and HHG can be performed very efficiently.

Expression (35) that describes the excited state population as a function of time delay T and phase shift φ is an approximation of the more general solution (34) for the case where $a \approx \Delta/2$ or rather where both $\tau\Delta \ll 1$ and $\Omega\tau \ll 1$. This approximation basically assumes that the excited state population remains negligible compared to that of the ground state and that coherent accumulation effects such as Rabi oscillations are not significant. To investigate the conditions for which these assumptions hold,

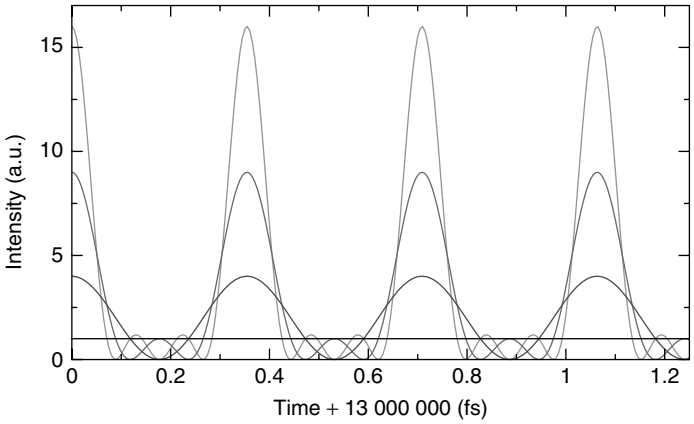

Figure 35 Excited state population as a function of the time delay T for 1 pulse (black horizontal curve), up to four pulses (light gray curve). The repetition rate is 75 MHz and $\Phi_{\mathrm{ce}} = 0$. [Reproduced from Witte (2008).]

one can rewrite the terms in equation (34) using the Taylor expansions $\sin x = x + \cdots$ and $\cos x = 1 - \frac{1}{2}x^2 + \cdots$, which leads to

$$c_{e2} \approx -2c_{e1}\left[\left(1 - \frac{1}{2}|\Omega|^2\tau^2\right)\cos\frac{\omega_0 T + \varphi}{2} - \frac{1}{2}\frac{\Delta}{2}|\Omega|^2\tau^3 \sin\frac{\omega_0 T + \varphi}{2}\right] \tag{37}$$

where any terms of order τ^4 and higher are neglected. From this equation, it follows that equation (35) is valid if the detuning Δ is small. This detuning is the difference in frequency between the transition frequency ω_0 and the carrier wave ω_L of the square laser pulse. If a comb spectrum is used that is symmetric and centered around ω_0, we have $\Delta = 0$, and no shift is expected at all. Otherwise, the requirement is that $\Omega\tau \ll 1$, which is, in practice, easily met. If we, e.g., assume a fairly big $\Omega\tau = 0.2$, then a detuning of $\Delta/2 = 1/\tau$ is required to induce a phase shift of about 42 mrad (= 1/150th of a cycle). However, since $1/\tau$ is on the order of the spectral bandwidth of the pulses, the excitation probability will go down rapidly for such a large detuning. Therefore, equation (35) should describe the experimentally observed signals very well for any reasonable set of parameters Δ, Ω, and τ. Any phase shifts due to the detuning and Rabi frequency can easily be kept within ~ 0.1 mrad ($\sim 10^{-5}$ of a cycle), which is usually far below the experimental accuracy with which a measured oscillatory pattern can be fitted.

It should be noted that although, in practice, the theory presented in this section forms a very good approximation (which is confirmed in the following section), a more detailed analysis using real experimental parameters and including, e.g., pulse envelopes, Doppler broadening, etc., requires numerical integration of a set of Bloch equations for the density matrix of the system (Zinkstok 2008). An example of such a calculation can be seen in Figure 36.

5.5 Two-photon Doppler-free Excitation and Light Shifts

In single-photon spectroscopy with comb lasers, only one mode is resonant. All the other modes can, e.g., still produce background signal from scattering, even if spectral filtering is used. There can also be a Doppler shift, depending on the excitation geometry and speed of the atoms. Both drawbacks can be significantly reduced by Doppler-free DFCS. Already in 1977 it was realized that Doppler-free excitation can be performed on two-photon resonances with pulses (Baklanov and Chebotaev 1977), similar to the case of CW excitation. The requirement is that the pulses come from opposite sides and overlap in the interaction region. In Figure 37, the situation is sketched in the time and frequency domain. It is particularly interesting to note that not just one but almost all of the comb modes can now contribute to the signal. Suppose that a mode in the comb spectrum ω_m is two-photon resonant with the resonance at ω_r, so $2\omega_m = \omega_r$. Then, also a combination of one mode up and one down is resonant: $\omega_{m-1} + \omega_{m+1} = \omega_r$. This hold for all combinations $\omega_{\mathrm{m-p}} + \omega_{\mathrm{m+p}}$, so that most modes can effectively contribute to the signal. The signal is, therefore, significantly enhanced in this way. In fact, the DFCS signal with counter-propagating beams is of the same order of magnitude as if the laser beams would have been CW (Baklanov and Chebotaev 1977). The only apparent difference is that the Doppler shift compensation for a combination of different modes is not perfect because of the difference in frequency. It leads to imperfect Doppler cancellation and, therefore, to a broadening of the measured resonance. This is equivalent to time-of-flight broadening:

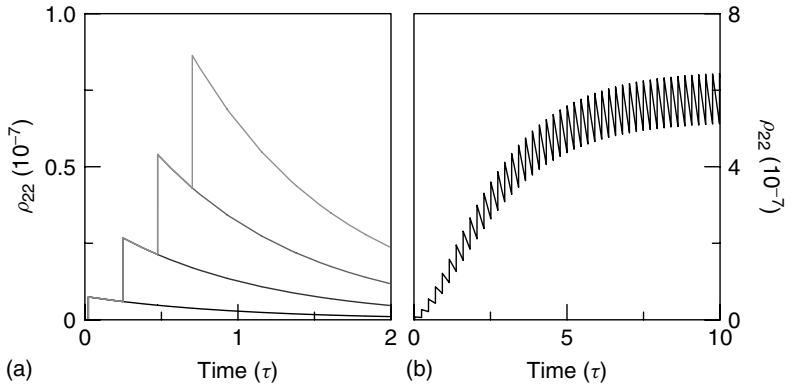

Figure 36 Numeric calculation of the excited state population $\rho_{22} = |c_e|^2$ for a varying number of phase-locked laser pulses. (a) Excitation for 1–4 pulses. (b) The same, but up to 42 pulses. Time is in units of the upper state lifetime τ and the delay between the pulses is 0.22τ. [Reproduced from Zinkstok (2008).]

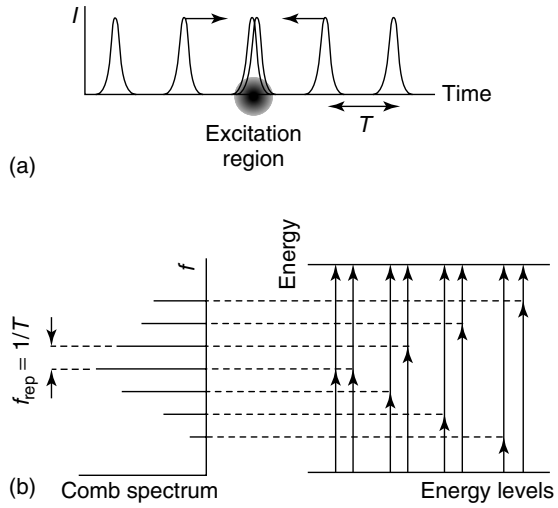

Figure 37 Schematic representation of two-photon excitation with frequency combs. (a) Time domain picture with pulses coming from opposite sides. (b) Frequency domain picture, showing how different modes add up to (approximately) the same transition energy.

viewed in the frequency domain, one can say that shorter pulses lead to a wider spectrum and, therefore, to less ideal Doppler compensation. Similarly, in the time domain shorter pulses lead to a smaller interaction zone, because the overlap region scales with the pulse duration (Figure 37). Therefore, the interaction time reduces for shorter pulses, resulting in a larger time-of-flight broadening. It is, therefore, useful to use relatively long pulses (in the ps range) for Doppler-free DFCS. Because excitation with frequency combs is so similar to CW excitation, one might suspect that, e.g., AC-Stark shifts from the comb pulses have its CW equivalence too. This is indeed the case. With DFCS the instantaneous peak power can be very high, leading to strong shifts of the energy levels. However, these shifts last only for the duration of the pulses. In between the pulses, when there is no field, light shift is also not there. Because the AC-Stark shift is linear in intensity, it simply scales with the effective *average power* during excitation. This was verified in an experiment with DFCS on the 6s–8s transition in cesium at 2×822 nm (Fendel *et al*. 2007).

For DFCS in the XUV, this should work the same way. One issue though is the square-law intensity dependency of the excitation probability for a two-photon transition. With a typical conversion efficiency of HHG on the order of 10^{-6}, one might not expect much signal. However, two-photon excitation of, e.g., helium with XUV pulses from HHG has already been demonstrated (Papadogiannis *et al*. 2003, Nabekawa *et al*. 2005).

It should also be realized that the cancellation of the Doppler *shift* works only for an isotropic velocity distribution of the atoms (such as in a closed vapor cell). If there is a preferred direction (like in an atomic beam), then Doppler shift cancellation requires exactly counter-propagating and wavefront identical XUV beams, which can be quite challenging to achieve. Alternatively, one can store the atoms in a trap for DFCS to convert the atomic motion into a periodic one. This was studied theoretically for DFCS of He^+ ions in a Paul trap (Herrmann *et al*. 2009). It was found that for sufficiently low temperature and few ions, one can then distinguish the carrier (Doppler-free transition) from the side bands, although only very low signal levels are expected with current technology. We can, therefore, conclude that DFCS is very promising to perform high-resolution spectroscopy in the XUV, but there are still several challenges.

5.6 Two-pulse Direct Frequency Comb Excitation

Up to now, the possibilities of DFCS have been discussed for the XUV with few and many (upconverted) pulses.

In the following paragraph, we focus on the experimental issues involved, in particular for two-pulse DFCS. There are several advantages to amplification and upconversion of only a few pulses for DFCS. An important one is the high power per pulse, which is favorable for the efficiency of harmonic generation and, therefore, for signal detection. Another advantage is the greater flexibility, e.g., easy separation of XUV from the original IR light and the use of pulsed atomic beams for higher gas densities. However, there are also clear drawbacks. The most important one is that subsequent pulses do not necessarily experience the same conditions in the amplification or harmonic upconversion. For example, the first pulse might introduce some ionization of the HHG medium (typically, a noble gas such as xenon), which can then lead to a phase shift $\delta\phi_{1,\mathrm{ir}}$. The second pulse introduces more ionization, and a different phase shift $\delta\phi_{2,\mathrm{ir}}$ for the second pulse. However, one should keep in mind that only the *differential phase shift* $\delta\phi_{12,\mathrm{ir}} = \delta\phi_{2,\mathrm{ir}} - \delta\phi_{1,\mathrm{ir}}$ between the pulses matters for the calibration according to equation (35). This relaxes the required conditions considerably, e.g., for frequency chirp in the pulses. Significant chirp in ultrafast pulses is quite common, e.g., from residual effects of chirped-pulse amplification. However, it is of no consequence as long as the chirp is identical in all pulses. This is true for chirp due to geometrical effects (stretching and compression) if the pulses follow the same path through the whole optical system. In addition, self-phase modulation (SFM) is not a big issue if one makes sure that the pulses have the same pulse length and intensity, so that equal phase shifts result. Identical SFM can change the overall comb spectrum envelope function (the dashed line in Figure 33), but it leaves the individual modes in their original positions.

If, however, there is a significant $\delta\phi_{12,\mathrm{ir}}$ between the amplified comb pulses before upconversion, the effect of it will be multiplied by the frequency upconversion and the number of photons involved in the excitation process. Apart from effects due to ionization, the harmonic upconversion process itself can also cause a phase shift (see Section 5.3), linear in intensity of the fundamental wavelength, which can lead to a differential XUV phase shift $\delta\phi_{12,xuv}$. For the total error in the transition frequency, we write

$$\Delta f_{\mathrm{error}} = m(q\delta\phi_{12,\mathrm{ir}} + \delta\phi_{12,xuv})\, f_{\mathrm{rep}}/2\pi \qquad (38)$$

where m is the amount of XUV photons involved in the transition and q is the harmonic order. From this equation, we can draw several conclusions. First, one has to very carefully characterize the phase shifts introduced in all the processes from the comb laser onward (see below), especially those shifts before harmonic generation. Second, the error scales linearly with the pulse repetition rate or inversely proportional to the pulse delay T. This means that the influence of phase shifts becomes progressively smaller for longer pulse delays.

Pulsed excitation with two harmonically upconverted pulses was shown for the first time at 85 nm in krypton (Cavalieri *et al*. 2002). Starting with single $\approx 100\, fs$ pulses from a Ti : sapphire oscillator–amplifier system, a double-pulse was generated with a variable time delay using a Michelson interferometer. Both pulses were then upconverted in the same gas jet to 88 nm (9th harmonic) and used to excite continuum states above the ionization threshold in krypton. An oscillating signal could be recorded as a function of the pulse delay (up to $\approx 200\, fs$). This experiment showed that the phase shifts in HHG generation can be kept stable enough in experiments to observe Ramsey fringes in the XUV. However, it is very difficult to control and measure the phase differences between the pulses from a Michelson interferometer. Therefore, no absolute calibration could be performed with this method so far (Pirri *et al*. 2008).

The solution to this problem is to start with pulses of which the phase difference is known from the start with high precision: a frequency comb laser. The first demonstration of this principle, DFCS with amplification and upconversion of a frequency comb, involved excitation of krypton at 212.55 nm on a two-photon transition (Witte *et al*. 2005). A special Ti : sapphire-based amplifier (Figure 38) was developed for this purpose that could amplify multiple pulses from a frequency comb at 848 nm. This comb laser (also Ti : sapphire-based) operated at a repetition rate of 75 MHz and was stabilized to a global positioning system (GPS)-disciplined Rb atomic clock. With Pockels cells, a few pulses were selected for amplification to the 50 μJ level, and frequency-doubling was performed twice in BBO crystals to obtain the required 212.55 nm. After excitation of krypton with these pulses, excited atoms were ionized by a 60 ps laser pulse at 532 nm and the ions detected via a time-of-flight mass separator. Spectroscopy is performed with such a system by changing the pulse delay with the frequency comb laser (so by tuning f_{rep}, but keeping f_0 equal).

It should be noted that special effort was made to amplify only a *narrow bandwidth* of 0.5 nm from the total spectrum of the comb laser (FWHM of $\approx$ 100 nm). This was achieved with a combination of an interference filter and grating-slit combination *within the amplifier*, as can be seen in Figure 38. In this way, one can make sure that only one transition is excited at the time. Simultaneous excitation of multiple transitions would lead to a reduced contrast and an unknown shift of the interference pattern and, hence, to a systematic error.

In Figure 39(a), the krypton ion signal is shown for excitation with one to three upconverted frequency comb pulses. For each data point the time delay between the pulses (13.3 ns) was adjusted in steps of 12 as. With two

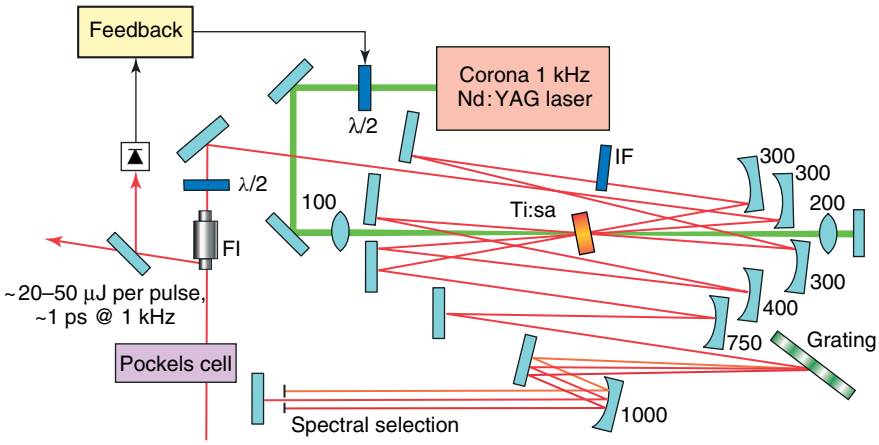

Figure 38 Six-pass Ti : sapphire amplifier of frequency comb pulses (injected bottom-left just before the Pockles cell) designed to amplify up to six subsequent pulses in nonsaturation mode. FI: Faraday isolator, $\lambda/2$: half-wave plate, Ti : Sa: titanium : sapphire crystal, IF: interference filter. The numbers in the figure indicate the radii of curvature and focal lengths in units of millimeter. [Reproduced from Zinkstok (2008).]

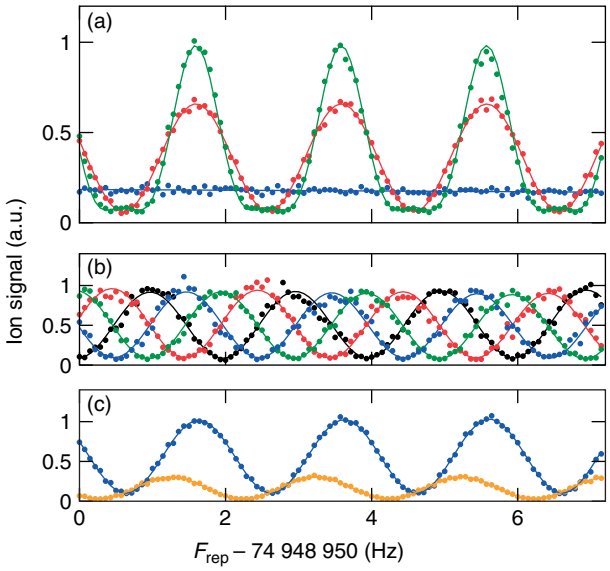

Figure 39 Direct frequency comb spectroscopy at 212.55 nm on the $4p^6 \rightarrow 4p^5 5p[1/2]_0$ transition in krypton using pulses 13.3 ns apart. (a) ^{84}Kr ion signal as a function of the repetition rate of the comb laser for one, two, and three pulses, leading to, respectively, a flat line, a cosine modulation, and a sync-like shape. (b) Measurement for different carrier–envelope phase shifts. (c) Isotope shift measurement by recording the signal of ^{84}Kr (the stronger signal) and ^{86}Kr (the weaker signal) simultaneously. [Reproduced from Witte *et al.* (2005).]

pulses, a nearly perfect cosine-like spectrum is recorded. Going from two to three pulses, the resonances become narrower and more comb-like, as expected from equations (35) and (36). A shift in the carrier–envelope phase shift leads to a shift of the ion signal, as can be seen in Figure 39(b). At the maxima of the signal, the frequency comb modes (times eight because of the frequency quadrupling and the two-photon transition) come into resonance with the transition. Therefore, the pattern repeats itself after the mode spacing of 75 MHz. This shows one of the complications of using frequency combs for excitation: one has to determine which mode of the comb laser is resonant at each maximum of the signal. A previous calibration by other means at an accuracy far better than f_{rep} can resolve this issue. If this is not available, one can repeat the measurement at several f_{rep}. Near the expected transition frequency, the calibration for the proper mode will coincide. This method has been applied for the krypton measurement, leading to a new value for the $4p^6 \rightarrow 4p^5 5p[1/2]_0$ transition of 2 820 833 097.7 (3.5) MHz. This is an order of magnitude better than the previous determination (Brandi *et al.* 2002) using single nanosecond-timescale laser pulses. Isotope-shift measurements have also been performed, as shown in Figure 39(c). In this case, the signal of two isotopes was recorded simultaneously.

A full length discussion of all the systematic effects and errors is out of scope here, but can be found in (Zinkstok 2008, Witte *et al.* 2005).

5.7 Detection of Phase Distortions from Amplification

One aspect deserves special attention in a two-pulse DFCS experiment: the differential phase shift from the amplification process. According to Section 5.6, this phase shift can give significant calibration errors. For example, for the two-photon krypton experiment (Witte *et al.* 2005), we have $q = 4$, $m = 2$, and $f_{rep} = 75$ MHz, so that 100 mrad phase error (1/60th of a wavelength) leads to an error of

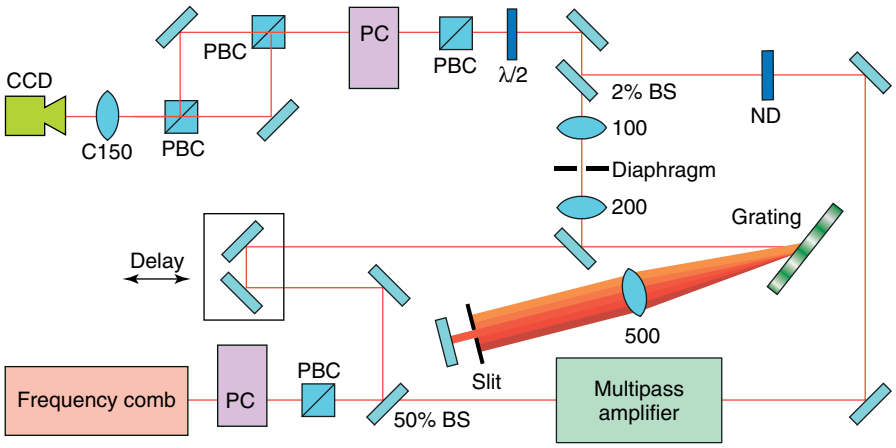

Figure 40 Spectral interferometry setup to measure differential phase shifts between pulses due to amplification. PBC: polarizing beam splitter cube, BS: beam splitter, C:cylindrical lens, and ND: neutral density filter. The grating in combination with the lens $f = 500\,\text{mm}$ forms a $4f$ system. Focal lengths (in millimeter) are indicated by the numbers in the figure. [Reproduced from Zinkstok (2008).]

9.5 MHz at the transition frequency. It is, therefore, very important to measure this differential phase shift with high accuracy. In Figure 40, the setup for such a measurement is shown, based on a Mach–Zehnder interferometer. Part of the light from each comb pulse is split off to serve as a phase reference for the part that travels through the amplifier. After the amplifier, the amplified and reference pulses are recombined with a small time delay of $\approx 1\,\text{ps}$. The phase difference between the two amplified pulses is then measured by recording spectral fringes in a spectrometer consisting of a grating and a CCD camera. To determine the differential phase shift, the patterns of the two amplified pulses with their reference pulses must be spatially separated. Therefore, an additional Pockels cell is used in combination with polarizing optics. Between the two amplified pulses (time delay in the nanoseconds range), the Pockels cell rotates the polarization by 90° so that the second pulse (with reference pulse) is taking a different optical route. In this way, the patterns can be projected above each other, as shown in Figure 41. The differential phase shift between the pulses is measured as a phase (horizontal position) difference of the two patterns. However, any misalignment of the position on the camera of the two patterns leads to a false phase shift reading. The solution is exchanging the projections (up vs down) of the two interference patterns. This is done using the Pockels cell that rotates the polarization of the first or second amplified pulse (with reference). If there is no real differential phase shift, then both projections will lead to the same relative position of the interference patterns, so that a zero difference phase shift is measured. However, for a real phase shift, the difference is equal to *twice the differential phase shift*. Geometrical and real phase shifts could be distinguished in this manner with an accuracy of 25 mrad (Witte *et al.* 2005). An improved version at a level of 5 mrad was demonstrated by Kandula *et al.* (2008) for characterizing the beam from an optical parametric amplifier. One should bear in mind though that the phase shifts can vary spatially across the beam on a level of 30–100 mrad for such an amplifier (Kandula *et al.* 2008). However, it seems feasible to determine the average effective phase shift at a level of 10 mrad or better. If we translate this to an experiment in the XUV, using, e.g., the 15th harmonic of 800 nm and a pulse delay of $T = 10\,\text{ns}$, then the uncertainty due to amplifier phase shifts would be only 2.4 MHz at 53 nm. A longer delay between the pulses would reduce this error proportionally so that even submega-hertz resolution might be achieved in the XUV. In effect there are actually two ways of achieving high resolution: either by using more than two pulses or by taking two pulses further apart according to equation (36).

5.8 Frequency Comb Excitation in the VUV

The principles described in the previous section were demonstrated with a DFCS experiment in Xe (Zinkstok *et al.* 2006) at 125 nm. Frequency comb pulses at 730 nm were amplified (up to six subsequent pulses) in a

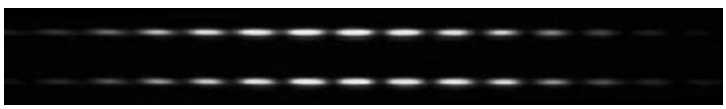

Figure 41 CCD recording of two spectral interferograms over ≈0.5 nm bandwidth.

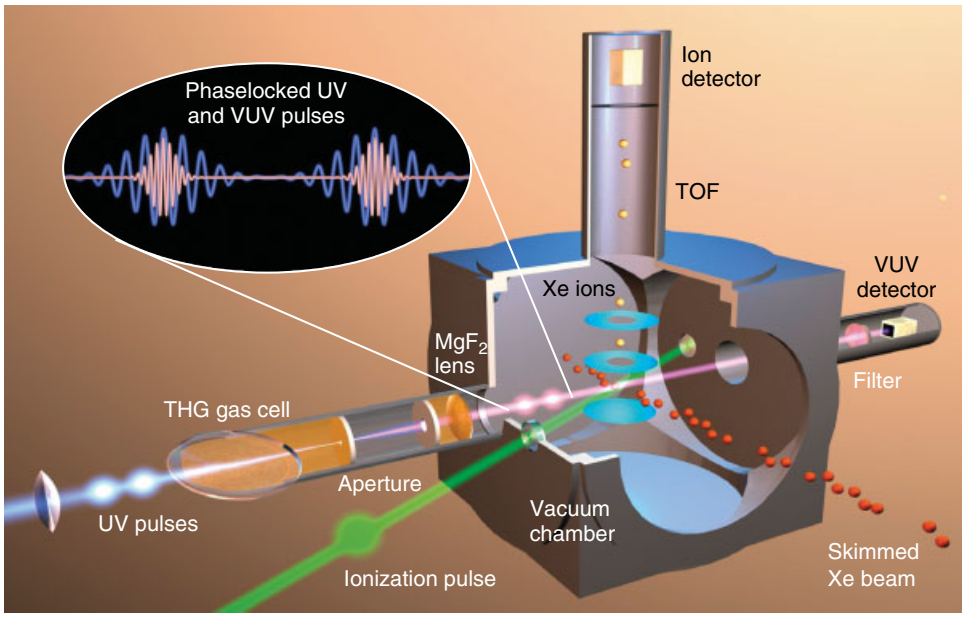

Figure 42 Experimental setup for DFCS at 125 in xenon. TOF: time-of-flight mass spectrometer and THG: third-harmonic generation. [Reproduced from Zinkstok *et al*. (2006).]

Ti : sapphire amplifier and frequency doubled in a BBO crystal (β-barium-borate). The resulting UV pulses were then tripled in a gas cell to reach 125 nm. Excitation of xenon on the $5p^6\ {}^1S_0 \rightarrow 5p^5\ {}^2P_{3/2}\ 5d[1/2]_1$ transition took place in a crossed beam geometry to reduce Doppler broadening, and the detection of the excited state population was performed by monitoring the ions produced by a delayed ionization laser at 532 nm (Figure 42).

In Figure 43, the ^{132}Xe excitation probability is shown on the left-hand side as a function of the repetition rate of the pulses, for 2–6 pulses. More pulses lead to narrower resonances, as is expected based on equation (36). One can also see that the position of the peaks is not exactly equal going from two to more pulses. This has to do with uncontrolled phase shifts in the amplifier. For more than two pulses, it becomes unpractical to measure these

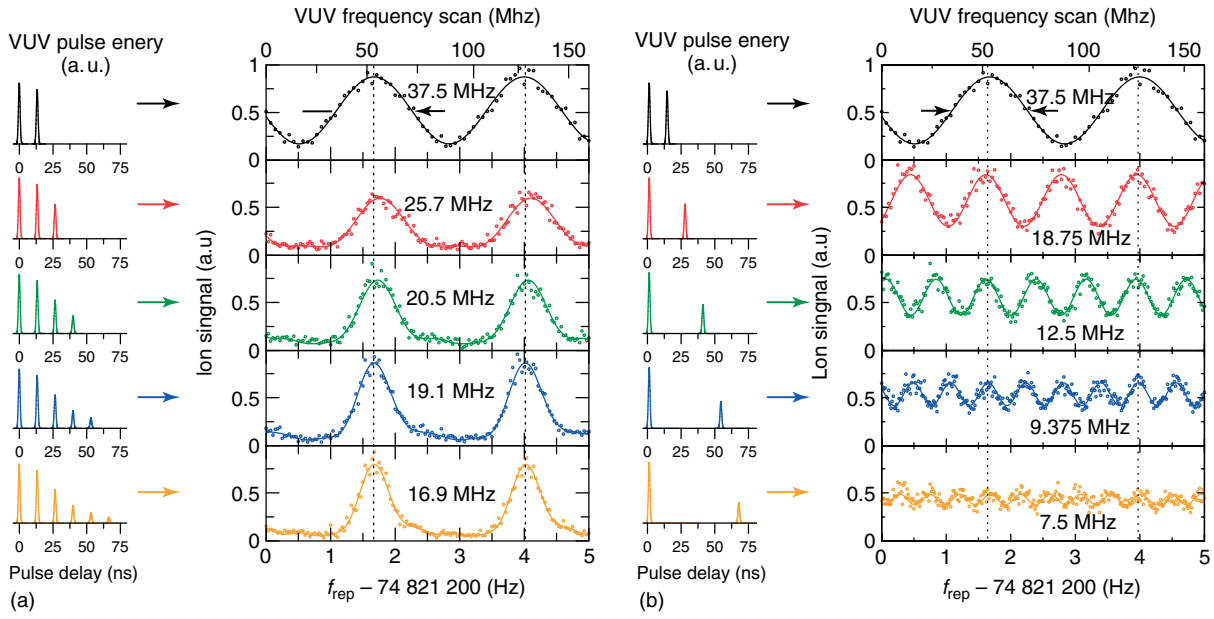

Figure 43 DFCS in xenon at 125 nm as a function of the f_{rep} of the frequency comb laser. (a) Ion signal for 1–6 VUV pulses. (b) Ion signal for 2 pulses, for different time delays. [Reproduced from Zinkstok *et al*. (2006).]

phase shifts. The calibration error that this results in can be observed as a difference between the peak positions and the dashed line that indicates the position for two-pulse excitation. The solution to this problem is shown in Figure 43 on the right-hand side. In this case, only two pulses are used, at multiples of the original frequency comb pulse repetition time. The differential phase shift can then be measured with high accuracy to correct for shifts in the peak positions (as discussed in the previous section). A high resolution is then obtained by using a longer time delay between the pulses. Figure 43 also shows that it is beneficial to start with a short time delay (high effective "f_{rep}"). Such a measurement can be used to pinpoint the transition by determining the mode number n within the range of f_{rep}. Once this is achieved, one can increase the delay as shown in Figure 43 (right-hand side) to increase the resolution of the measurement according to equation (35).

By increasing the time delay with $T = 1/f_{\mathrm{rep}}$, one can zoom in on the transition without losing the track of the mode number n that is used for the measurement at each peak in the spectrum. It can be seen that a longer delay also leads to a reduced contrast. This is the result of a reduced amplitude from the first pulse (due to a lifetime of the upper state of 59 ns and due to a Doppler width in the experiment on the order of 10 MHz). These two effects are far less of an issue if one excites a two-photon transition (with a long life time) and reduced Doppler broadening. As far as the absolute calibration of the Xe transition is concerned, the $5p^6\ {}^1S_0 \rightarrow 5p^5\ {}^2P_{3/2}\ 5d[1/2]_1$ transition is not known accurately enough (better then $f_{\mathrm{rep}} = 75$ MHz) from a previous experiment to find the mode n. Even so, tests were done on phase shifts introduced by the harmonic generation, but no significant differential phase shift was seen. Therefore, precise absolute calibration is, in principle, possible with this method.

Although no absolute calibration was performed for Xe, the VUV comb spectrum was broad enough to excite many isotopes at the same time. This allowed us to measure isotope shifts in a straightforward manner, by counting the ions from two isotopes at the same time. In Figure 44, the signal of the different isotopes is shown in comparison with the main isotope ^{132}Xe. Most of the systematic shifts are almost identical, such as Doppler shifts. In combination with previous measurements to levels involved in the transition, the isotope shifts could be determined with an accuracy of ≈ 1 MHz (Zinkstok 2008).

The demonstration of DFCS in xenon is, strictly speaking, not performed in the XUV but in the VUV. However, all ingredients for successful DFCS in the XUV have been demonstrated by it. The next step would be to use higher

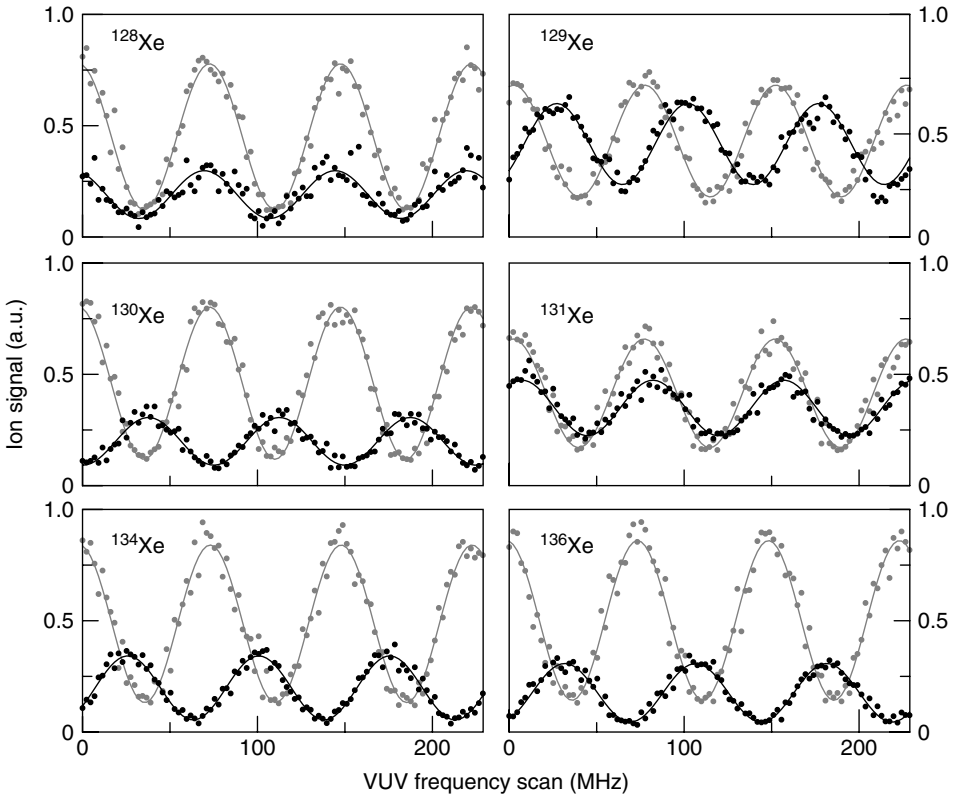

Figure 44 Isotope shift measurements using DFCS with two 125 nm pulses, 13.3 ns apart ($f_{\mathrm{rep}} = 75$ MHz). [Reproduced from Zinkstok (2008).]

harmonics and longer pulse delays to achieve megahertz or even kilohertz resolution in the XUV. One idea pursued in our lab is to excite the $1s^2\ ^1S_0 \rightarrow 1s5p\ ^1P_1$ transition at 51.6 nm of He with two phase-coherent XUV pulses about 10 ns apart, aiming for an accuracy of 15 MHz or better. The pulses will be generated by a combination of a double-pulse parametric amplifier (Kandula *et al*. 2008) and 15th harmonic generation in krypton.

6 CONCLUSION

We have discussed VUV-XUV generation for a wide range of conditions and spectroscopic applications. Precision laser spectroscopy in atoms and molecules at wavelengths ranging from 200 to 100 nm using nanosecond-timescale laser pulses is now very well established at the 10 MHz level. Spectroscopy at shorter wavelengths is also possible, but usually requires lasers with higher peak power and shorter pulses in the picosecond and femtosecond range. The resulting broader laser bandwidth hampers high precision in this case, as do frequency chirping effects. Some 10 years ago, it seemed that this would pose a severe limitation to increase the accuracy in the XUV. However, recent developments in the application and the extension of frequency comb lasers suggest that this is probably not going to be the case for much longer.

ABBREVIATIONS AND ACRONYMS

CW	continuous wave
DFCS	direct frequency comb spectroscopy
FT	Fourier-transform
GPS	global positioning system
HHG	high harmonic generation
PDA	pulsed-dye amplification
SFM	self-phase modulation
SBS	stimulated Brillouin scattering
THG	third-harmonic generation
VUV	vacuum ultraviolet
XUV	extreme ultraviolet

REFERENCES

Abgrall, H., Roueff, E., Launay, F., Roncin, J.Y., and Subtil, J.L. (1993a) Table of the Lyman band system of molecular-hydrogen. *Astronomy and Astrophysics. Supplement Series*, **101**(2), 273–321.

Abgrall, H., Roueff, E., Launay, F., Roncin, J.Y., and Subtil, J.L. (1993b) Table of the Werner band system of molecular-hydrogen. *Astronomy and Astrophysics. Supplement Series*, **101**(2), 323–362.

Adkins, G.S., Morrison, S., and Sapirstein, J. (2007) Recoil corrections in highly charged ions. *Physical Review A*, **76**(4), 042508.

Albert, S., Albert, K.K., and Quack, M. (2011) High-resolution Fourier transform infrared spectroscopy, in *Handbook of High-resolution Spectroscopy*, Quack, M. and Merkt, F. (eds), John Wiley & Sons, Ltd., Chichester, UK.

Armstrong, J.A., Bloembergen, N., Ducuing, J., and Pershan, P.S. (1962) Interactions between light waves in a nonlinear dielectric. *Physical Review*, **127**(6), 1918–1939.

Baker, J., Lemaire, J.L., Couris, S., Vient, A., Malmasson, D., and Rostas, F. (1993) A 2+1 REMPI study of the E-X transition in CO - indirect predissociations in the $E^1\Pi$ state. *Chemical Physics*, **178**(1–3), 569–579.

Baker, J., Tchang-Brillet, W.U.L., and Julienne, P.S. (1995) First observation of the $v = 3$ level of the $B\ ^1\Sigma^+$ Rydberg state of CO. *Journal of Chemical Physics*, **102**(10), 3956–3961.

Baklanov, Y.V. and Chebotaev, V.P. (1977) Narrow resonances of two-photon absorption of super-narrow pulses in a gas. *Applied Physics A*, **12**, 97–99.

Baltuska, A., Udem, T., Uiberacker, M., Hentschel, M., Goulielmakis, E., Gohle, C., Holzwarth, R., Yakoviev, V., Scrinzi, A., Hänsch, T.W. *et al*. (2003) Attosecond control of electronic processes by intense light fields. *Nature*, **421**(6923), 611–615.

Bellini, M., Bartoli, A., and Hänsch, T.W. (1997) Two-photon Fourier spectroscopy with femtosecond light pulses. *Optics Letters*, **22**(8), 540–542.

Bergeson, S.D., Balakrishnan, A., Baldwin, K.G.H., Lucatorto, T.B., Marangos, J.P., McIlrath, T.J., O'Brian, T.R., Rolston, S.L., Sansonetti, C.J., Wen, J. *et al*. (1998) Measurement of the He ground state Lamb shift via the two-photon $1^1S - 2^1S$ transition. *Physical Review Letters*, **80**(16), 3475–3478.

Bjorklund, G.C. (1975) Effects of focusing on 3rd-order nonlinear processes In isotropic media. *IEEE Journal of Quantum Electronics*, **11**(6), 287–296.

Boyd, R.W. (2003) *Nonlinear Optics*, Academic Press.

Brandi, F., Giammanco, F., and Ubachs, W. (2006) Spectral redshift in harmonic generation from plasma dynamics in the laser focus. *Physical Review Letters*, **96**(12), 123904.

Brandi, F., Hogervorst, W., and Ubachs, W. (2002) High-resolution vacuum-ultraviolet and ultraviolet photoionization spectroscopy of krypton. *Journal of Physics B*, **35**(4), 1071–1084.

Brandi, F., Neshev, D., and Ubachs, W. (2003a) High-order harmonic generation yielding tunable extreme-ultraviolet radiation of high spectral purity. *Physical Review Letters*, **91**(16), 163901.

Brandi, F., Velchev, I., Hogervorst, W., and Ubachs, W. (2001) Vacuum-ultraviolet spectroscopy of Xe: Hyperfine splittings, isotope shifts, and isotope-dependent ionization energies. *Physical Review A*, **64**(3), 032505.

Brandi, F., Velchev, I., Neshev, D., Hogervorst, W., and Ubachs, W. (2003b) A narrow-band wavelength-tunable laser system delivering high-energy 300 ps pulses in the near-infrared. *Review of Scientific Instruments*, **74**(1, Part 1), 32–37.

Cacciani, P., Brandi, F., Sprengers, J.P., Johansson, A., L'Huillier, A., Wahlstrom, C.G., and Ubachs, W. (2002) Predissociation of the $4p\pi L\ ^1\Pi$ Rydberg state of carbon monoxide. *Chemical Physics*, **282**(1), 63–73.

Cacciani, P., Hogervorst, W., and Ubachs, W. (1995) Accidental predissociation phenomena in the $E^1\Pi$, $v = 0$ and $v = 1$ states of $^{12}C^{16}O$ and $^{13}C^{16}O$. *Journal of Chemical Physics*, **102**(21), 8308–8320.

Cacciani, P., Lynga, C., L'Huillier, A., Wahlstrom, C., Ubachs, W., and Hinnen, P. (1998) Lifetime measurements of the $E^1\Pi$, $v = 0$ and $v = 1$ states of $^{12}C^{16}O$, $^{13}C^{16}O$, and $^{13}C^{18}O$. *Astrophysical Journal*, **499**(2, Part 2), L223–L226.

Cariou, J. and Luc, P. (1980) *Atlas du Spectre d'absorption de Tellure*, Laboratoire Aimeé-Cotton, CNRS II, Orsay, France.

Casey, M. (1978) *High-resolution Studies on the Absorption Spectrum of $C^{12}O$ and $C^{13}O$ in the Wavelength Region 800-1200*. Ph.D. thesis, University College Dublin.

Cavalieri, S., Eramo, R., Materazzi, M., Corsi, C., and Bellini, M. (2002) Ramsey-type spectroscopy with high-order harmonics. *Physical Review Letters*, **89**(13), 133002.

Chantler, C.T., Laming, J.M., Dietrich, D.D., Hallett, W.A., McDonald, R., and Silver, J.D. (2007) Hydrogenic Lamb shift in iron Fe^{25+} and fine-structure Lamb shift. *Physical Review A*, **76**(4), 042116.

Cohen-Tannoudji, C., Diu, B., and Laloë, F. (1977) *Quantum Mechanics*, John Wiley & Sons.

Cooper, D.M. and Langhoff, S.R. (1981) A theoretical study of selected singlet and triplet states of the CO molecule. *Journal of Chemical Physics*, **74**(2), 1200–1210.

Corkum, P.B. (1993) Plasma perspective on strong field multiphoton ionization. *Physical Review Letters*, **71**(13), 1994–1997.

Corkum, P.B. and Krausz, F. (2007) Attosecond science. *Nature Physics*, **3**(6), 381–387.

Costello, J.T., Mosnier, J.P., Kennedy, E.T., Carroll, P.K., and Osullivan, G. (1991) XUV absorption-spectroscopy with laser-produced plasmas—a review. *Physica Scripta*, **T34**, 77–92.

Cromwell, E., Trickl, T., Lee, Y.T., and Kung, A.H. (1989) Ultranarrow bandwidth VUV-XUV laser system. *Review of Scientific Instruments*, **60**(9), 2888–2892.

Drake, G.W.F., Khriplovich, I.B., Milstein, A.I., and Yelkhovsky, A.S. (1993) Energy corrections of order $mc^2\alpha^6 \ln\alpha$ in Helium. *Physical Review A*, **48**(1), R15–R17.

Drake, G.W.F. and Yan, Z.-C. (2008) High-precision spectroscopy as a test of quantum electrodynamics in light atomic systems. *Canadian Journal of Physics*, **86**(1), 45–54.

Dudley, J.M., Genty, G., and Coen, S. (2006) Supercontinuum generation in photonic crystal fiber. *Reviews of Modern Physics*, **78**(4), 1135–1184.

Ebata, T., Hosoi, N., and Ito, M. (1992) Rotational analysis of $v = 1$ level of $n = 8$ similar-to 10 Rydberg states of CO by triple resonant multiphoton spectroscopy. *Journal of Chemical Physics*, **97**(6), 3920–3930.

Eckstein, J.N., Ferguson, A.I., and Hänsch, T.W. (1978) High-resolution two-photon spectroscopy with picosecond light pulses. *Physical Review Letters*, **40**(13), 847–850.

Eidelsberg, M., Benayoun, J.J., Viala, Y., and Rostas, F. (1991) Atlas of the absorption dissociation spectra of CO and its isotopes between 91.2 nm and 115.2 nm. *Astronomy and Astrophysics. Supplement Series*, **90**(2), 231–282.

Eidelsberg, M., Launay, F., Ito, K., Matsui, T., Hinnen, P.C., Reinhold, E., Ubachs, W., and Huber, K.P. (2004) Rydberg-valence interactions of CO, and spectroscopic evidence characterizing the $C'^1\Sigma^+$ valence state. *Journal of Chemical Physics*, **121**(1), 292–308.

Eikema, K.S.E., Hogervorst, W., and Ubachs, W. (1994a) Predissociation rates in carbon-monoxide—dependence on rotational state, parity and isotope. *Chemical Physics*, **181**(1–2), 217–245.

Eikema, K.S.E., Ubachs, W., and Hogervorst, W. (1994b) Isotope shift in the neon ground-state by extreme-ultraviolet laser spectroscopy at 74 nm. *Physical Review A*, **49**(2), 803–808.

Eikema, K.S.E., Ubachs, W., Vassen, W., and Hogervorst, W. (1993) 1st Laser excitation of the ^{4}He $1\ ^1S$—$2\ ^1P$ resonance line at 58 nm. *Physical Review Letters*, **71**(11), 1690–1692.

Eikema, K.S.E., Ubachs, W., Vassen, W., and Hogervorst, W. (1997) Lamb shift measurement in the 1^1S ground state of helium. *Physical Review A*, **55**(3), 1866–1884.

Eikema, K.S.E., Walz, J., and Hänsch, T.W. (1999) Continuous wave coherent Lyman-alpha radiation. *Physical Review Letters*, **83**(19), 3828–3831.

Eikema, K.S.E., Walz, J., and Hänsch, T.W. (2001) Continuous coherent Lyman-alpha excitation of atomic hydrogen. *Physical Review Letters*, **86**(25), 5679–5682.

Fee, M.S., Danzmann, K., and Chu, S. (1992) Optical heterodyne measurement of pulsed lasers—toward high-precision pulsed spectroscopy. *Physical Review A*, **45**(7), 4911–4924.

Fendel, P., Bergeson, S.D., Udem, T., and Hänsch, T.W. (2007) Two-photon frequency comb spectroscopy of the 6s-8s transition in cesium. *Optics Letters*, **32**(6), 701–703.

Ferray, M., L'Huillier, A., Li, X.F., Lompre, L.A., Mainfray, G., and Manus, C. (1988) Multiple-harmonic conversion of 1064 nm radiation in rare-gases. *Journal of Physics B*, **21**(3), L31–L35.

Fischer, M., Kolachevsky, N., Zimmermann, M., Holzwarth, R., Udem, T., Hänsch, T.W., Abgrall, M., Grunert, J., Maksimovic, I., Bize, S., *et al*. (2004) New limits on the drift of fundamental constants from laboratory measurements. *Physical Review Letters*, **92**(23), 230802.

Gaarde, M., Salin, F., Constant, E., Balcou, P., Schafer, K., Kulander, K., and L'Huillier, A. (1999) Spatiotemporal separation of high harmonic radiation into two quantum path components. *Physical Review A*, **59**(2), 1367–1373.

Gabrielse, G. (2005) Atoms made entirely of antimatter: two methods produce slow antihydrogen, in *Advances in Atomic Molecular Physics*, Bederson, B. and Walther, H. (eds), Academic Press, pp. 155–217, Vol. 50.

Gallmann, L. and Keller, U. (2011) Femtosecond and attosecond light sources and techniques for spectroscopy, in *Handbook of High-resolution Spectroscopy*, Quack, M. and Merkt, F. (eds), John Wiley & Sons, Ltd., Chichester, UK.

Gohle, C., Udem, T., Herrmann, M., Rauschenberger, J., Holzwarth, R., Schuessler, H.A., Krausz, F., and Hänsch, T.W. (2005) A frequency comb in the extreme ultraviolet. *Nature*, **436**(7048), 234–237.

Gumberidze, A., Stohlker, T., Banas, D., Beckert, K., Beller, P., Beyer, H., Bosch, F., Hagmann, S., Kozhuharov, C., Liesen, D., *et al*. (2005) Quantum electrodynamics in strong electric fields: the ground-state lamb shift in hydrogenlike uranium. *Physical Review Letters*, **94**(22), 223001.

Hall, J.L. (2006) Nobel lecture: defining and measuring optical frequencies. *Reviews of Modern Physics*, **78**(4), 1279–1295.

Hänsch, T.W. (2006) Nobel lecture: passion for precision, *Review of Modern Physics*, **78**(4), 1297–1309.

Hannemann, S., Hollenstein, U., van Duijn, E.J., and Ubachs, W. (2005) Production of narrowband tunable extreme-ultraviolet radiation by noncollinear resonance-enhanced four-wave mixing. *Optics Letters*, **30**(12), 1494–1496.

Herrmann, M., Haas, M., Jentschura, U.D., Kottmann, F., Leibfried, D., Saathoff, G., Gohle, C., Ozawa, A., Batteiger, V., Knunz, S. *et al*. (2009) Feasibility of coherent XUV spectroscopy on the 1S-2S transition in singly ionized helium. *Physical Review A*, **79**(5), 052505.

Hartl, I., Schibli, T.R., Marcinkevicius, A., Yost, D.C., Hudson, D.D., Fermann, M.E., and Ye, J. (2007) Cavity-enhanced similariton Yb-fiber laser frequency comb: 3×10^{14} W/cm^{-2} peak intensity at 136 MHz. *Optics Letters*, **32**(19), 2870–2872.

Herzberg, G. (1958) Ionization potentials and Lamb shifts of the ground states of ^{4}He and ^{3}He. *Proceedings of the Royal Society of London. Series A, Mathematical and Physical Sciences*, **248**(1254), 309.

Hilber, G., Lago, A., and Wallenstein, R. (1987) Broadly tunable vacuum ultraviolet extreme-ultraviolet radiation generated by resonant 3rd-order frequency-conversion in krypton. *Journal of Optical Society of America B: Optical Physics*, **4**(11), 1753–1764.

Hilbig, R. and Wallenstein, R. (1982) Narrowband tunable vuv radiation generated by non-resonant sum-frequency and difference-frequency mixing in xenon and krypton. *Applied Optics*, **21**(5), 913–917.

Hinnen, P.C. (1997) *XUV-laser Spectroscopy of H_2 and the Mystery of the Diffuse Interstellar Bands*, Ph.D. thesis, Vrije Universiteit, Amsterdam.

Hinnen, P.C., Hogervorst, W., Stolte, S., and Ubachs, W. (1994) Sub-Doppler laser spectroscopy of H_2 and D_2 in the range 91–98 nm. *Canadian Journal of Physics*, **72**(11–12), 1032–1042.

Hinnen, P.C., Werners, S.E., Stolte, S., Hogervorst, W., and Ubachs, W. (1995) XUV-laser spectroscopy of HD at 92–98 nm. *Physical Review A*, **52**(6), 4425–4433.

Hollenstein, U., Palm, H., and Merkt, F. (2000) A broadly tunable extreme ultraviolet laser source with a 0.008 cm^{-1} bandwidth. *Review of Scientific Instruments*, **71**(11), 4023–4028.

Hollenstein, U., Reinhold, E., de Lange, C., and Ubachs, W. (2006) High-resolution VUV-laser spectroscopic study of the $B\,^1\Sigma^+_{(u)}$ $(v' = 0-2) \leftarrow X\,^1\Sigma^+_{(g)}$ $(v'' = 0)$ Lyman bands in H_2 and HD. *Journal of Physics B*, **39**(8), L195–L201.

Holzwarth, R., Udem, T., Hänsch, T.W., Knight, J.C., Wadsworth, W.J., and Russell, P.S.J. (2000) Optical frequency synthesizer for precision spectroscopy. *Physical Review Letters*, **85**(11), 2264–2267.

Hopfield, J.J. (1930) New ultra-violet spectrum of helium. *Astrophysical Journal*, **72**(3), 133–145.

Hopfield, J.J. and Leifson, S.W. (1923) Wave-length standards in the extreme ultra-violet. *Astrophysical Journal*, **58**(1), 59–63.

Ivanov, T.I., Roudjane, M., Vieitez, M.O., de lange, C.A., Tchang-Brillet, W.U.L., and Ubachs, W. (2008) HD as a probe for detecting mass variation on a cosmological time scale. *Physical Review Letters*, **100**(9), 093007.

Jones, D., Diddams, S., Ranka, J., Stentz, A., Windeler, R., Hall, J., and Cundiff, S. (2000) Carrier-envelope phase control of femtosecond mode-locked lasers and direct optical frequency synthesis. *Science*, **288**(5466), 635–639.

Jones, R.J., Moll, K.D., Thorpe, M.J., and Ye, J. (2005) Phase-coherent frequency combs in the vacuum ultraviolet via high-harmonic generation inside a femtosecond enhancement cavity. *Physical Review Letters*, **94**(19), 193201.

Joyeux, D., de Oliveira, N., Phalippou, D., Rodier, J.C., Vervloet, M., Polack, F., and Nahon, L. (2005) A spectrometer by Fourier transformation without separating wave, for VUV-XUV. Principles, implementation, and primary results. *Journal de Physique IV*, **127**, 77–85.

Jungen, Ch. (2011) Elements of quantum defect theory, in *Handbook of High-resolution Spectroscopy*, Quack, M. and Merkt, F. (eds), John Wiley & Sons, Ltd., Chichester, UK.

Kabir, P.K. and Salpeter, E.E. (1957) Radiative corrections to the ground-state energy of the helium atom. *Physical Review*, **108**(5), 1256–1263.

Kan, C., Capjack, C., Rankin, R., and Burnett, N. (1995) Spectral and temporal structure in high harmonic emission from ionizing atomic gases. *Physical Review A*, **52**(6), R4336–R4339.

Kandula, D.Z., Renault, A., Gohle, C., Wolf, A.L., Witte, S., Hogervorst, W., Ubachs, W., and Eikema, K.S.E. (2008) Ultrafast double-pulse parametric amplification for precision Ramsey metrology. *Optics Express*, **16**(10), 7071–7082.

Karshenboim, S. (2005) Precision physics of simple atoms: QED tests, nuclear structure and fundamental constants. *Physics Reports*, **422**(1–2), 1–63.

Kim, S., Jin, J., Kim, Y.-J., Park, I.-Y., Kim, Y., and Kim, S.-W. (2008) High-harmonic generation by resonant plasmon field enhancement. *Nature*, **453**(7196), 757–760.

Komatsu, M., Ebata, T., and Mikami, N. (1993) Rotational analysis of $n = 4-7$ Rydberg states of CO observed by ion-dip spectroscopy. *Journal of Chemical Physics*, **99**(12), 9350–9364.

Krause, J.L., Schafer, K.J., and Kulander, K.C. (1992) Calculation of photoemission from atoms subject to intense laser fields. *Physical Review A*, **45**(7), 4998–5010.

Kung, A.H. (1983) 3rd-Harmonic generation in a pulsed supersonic jet of xenon. *Optics Letters*, **8**(1), 24–26.

de Lange, A., Lang, R., van der Zande, W., and Ubachs, W. (2002) Highly excited states of gerade symmetry in molecular nitrogen. *Journal of Chemical Physics*, **116**(18), 7893–7901.

Letzelter, C., Eidelsberg, M., Rostas, F., Breton, J., and Thieblemont, B. (1987) Photoabsorption and photodissociation cross-sections of CO between 88.5 and 115 nm. *Chemical Physics*, **114**(2), 273–288.

Lewenstein, M., Balcou, P., Ivanov, M.Y., L'Huillier, A., and Corkum, P.B. (1994) Theory of high-harmonic generation by low-frequency laser fields. *Physical Review A*, **49**(3), 2117–2132.

Lewenstein, M., Salieres, P., and L'Huillier, A. (1995) Phase of the atomic polarization in high-order harmonic-generation. *Physical Review A*, **52**(6), 4747–4754.

Lewis, B.R., Gibson, S.T., Sprengers, J.P., Ubachs, W., Johansson, A., and Wahlstrom, C.G. (2005) Lifetime and predissociation yield of $^{14}N_2$ b $^1\Pi_u$ (v = 1) revisited: Effects of rotation. *Journal of Chemical Physics*, **123**(23), 236101.

Limpert, J., Roeser, F., Schimpf, D.N., Seise, E., Eidam, T., Haedrich, S., Rothhardt, J., Misas, C.J., and Tuennermann, A. (2009) High repetition rate gigawatt peak power fiber laser-systems: challenges, design, and experiment. *IEEE Journal of Selected Topics in Quantum Electronics*, **15**(1), 159–169.

Lindner, F., Stremme, W., Schatzel, M., Grasbon, F., Paulus, G., Walther, H., Hartmann, R., and Struder, L. (2003) High-order harmonic generation at a repetition rate of 100 kHz. *Physical Review A*, **68**(1), 013814.

Lyman, T. (1906) The spectrum of hydrogen in the region of extremely short wave-lengths. *Astrophysical Journal*, **23**(3), 181–210.

Lyman, T. (1914) An extension of the spectrum in the extreme ultra-violet. *Nature*, **93**, 241.

Lyman, T. (1924) The spectrum of helium in the extreme ultra-violet. *The Astrophysical Journal*, **60**(1), 1–14.

Lynga, C., Ossler, F., Metz, T., and Larsson, J. (2001) A laser system providing tunable, narrow-band radiation from 35 nm to 2 μm. *Applied Physics B*, **72**(8), 913–920.

Macklin, J.J., Kmetec, J.D., and Gordon, C.L. (1993) High-order harmonic-generation using intense femtosecond pulses. *Physical Review Letters*, **70**(6), 766–769.

Mahon, R., McIlrath, T.J., Myerscough, V.P., and Koopman, D.W. (1979) 3rd-Harmonic generation in argon, krypton, and xenon—bandwidth limitations in the vicinity of lyman-alpha. *IEEE Journal of Quantum Electronics*, **15**(6), 444–451.

Marangos, J.P., Shen, N., Ma, H., Hutchinson, M.H.R., and Connerade, J.P. (1990) Broadly tunable vacuum-ultraviolet radiation source employing resonant enhanced sum difference frequency mixing in krypton. *Journal of the Optical Society of America B: Optical Physics*, **7**(7), 1254–1259.

Marian, A., Stowe, M., Lawall, J., Felinto, D., and Ye, J. (2004) United time-frequency spectroscopy for dynamics and global structure. *Science*, **306**(5704), 2063–2068.

Marinero, E.E., Rettner, C.T., Zare, R.N., and Kung, A.H. (1983) Excitation of H_2 using continuously tunable coherent XUV radiation (97.3–102.3 nm). *Chemical Physics Letters*, **95**(6), 486–491.

Melikechi, N., Gangopadhyay, S., and Eyler, E.E. (1994) Phase dynamics in nanosecond pulsed dye-laser amplification. *Journal of the Optical Society of America B: Optical Physics*, **11**(12), 2402–2411.

Merkt, F., Willitsch, S., and Hollenstein, U. (2011) High-resolution photoelectron spectroscopy, in *Handbook of High-resolution Spectroscopy*, Quack, M. and Merkt, F. (eds), John Wiley & Sons, Ltd., Chichester, UK.

Miyazaki, K., Sakai, H., and Sato, T. (1989) 2-Photon resonances in Xe and Kr for the generation of tunable coherent extreme uv-radiation. *Applied Optics*, **28**(4), 699–702.

Nabekawa, Y., Hasegawa, H., Takahashi, E., and Midorikawa, K. (2005) Production of doubly charged helium ions by two-photon absorption of an intense sub-10-fs soft x-ray pulse at 42 eV photon energy. *Physical Review Letters*, **94**(4), 043001.

Neshev, D., Velchev, I., Majewski, W., Hogervorst, W., and Ubachs, W. (1999) SBS pulse compression to 200 ps in a compact single-cell setup. *Applied Physics B*, **68**(4), 671–675.

New, G.H.C. and Ward, J.F. (1967) Optical 3rd-harmonic generation in gases. *Physical Review Letters*, **19**(10), 556–559.

Nolting, J. and Wallenstein, R. (1990) An optical ring resonator designed for frequency tripling of CW dye-laser radiation in metal vapors. *Optics Communications*, **79**(6), 437–442.

Ozawa, A., Rauschenberger, J., Gohle, C., Herrmann, M., Walker, D.R., Pervak, V., Fernandez, A., Graf, R., Apolonski, A., Holzwarth, R. *et al.* (2008) High harmonic frequency combs for high resolution spectroscopy. *Physical Review Letters*, **100**(25), 253901.

Pachucki, K. (2006) Helium energy levels including m α^6 corrections. *Physical Review A*, **74**(6), 062510.

Pachucki, K. (2007) Erratum: Helium energy levels including m α^6 corrections (vol. **74**, art. no. 062510, 2006). *Physical Review A*, **76**(5), 059906.

Papadogiannis, N., Nikolopoulos, L., Charalambidis, D., Tsakiris, G., Tzallas, P., and Witte, K. (2003) Two-photon ionization of He through a superposition of higher harmonics. *Physical Review Letters*, **90**(13), 133902.

Philip, J., Sprengers, J.P., Pielage, T., de Lange, C.A., Ubachs, W., and Reinhold, E. (2004) Highly accurate transition frequencies in the H_2 Lyman and Werner absorption bands. *Canadian Journal of Chemistry*, **82**(6), 713–722.

Pirri, A., Sali, E., Corsi, C., Bellini, M., Cavalieri, S., and Eramo, R. (2008) Extreme-ultraviolet Ramsey-type spectroscopy. *Physical Review A*, **78**(4), 043410.

Ramsey, N.F. (1949) A new molecular beam resonance method. *Physical Review*, **76**(7), 996.

Reinhard, I., Gabrysch, M., von Weikersthal, B.F., Jungmann, K., and Putlitz, G.Z. (1996) Measurement and compensation of frequency chirping in pulsed dye laser amplifiers. *Applied Physics B*, **63**(5), 467–472.

Reinhold, E., Buning, R., Hollenstein, U., Ivanchik, A., Petitjean, P., and Ubachs, W. (2006) Indication of a cosmological variation of the proton-electron mass ratio based on laboratory measurement and reanalysis of H_2 spectra. *Physical Review Letters*, **96**(15), 151101.

Reinhold, E., de Lange, A., Hogervorst, W., and Ubachs, W. (1998) Observation of the $I'^1\Pi_g$ outer well state in H_2 and D_2. *Journal of Chemical Physics*, **109**(22), 9772–9782.

Rocca, J.J., Shlyaptsev, V., Tomasel, F.G., Cortazar, O.D., Hartshorn, D., and Chilla, J.L.A. (1994) Demonstration of a discharge pumped table-top soft-x-ray laser. *Physical Review Letters*, **73**(16), 2192–2195.

Roudjane, M., Ivanov, T.I., Vieitez, M.O., de Lange, C.A., Tchang-Brillet, W.U.L., and Ubachs, W. (2008) Extreme ultraviolet laser calibration of D_2 Lyman and Werner transitions. *Molecular Physics*, **106**(9–10), Sp. Iss. SI), 1193–1197.

Rupper, P. and Merkt, F. (2004) Intense narrow-bandwidth extreme ultraviolet laser system tunable up to 20 eV. *Review of Scientific Instruments*, **75**(3), 613–622.

Salour, M.M. (1978) Quantum interference effects in two-photon spectroscopy. *Reviews of Modern Physics*, **50**(3), 667–681.

Salour, M.M. and Cohen-Tannoudji, C. (1977) Observation of Ramsey's interference fringes in the profile of Doppler-free two-photon resonances. *Physical Review Letters*, **38**(14), 757–760.

Schiemann, S., Ubachs, W., and Hogervorst, W. (1997) Efficient temporal compression of coherent nanosecond pulses in compact SBS generator-amplifier setup. *IEEE Journal of Quantum Electronics*, **33**(3), 358–366.

Schumann, V. (1928) *The Spectroscopy of the Extreme Ultraviolet*, Green and Company, London.

Seiler, R. (2004) *Rydbergzustandsaufgelöste-Schwellenionisationsspektroskopie*, Ph.D. thesis, ETH Zurich, nr. 15591.

Seiler, R., Hollenstein, U., Greetham, G.M., and Merkt, F. (2001) Rydberg-state-resolved zero-kinetic-energy photoelectron spectroscopy. *Chemical Physics Letters*, **346**(3–4), 201–208.

Shen, Y.R. (1984) *The Principles of Nonlinear Optics*, John Wiley & Sons.

Simmons, J.D. and Tilford, S.G. (1974) Evidence for an accidental predissociation of CO. *Journal of Molecular Spectroscopy*, **49**(1), 167–168.

Snadden, M., Bell, A., Riis, E., and Ferguson, A. (1996) Two-photon spectroscopy of laser-cooled Rb using a mode-locked laser. *Optics Communications*, **125**(1–3), 70–76.

Sprengers, J.P., Reinhold, E., Ubachs, W., Baldwin, K.G.H., and Lewis, B.R. (2005a) Optical observation of the 3s σ_gF $^3\Pi_u$ Rydberg state of N_2. *Journal of Chemical Physics*, **123**(14), 144315.

Sprengers, J.P., Ubachs, W., and Baldwin, K.G.H. (2005b) Isotopic variation of experimental lifetimes for the lowest $^1\Pi_u$ states of N_2. *Journal of Chemical Physics*, **122**(14), 144301.

Stahel, D., Leoni, M., and Dressler, K. (1983) Non-adiabatic representations of the $^1\Sigma_u^+$ and $^1\Pi_u$ states of the N_2 molecule. *Journal of Chemical Physics*, **79**(6), 2541–2558.

Stark, G., Huber, K.P., Yoshino, K., Smith, P.L., and Ito, K. (2005) Oscillator strength and linewidth measurements of dipole-allowed transitions in $^{14}N_2$ between 93.5 and 99.5 nm. *Journal of Chemical Physics*, **123**(21), 214303.

Stoehlker, T., Gumberidze, A., Kumar, A., Reuschl, R., and Trassinelli, M. (2008) Quantum electrodynamics in one- and two-electron high-Z ions, in *Current Trends in Atomic Physics*, Sabin, J. and Brandas, E. (eds), *Advances in Quantum Chemistry*, Academic Press, pp. 57–65, Vol. 53.

Sucher, J. (1958) Energy levels of the 2-electron atom to order α^3 Ry—ionization energy of helium. *Physical Review*, **109**(3), 1010–1011.

Tchang-Brillet, W.U.L., Julienne, P.S., Robbe, J.M., Letzelter, C., and Rostas, F. (1992) A model of the B $^1\Sigma^+$–D$'^1\Sigma^+$ rydberg-valence predissociating interaction in the CO molecule. *Journal of Chemical Physics*, **96**(9), 6735–6745.

Teets, R., Eckstein, J., and Hänsch, T.W. (1977) Coherent two-photon excitation by multiple light pulses. *Physical Review Letters*, **38**(14), 760–764.

Timmermann, A. and Wallenstein, R. (1983) Generation of tunable single-frequency continuous-wave coherent vacuum ultraviolet-radiation. *Optics Letters*, **8**(10), 517–519.

Tomboulian, D.H. and Hartman, P.L. (1956) Spectral and angular distribution of ultraviolet radiation from the 300-MeV cornell synchrotron. *Physical Review*, **102**(6), 1423–1447.

Tousey, R. (1962) The extreme ultraviolet—past and future. *Applied Optics*, **1**(6), 679–694.

Trickl, T., Vrakking, M.J.J., Cromwell, E., Lee, Y.T., and Kung, A.H. (1989) Ultrahigh-resolution (1 + 1) photoionization spectroscopy of Kr-I—hyperfine structures, isotope shifts, and lifetimes for the n = 5, 6, 7 4p5ns rydberg levels. *Physical Review A*, **39**(6), 2948–2955.

Ubachs, W. (1997) Predissociative decay of the $c_4'\ ^1\Sigma_u^+$, v = 0 state of N_2. *Chemical Physics Letters*, **268**(1–2), 201–206.

Ubachs, W., Eikema, K.S.E., Hogervorst, W., and Cacciani, P.C. (1997) Narrow-band tunable extreme-ultraviolet laser source for lifetime measurements and precision spectroscopy. *Journal of the Optical Society of America B: Optical Physics*, **14**(10), 2469–2476.

Ubachs, W., Tashiro, L., and Zare, R.N. (1989) Study of the N_2 b $^1\Pi_u$ state via 1+1 multiphoton ionization. *Chemical Physics*, **130**(1–3), 1–13.

Ubachs, W., Velchev, I., and Cacciani, P. (2000a) Predissociation in the $E^1\Pi$, v = 1 state of the six natural isotopomers of CO. *Journal of Chemical Physics*, **113**(2), 547–560.

Ubachs, W., Velchev, I., and de Lange, A. (2000b) Predissociation in b $^1\Pi_u$, v(v = 1, 4, 5, 6) levels of N_2. *Journal of Chemical Physics*, **112**(13), 5711–5716.

Udem, T., Holzwarth, R., and Hänsch, T.W. (2002) Optical frequency metrology. *Nature*, **416**(6877), 233–237.

Velchev, I., Hogervorst, W., and Ubachs, W. (1999) Precision VUV spectroscopy of Ar I at 105 nm. *Journal of Physics B*, **32**(17), L511–L516.

Vieitez, M., Ivanov, T., Ubachs, W., Lewis, B., and de Lange, C. (2008) On the complexity of the absorption spectrum of molecular nitrogen. *Journal of Molecular Liquids*, **141**, 110–117.

Wahlstrom, C.G., Larsson, J., Persson, A., Starczewski, T., Svanberg, S., Salieres, P., Balcou, P., and L'Huillier, A. (1993) High-order harmonic-generation in rare-gases with an intense short-pulse laser. *Physical Review A*, **48**(6), 4709–4720.

Werner, S. (1926) Hydrogen bands in the ultra-violet Lyman region. *Proceedings of the Royal Society of London. Series A, Mathematics and Physical Character*, **113**(763), 107–117.

Wieman, C. and Hänsch, T.W. (1980) Precision-measurement of the 1 s lamb shift and of the 1s-2s isotope shift of hydrogen and deuterium. *Physical Review A*, **22**(1), 192–205.

Wildenauer, J. (1987) Generation of the 9th-harmonic, 11th-harmonic, and 15th-harmonic of iodine laser-radiation. *Journal of Applied Physics*, **62**(1), 41–48.

Witte, S., Zinkstok, R., Ubachs, W., Hogervorst, W., and Eikema, K. (2005) Deep-ultraviolet quantum interference metrology with ultrashort laser pulses. *Science*, **307**(5708), 400–403.

Witte, S.M. (2008) *Terawatt-Intensity few-Cycle Laser Pulses—Optical Parametric Chirped Pulse Amplification and Frequency Comb Spectroscopy*, Ph.D. thesis, Vrije Universiteit, Amsterdam.

Wolk, G.L. and Rich, J.W. (1983) Observation of a new electronic state of carbon-monoxide using LIF on highly vibrationally excited CO($X\ ^1\Sigma^+$). *Journal of Chemical Physics*, **79**(1), 12–18.

Wörner, H.J. and Merkt, F. (2011) Fundamentals of electronic spectroscopy, in *Handbook of High-resolution Spectroscopy*, Quack, M. and Merkt, F. (eds), John Wiley & Sons, Ltd., Chichester, UK.

Yoshino, K., Smith, P.L., Parkinson, W.H., Thorne, A.P., and Ito, K. (1995) The combination of a VUV fourier-transform spectrometer and synchrotron-radiation. *Review of Scientific Instruments*, **66**(2), 2122–2124.

Zerne, R., Altucci, C., Bellini, M., Gaarde, M.B., Hänsch, T.W., L'Huillier, A., Lyngå, C., and Wahlström, C.-G. (1997) Phase-locked high-order harmonic sources. *Physical Review Letters*, **79**(6), 1006–1009.

Zinkstok, R.T. (2008) *Precise Control of Electromagnetic Fields and Atomic Excitation*, Ph.D. thesis, Vrije Universiteit, Amsterdam.

Zinkstok, R.T., Witte, S., Ubachs, W., Hogervorst, W., and Eikema, K.S.E. (2006) Frequency comb laser spectroscopy in the vacuum-ultraviolet region. *Physical Review A*, **73**(6), 061801.

RELATED ARTICLES

Albert *et al*. 2011: **High-resolution Fourier Transform Infrared Spectroscopy**
Gallmann and Keller 2011: **Femtosecond and Attosecond Light Sources and Techniques for Spectroscopy**
Jungen 2011: **Elements of Quantum Defect Theory**
Merkt *et al*. 2011: **High-resolution Photoelectron Spectroscopy**
Wörner and Merkt 2011: **Fundamentals of Electronic Spectroscopy**